Systematic evaluation of a microwave medical imaging system

Matilde Pereira Moreira

Thesis to obtain the Master of Science Degree in

Electrical and Computer Engineering

Supervisors: Prof. Carlos António Cardoso Fernandes
Prof. João Manuel de Almeida Monteiro Felício

Examination Committee

Chairperson: Prof. José Eduardo Charters Ribeiro da Cunha Sanguino
Supervisor: Prof. Carlos António Cardoso Fernandes
Member of the Committee: Prof. Octavian Adrian Postolache

September 2021

Declaration

I declare that this document is an original work of my own authorship and that it fulfills all the requirements of the Code of Conduct and Good Practices of the Universidade de Lisboa.

Acknowledgments

On September 9, 2015 was the beginning of one of the most important chapters of my life, my admission to the University - Instituto Superior Técnico, in Electrical and Computer Engineering. 6 years have passed since that day and I still vividly remember my first day.

In the same month that I started my research for the thesis, in March 2020, the coronavirus pandemic has reached every country in the world. In order to prevent the spread of the virus, most establishments, including educational establishments, were forced to close.

Given the situation we live in, most of my thesis work was developed from home, which made the whole process difficult and delayed. During my penultimate year of college, I always imagined that my thesis was mostly developed at Instituto Superior Técnico. However, those ideas totally disappeared due to COVID-19, so most of my meetings were remotely.

Throughout this dissertation I have received a great deal of support and assistance by my supervisors.

First of all, I would like to express my gratitude to my supervisors, Professor Carlos Fernandes and João Felício, for having guided, motivated, shared of knowledge and supported me, with quality, during the development of both my thesis and the introduction to the thesis, even more so given the pandemic situation that we are living and all the adversities that resulted from this disease. During the thesis, numerous challenges have emerged and you were always here to help me, always encouraging to understand all of the concepts. Your insightful feedback pushed me to sharpen my thinking and brought my work to a higher level.

I would like to thank to Instituto de Telecomunicações, that always tried to provided the tools and conditions to develop this thesis.

Secondly, I am deeply grateful to my mother Ana Maria, and my maternal grandmother Albina for always being by my side through thick and thin, for all the sacrifices they made so that I could study and never give up on my own dreams and for all the care, love and strength they have always given me. I would also like to thank my family for their understanding and support throughout all these years.

To my caring, loving, and supportive boyfriend, João Pedro: my deepest gratitude. Your encouragement when the times got rough are much appreciated. My heartfelt thanks.

My completion of this thesis could not have been accomplished without the support of my friends and colleagues, that helped me grow as a person and were always there for me.

Finally, I would like to thank Mr. Carlos Brito for all his help manufacturing and welding the prototype and Raquel Martins for all the support and her help with prototype measurements.

Abstract

The breast cancer has the highest cancer attack-rate among women. The standard methods of breast cancer detection are painful, time consuming, expensive and harmful. The drawbacks of these methods have resulted in research into alternative methods of breast imaging. Microwave Breast Imaging (MWI) has received attention for many years. The Antennas and Propagation group at Instituto de Telecomunicações has been working in medical imaging techniques based on microwave radar and they developed a contactless microwave imaging system, that is a dry setup, for breast cancer screening. A Graphical User Interface is used to control the system along with adequate signal processing. In this dissertation, it is also possible to know the changes in the interface and the setup. In order to deal with the challenges of the dry setup exists an algorithm based on singular value decomposition (SVD), that removes the skin back-scattering. There exist two calibration methods to remove the early time reflections: the Ideal Calibration and the SVD. Before submitting the setup to clinical trials, it is important to test the set-up in controlled environment using phantoms. This dissertation demonstrates the results of the test using a set of breast phantoms anthropomorphic. The numerical results include the study of the behavior of the XETS antenna depending on distance to the target, in order to understand how the distance of the XETS antenna affects the results during the experimental measurements with breast phantoms. The results were promising, as it was possible to detect the tumors for most breast phantoms.

Keywords

Breast cancer; microwave imaging (MWI); artifact removal; phantom; measurement setup

Resumo

O cancro de mama é o cancro invasivo mais frequentemente diagnosticado entre as mulheres. Os métodos convencionais de deteção do cancro de mama são dolorosos, demorados, dispendiosos e prejudiciais. As desvantagens destes métodos resultaram na pesquisa de métodos alternativos de imagem da mama. A imagem por microondas tem recebido atenção desde há muitos anos e existem inclusive protótipos desenvolvidos. O grupo de Antenas e Propagação do Instituto de Telecomunicações tem trabalhado em técnicas de imagem por microondas baseadas em radar e desenvolveram um sistema de imagem por microondas sem contacto, um sistema seco, para rastreio do cancro da mama. Uma Interface Gráfica de Usuário é utilizada para controlar o sistema e efetuar o processamento dos sinais. Nesta dissertação é possível conhecer as mudanças feitas na interface e no sistema. Para lidar com os desafios da configuração seca existe um algoritmo baseado na decomposição de valor singular (SVD), que remove a contribuição da pele. Existem dois métodos de calibração para remover as reflexões: a calibração ideal e o SVD. Antes de submeter a configuração a ensaios clínicos, é importante testar a configuração num ambiente controlado usando phantoms. Esta dissertação demonstra os resultados do teste utilizando um conjunto de phantoms antropomórficos de mama. Os resultados numéricos incluem o estudo do comportamento da antena XETS em função da distância ao alvo, a fim de entender como a distância da antena XETS afeta os resultados durante as medições experimentais com phantoms. Os resultados foram bons, pois foi possível detetar os tumores para a maioria dos phantoms de mama.

Palavras Chave

Cancro da mama; imagens por microondas (MWI); remoção de artefato; phantom; demonstrador de medida

Contents

List of Figures

List of Tables

List of Acronyms

BAVA Balanced antipodal Vivaldi antenna. 9, 32, 34, 36, 37, 41, 79

CABAVA Circular Array Balanced Antipodal Vivaldi Antenna. 47, 50, 66, 68, 70, 79, 80
CMOS Complementary Metal-Oxide-Semiconductor. 11
CST Computer Simulation Technology. 25, 26

DC Dartmouth College. 7
DC Direct Current. 58
DNA Deoxyribonucleic Acid. 18

ETRI Electronics and Telecommunications Research Institute. 10

FFT Fast Fourier Transform. 8

GMP Gaussian monocycle Pulse. 11
GUI Graphical User Interface. 3, 66, 67, 69, 72, 74, 75, 80

HP Huygens Principle. 11
HU Hiroshima University. 11

IFBW Intermediate Frequency Band Width. 68
IT Instituto de Telecomunicacões. 3, 12, 31, 66, 79, 80

MARIA Multistatic Array Processing for Radiowave Image Acquisition. 8
MRI Magnetic Resonance Imaging. 2, 4, 5
MS-MIST Multistatic Microwave Imaging via Space Time. 9
MU McGill University. 10
MWI Microwave Breast Imaging. 3–6, 8, 9, 31, 70

PE Positioning Error. 23
PLA Polyactic acid. 32, 38, 42, 46, 47, 53, 57, 61, 70

RF Radio Frequency. 70
RMS Root Mean Square. 68

SPDT Single Pole Double Throw. 69
SU Shizuoka University. 9, 10
SUST Southern University of Science and Technology. 11
SVD Singular Value Decomposition. 21, 22, 25, 35–37, 39, 42, 43, 46, 48–50, 52, 53, 55, 58, 62, 64, 65, 74, 79

TCR Tumor-to-clutter Ratio. 23, 41, 57

TMR Tumor-to-mean Ratio. 23, 41, 57
TSAR Tissue Sensing Adaptive Radar. 9

UM Manitoba University. 12
UM-MWID University of Manitoba Microwave Breast Imaging Dataset. 14
UWB Ultra wide-Band. 5, 9, 11

VNA Vector Network Analyzer. 3, 8, 9, 11, 12, 14, 15, 25, 42, 47, 53, 61, 66, 68, 69, 71, 72, 75, 76, 79

WS Workstation. 9, 10

XETS Crossed Exponentially Tapered Slot. 15, 25–27, 29, 32, 37–39, 41–43, 47, 50, 53, 57, 58, 61, 62, 79

List of Symbols

v	Speed of light in vacuum.
k	Wave Number.
n	Refractive Index.
d	Distance.
λ	Wavelength.
E	Electric Field.
f	Frequency.
ε	Dielectric constant.
σ	Conductivity.
x, y, z	Cartesian Components.

1

Introduction

Contents

This chapter approaches the advantages and disadvantages of conventional methods and introduces breast microwave breast imaging as a potential method for breast cancer detection. Some of Microwave breast imaging systems have been employed and they are presented in this section, as well as the challenges faced during clinical trials. The chapter concludes with the problem statement of this thesis.

1.1 Motivation and Objectives

Global statistics indicate that breast cancer is the most frequently diagnosed invasive cancer and the second cause of death by cancer among female patients [11, 12]. Until July 2021, the estimation of the number of new cases and deaths, all over the world, was approximately 281 550 and 43 600,respectively. [11]. Survival following a diagnosis of breast cancer is grossly determined by the stage of the disease at the time of initial diagnosis, highlighting the importance of early detection, so if the tumor is detected in its initial stage, the relative survival rate in 5 years after diagnosis is more than 90% [11].

The number of breast cancer cases in developed countries continues to rise, however, the mortality rate has decreased substantially. This is due to the fact that over the years, there have been numerous studies on how to prevent, detect and treat cancer, always taking into account the improvement of people's quality of life, with cancer, during and after treatment [12]. Technology has had a strong impact on the early detection of cancer, through improved treatment methods, the implementation of screening programs and improved imaging techniques [12, 13]. The methods and techniques must be specific and sensitive, in order to detect the presence of a tumor in an early-stage and also to distinguish between malignant and benign lesions [14].

In this era of a rising incidence of breast cancer, the diagnosis at the earliest stage requires further improvements in the efficiency and capabilities of current diagnostic modalities and the expansion of novel imaging systems. Nowadays, the current conventional imaging applications used in breast cancer detection are X-Ray mammography, Magnetic Resonance Imaging (MRI) and ultrasound [13]. All these modalities exploit a variety of properties of biological tissues to form an image, whose aspects are summarized in the table 1.1.

Table 1.1: Comparisons between different imaging techniques for breast cancer detection. [10]

Imaging Techniques	Patients Comfort	Radiation Safety	Cost	Time Required	Effectiveness
X-ray mammography	Uncomfortable	Ionizing Radiation	Low	Less than 10min	Can detect up to few mm. Tumors without a distinct mass or calcification are difficult to identify. The sensitivity in dense breast is low.
Ultrasound	Comfortable	Non-ionizing Radiation	Low	15min-25min	Can detect tumors up to few cm. Effective for dense breast.
MRI	Uncomfortable	Non-ionizing Radiation	High	45min-1hr	Effective in detecting tumors up to few mm. Effective for dense breast.

In order to overcome the shortfalls of the aforementioned screening methods, which are presented in the table 1.1, Microwave Breast Imaging (MWI), a low cost and non-ionizing imaging modality that represents a promising imaging modality of breast cancer detection, is being investigated. MWI exploits the contrast of dielectric properties of biological tissues to form images, potentially providing complementary information to conventional diagnoses [2, 12, 13, 15, 16]. For all these reasons, MWI is an attractive method for breast cancer detection overcoming limitations of traditional detection methods. Considering all the shortfalls of the conventional methods and the vantages of MWI, the dissertation will address a set-up using a radar-based MWI.

In recent years, the Antennas and Propagation group of Instituto de Telecomunicacões (IT), at Instituto Superior Técnico, in Lisbon, has been working and acquired experience in medical imaging techniques based on microwave radar (MWI). This experience has been acquired through the development of a contactless microwave imaging system for breast cancer screening to be submitted to clinical trials. The setup comprises a ring of 8 antennas distributed in a circular ring that can move up and down in order to take the measurements. The system also comprises an optical camera which takes snapshots of the breast, to reconstruct the breast image, and a Vector Network Analyzer (VNA). The group has already developed an application with user friendly interface to control the system along with adequate signal processing algorithms to cope with the inherent challenges that MWI faces.

Prior to clinical trials, it is important to test the set-ups in controlled environment through the use of phantoms, instead of people. The phantoms are an artificial structure that mimics the properties of the human body, such as the electric properties, light scattering and optics and sound wave reception. [17] Therefore, there is a need to validate these phantoms and the reliability of the exams, and for this, it is necessary to compare results between different international groups working in the same area of research. Within this framework the goals of this master's dissertation are:

- Use the Instituto de Telecomunicacões (IT) Microwave Breast Imaging (MWI) set-up to examine a set of phantoms anthropomorphic, where most of them were developed at a Manitoba university that collaborates with IT;

- Develop the MWI image acquisition set-up of IT, to prepare it for the clinical tests stage in hospitals;

- Further develop the Graphical User Interface (GUI), which interacts directly with the user and operates the setup. A part of the interface was developed in previous works [18, 19].

- Improve the IT set-up and methods of reconstructing the medical image of the breast from radar echoes.

- Implement calculation acceleration strategies to allow obtaining images of the breast in real time.

1.2   State of the Art

The ability of microwaves to penetrate and image biological tissues was demonstrated by Larsen and Jacobi, in the 1970s, through the imaging of canine kidneys. [20]. From the promising results obtained, microwaves quickly became the focus of imaging applications, particularly with microwave/acoustic and radiometry systems, but also with active microwave imaging systems. [1]

Over the past two decades of research on breast tumor detection, several MWI setups have been developed and demonstrated. Some of which have already been used in clinical trials or/and developed commercially. [1] Three commercial ventures for breast tumor detection were made by the Microwave Imaging System Technologies - MIST (Dartmouth College, USA), MARIA (Bristol University,UK) and Microwave Vision SA, France. [1] In the subsection 1.2.3, some systems are presented, as well as the challenges faced during clinical trials. Some factors were found to have an impact on measured dielectric properties in the tissues, such as the patient age, time between measurement and excision. [21]

1.2.1   Conventional Imaging Techniques

The standard technique for breast cancer screening and detection is X-ray mammography [22], that is an imaging modality based on the attenuation coefficient contrast between cancerous and healthy tissues [13, 23, 24]. Although mammography is not time consuming, it exposes the patient to ionizing radiation, which can cause serious health problems. It is very painful to the patient, since the breast needs to be compressed, in order to obtain a better image quality. The rate of failure of mammography in detecting breast cancer is relatively high and ranges from 4% to as high as 34%, essentially in patients with high radiographically density breast tissues [15]. Even in women with lower breast density, the sensitivity for screening mammography is 88.4% [12].

MRI is non-invasive technique, that uses strong magnetic fields to produce high resolution and quality of images of the breast, affords a sensitivity of over 90%, [12], this is why is primarily used as a supplemental tool to mammography. Usually, a breast MRI is used for women who have been diagnosed with breast cancer, to help measure its size, check for tumors in the opposite breast and also to look for other tumors in breast.

The specificity of lesion characterization remains low to moderate (72%) making the distinction between malignant and benign lesions difficult. [25] For some patients, it is necessary to inject an intravenous liquids, in order to improve contrast in the images. [26] MRI does not show micro-calcifications, which can be a sign of breast cancer [25], it is expensive, time-consuming (20-90min), claustrophobic and is also contraindicated in patients having pacemakers and other type of implants. [1]

Ultrasound imaging of the breast is a scan that uses penetrating sound waves, that do not affect or damage the tissue, to produce pictures of the internal structures of the breast, in real-time. [27].

Ultrasound is the modality of choice for further investigation of palpable breast findings that are not clearly benign and screen-detected abnormalities [28] and is recommend to prevent unnecessary radiation exposure to women under 30 years of age, generally have a higher breast tissue density and lower sensitivity. [12, 27, 28]. Ultrasound is a non-ionizing, painless, low cost, highly sensitive (81.7%), specific (88%) instrument for investigating symptomatic patients [12]. However, shows small resolution, is time consuming [29] and the examiner influences effectiveness of the results and the "sonogram" obtained.

1.2.2 Microwave Breast Imaging

The drawbacks of the aforementioned screening methods have resulted in research into alternative methods of breast imaging. Microwave imaging of biological structures has received extensive attention for many years. Recently, microwave imaging for breast cancer detection is being considered as a diagnostic tool that can complement well-established methods, previously covered. [16] The main motivation was the hypothesis that the electrical properties, conductivity and permittivity, of malignant breast tumors tissue differ significantly from those of the normal surrounding breast tissue.

Furthermore, microwave frequencies are non ionizing, that is risk-free for the patient, and they also exhibit reasonable penetration in breast tissue, despite the fact that it has low or poor resolution. [12, 22] The patient is more comfortable, since MWI does not require any painful compression of the breast. MWI is recommended also for younger women with dense breast and also avoids the injection of contrast agents, that is contraindicated for pregnant women, kidney patients,etc. The most crucial advantage of MWI over the MRI, is its low cost. For all the reasons presented, MWI is an ideal candidate for large scale screening campaigns and post-treatment cancer surveillance. [6]

There are four active imaging methods proposed for MWI,Ultra wide-Band Radar, Tomography, Holographic and Hybrid Imaging. The hybrid imaging technique is used to compensate the shortcomings of conventional imaging techniques, where efforts were taken to incorporate MWI techniques into them and the holographic imaging is based on the hologram technique in optics to generate a 3D view.

The tomographic approaches aim to reconstruct the dielectric breast profile based on dielectric properties, using non-linear inversion algorithms. [3, 6]. Due to the ill-posedness and the non-linearity of the problem, the inversion algorithms are very time-consuming, since non-linear inversions may take days of the CPU [6]. Figure 1.1 shows various stages in tomography. The regularization technique helps to change the original ill-posed problem by a well-posed one. [1]

Alternatively, the radar approach belongs to the class of linear scattering techniques, which is much faster computational signal processing. UWB radar microwave imaging overcomes the computation challenges of microwave tomography.

In MWI, the sensors are the transmitter and receiver antennas. While transmitter antennas illuminate the breast with microwave signals, receiver antennas collect the signals scattered back from the breast.
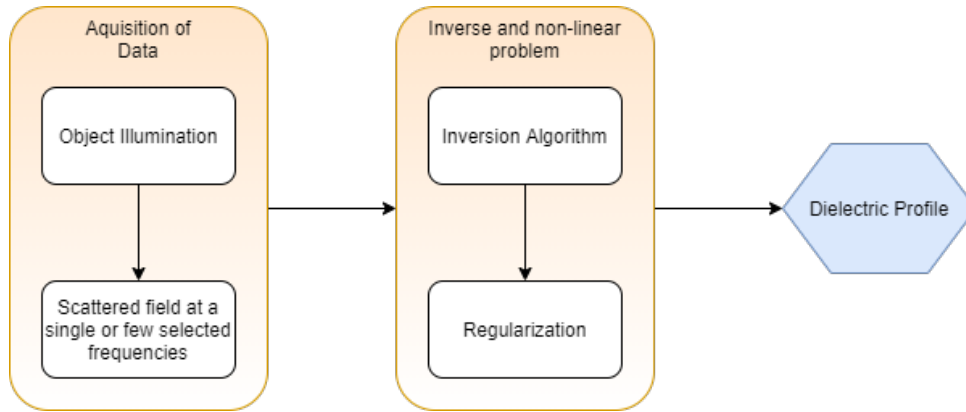
Figure 1.1: Stages in tomography. [1]

Due to the dielectric contrast, a tumor will cause a highly energetic spot in the image, since malignant tissues have higher density and water content than the breast's adipose tissue, which has low dielectric constant (permittivity), because its low water content [6, 15]. The glandular tissue has also a high water content, and the permittivity is just 10-30% lower than the cancerous tissue constant. If the tumor appears in the middle of a glandular tissue, it could be masked by a clutter, making the detection of the tumor difficult.

Figure 1.2 illustrates a patient laid prone on the stretcher and the breast extended through a circular gap, during an examination. The antennas are positioned around the breast's patient radiating with microwave signals and recording the backscatters from within breast. In MWI, the work frequencies vary between 1 to 10 GHz, which correspond to a wavelength interval from 300 to 30 mm, respectively.
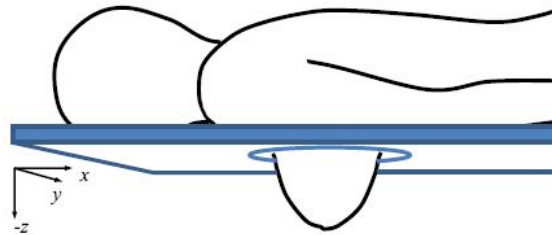
Figure 1.2: Breast screening scenario through Microwave Imaging. [2]

1.2.3 Microwave Breast Imaging Systems

Several operational microwave systems have been employed to trials to investigate the clinical feasibility of MWI. [12] The table 1.2 shows the differences between the operational microwave systems in terms of technical design parameters, patient interface and reconstructions algorithms. [13]

Regarding the technical design, most operation systems collect multi static data, where it is used

6

Table 1.2: Summary of microwave breast imaging systems developed. [1]

Systems	Largest trial	Position	Imaging	Freq [GHz]	Antenna	Scan Time	Acquisition
MARIA,UK	223	prone	Radar	3-8	slot	10s	frequency
DC,USA	150	prone	Tomo	0.7-1.7	monopole	5min	frequency
MU (Table)	13	prone	Radar	2-4	TWTLTLA	18min	time
MU (wearable)	38	seated	Radar	2–4	microstrip	5min	time
SUST, China	11	prone	Radar	4–8	horn	4min	frequency
TSAR, Canada	8	prone	Radar	1.3–7.6	vivaldi	30min	frequency
HU, Japan	5	supine	Radar	3.1–10.6	planar slot	3min	time
SU, Japan	2	prone	Radar,Tomo	4–9	stacked patch	3min	frequency
Microwave Vision	pilot	prone	Radar	1–4	vivaldi	10min	frequency
Mammowave, Italy	51	prone	HP	1–9	PulsON P200	10min	frequency
Kobe University, Japan	20	supine	Tomo	0.05–12	UWB	30min	time
ETRI, Korea	15	prone	Tomo	3–6	monopole	15 s/slice	frequency
Manitoba, Canada	-	prone	Radar,Holo	1–8	horn	-	frequency

different antennas to record and transmit, but monostatic acquisition has been also investigated, where the same antenna transmits and records the reflected signals. [13] Most operational systems require the patient to lie prone on an examination table, but there are also systems that require the breast to be immersed in a coupling medium or to be in direct contact with a solid coupling shell. [13]

The challenges that imaging operating systems and clinical evaluations face are related to the influence of the technical design parameters on clinical use, the effect of the acquisition hardware and algorithm design on the patient scan time and the system mechanical complexity and the implications for design safety. [1]

The first clinical prototype for tomographic imaging of the breast was developed by Meaney et al. from Dartmouth College (DC) in the United States developed in 2000. This research group have studied microwave tomography breast imaging since 1990s. [3] In this setup, the patient is laying in prone position and the breast is immersed in a saline coupling medium with a liquid, which can mask the internal structure of the breast, due to its high relative permittivity and reflections from the skin. [30]

Figure 1.3 shows the tomographic microwave breast imaging system at DC.

Figure 1.3: The microwave breast imaging system at Dartmouth College. [3]

The clinical prototype is constituted by 16 monopole antennas that operate in the 300 MHz to 1GHz

frequency range and radiate to the breast positioned in the center of the circular antenna configuration. [1] All the antennas can transmit and receive in order to maximize the number of measurements. [3] The monopole antennas used in this prototype are not the most adequate for microwave breast imaging, because its isotropic radiation pattern does not satisfy the requisites of MWI, but despite that they work well in lossy environments. [22].

Radar-based MARIA can be done in the frequency or time domain. Many of the systems built using a frequency approach have now matured towards clinical trials. Recently, the radar imaging by time domain started coming up and they offer notably reduce scan time. [1] The research group from Bristol University, UK, performed pioneering work in frequency-domain acquisition, where a frequency-domain signal acquisition procedure involves the collection of S-parameter measurements using VNA. The signals which are reflected from the breast surface are collected by sweeping frequencies and they are converted to the time-domain signals using an inverse Fast Fourier Transform (FFT) method. The time domain signals allow to reconstruct the image through focusing algorithms.

The first prototype named Multistatic Array Processing for Radiowave Image Acquisition (MARIA) was composed of 16 cavity-backed slot antenna multistatic radar system positioned in 4 by 4 hemispherical matrix and the work frequency bandwidth varies from 3 to 8 GHz. [1] This antenna type is a rectangular cube with metallic walls and a cavity inside and have smaller dimensions, thus allowing to maximize the number of antennas. Each antenna is connected through coaxial cables to a switch system, to commute between the pairs of antennas during signal acquisition. Figure 1.4 represents the first MARIA prototype developed.
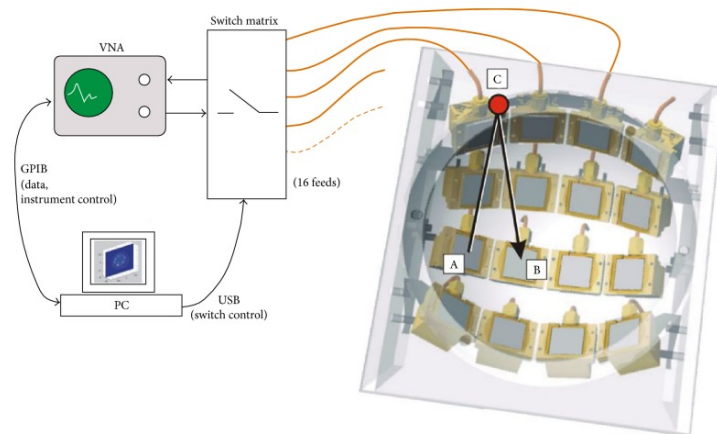
Figure 1.4: MARIA®system developed at the University of Bristol, UK. [1]

The patient has to be in prone position and this prototype is integrated into a compact unit that can slide beneath the examination table to make cleaning between each patient easier. The breast is placed in a coupling shell or a bio-compatible material.

MARIA®4 is being developed and commercialized by MICRIMA and this system has undergone

clinical trials at the several breast cancer imaging centers in the UK. hereafter, the research group improved the system to 60-element antenna array with 8-port VNA, MARIA®5. The scan time was reduced to 10 seconds. However, artifacts can occur due to patient movement.

Calgary University researchers created a prototype based on monostatic radar system, the Tissue Sensing Adaptive Radar (TSAR), which uses Balanced antipodal Vivaldi antenna (BAVA) with four degrees of freedom of movement [1] to examine the patient's breast and where the work frequency bandwidth varies from 1.3 to 7.7GHz. BAVA antennas are coplanar and broadband and they are good candidates for medical MWI due to their compact size and fairly directive radiation patterns. Despite BAVA antennas having a significant large size, it requires multiple antennas.

TSAR uses a synthetic array, where the transmitting or receiving antennas move during the patient scan to create the full synthetic array. [13]. This kind of arrays simplify the system mechanically, since they have less antennas, facilitating the calibration. The concern of synthetic array is the breast safety, since the only antenna exams the breast by rotating around with the help of a mechanical arm, and the antenna cannot have calibration errors in order to avoid collisions with the breast. The other reason that the acquired data has to be calibrated is to remove skin reflections.

Figure 1.5 represents the TSAR setup. [1, 4]
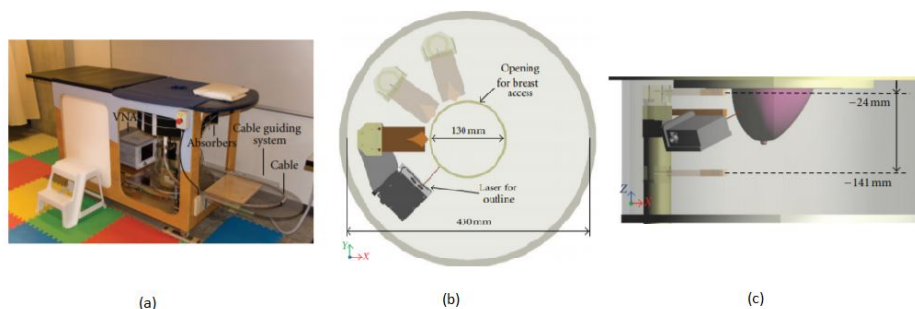
Figure 1.5: TSAR prototype system (a) setup used to scan volunteers (b) Top view (c) Side view. [4]

The patient lies prone on an examination table as in MARIA®'s prototype. The breast extends through a hole to a coupling medium tank filled with canola oil to improve the matching between the sensor and the breast, but lacks of hygiene and causes discomfort for the patient. TSAR uses the frequency domain like MARIA®'s prototype. [1] The process of moving the sensors and collecting measurements takes 30 minutes for 1 breast scanned at up to 200 antenna locations.

A conformal system has also been developed at Shizuoka University (SU), Japan, and it is based on multistatic UWB radar, which features are Multistatic Microwave Imaging via Space Time (MS-MIST) algorithm for high resolution with low artifacts and a conformal array that fixes the breast to the inner shape of a sensor via suction. [5] This prototype requires neither measurement of the breast shape, nor placement of the breast in a tank filled with a coupling liquid. [31]. The equipment used in this prototype is composed of a sensor, an aspirator, an antenna switch, a VNA, a PC for control and a Workstation

(WS) for data processing, as shown in the figure 1.6. [31]
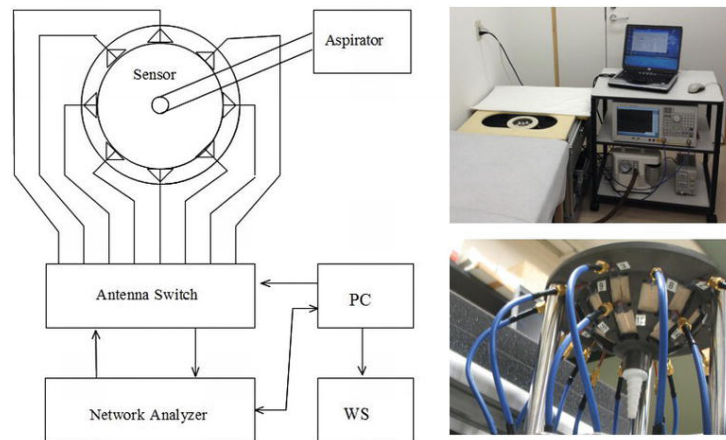
Figure 1.6: Microwave mammography system. [5]

There are different sensor types for various breast sizes, with different number of antennas. [31] The antenna is a stacked patch and has been designed to correspond to a bandwidth of 4 to 9 GHz, when it touches the breast. The sensor with suction restrains the patient from moving and breathing during the scan, since the pressure in the sensor decreases by the aspirator. [5] The antennas are embedded in a cup, whose material has almost the same electromagnetic parameters as the adipose tissue ($\epsilon_r = 6.3$, $\sigma = 0.15$, at 6 GHz). [13].

The patient has to be in prone position and places the breast in the sensor. The inspection time depends on the number of antennas and to remove artifacts is used an array rotation technique. [5] With this technique, it is difficult to detect the tumor whose boundary is irregular and which is buried in the fibroglandular tissue. [32]

McGill University (MU) developed a wearable prototype in time-domain employing a stationary 16-element antenna array for imaging in the wearable system, specifically flexible microstrip antennas,that have a PCB with flexible substrate to route the signal, which work frequency bandwidth varies from 2 to 4GHz. [13] This systems is characterized for not having moving parts and since requires more antennas, it makes the calibration more difficult. The system integrates all the acquisition and excitation hardware, and even the antennas in a bra, which is worn by the patient.The bra is undersized in order to ensure good contact between the breast and the antennas. The procedure is done with the patient seated down. Since the bra is slightly undersized, it doesn't totally cover the breast which may lead to errors during the monitoring of the signals. Monitoring consists on comparing signals over time, as it seen in SU, in order to detect differences between the signals.

Another imaging unit presently engaged in clinical trials for tomographic imaging of the breast was made in 2010 by researchers from the Electronics and Telecommunications Research Institute (ETRI) of Korea, using monopole antennas, which work frequency is in the range of 3 to 6 GHz spectrum. [1]

In the same year, a 3D imaging system designed to work at 3GHz was developed by Zhurbenko et al. with the antennas arranged in the form of a cup into which the patient's breast was to be placed. The time acquisition of this setup was 50 seconds. Since the cup was of a fixed size, the imaging of the patients' breasts, whose size varies created a problem, since larger breast sizes needed compression, while smaller breasts introduced gaps and increased losses. [33]

Hiroshima University (HU), Japan, developed a hand-held impulse-radar system against the widely used table-top design, using a Complementary Metal-Oxide-Semiconductor (CMOS) integrated circuits covering the UWB width from 3.1 to 10.6 GHz, which enable the generation and transmission of Gaussian monocycle Pulse (GMP) [34] as an alternative to high-speed pulse generator and oscilloscope. [3] The detector is designed to be placed on the breast with the patient in the supine position.

Microwave Vision group developed the Wavelia imaging system with a work frequency comprehended in 0.5 and 4.1GHz, which has a set of 18 wideband Vivaldi antennas with an horizontal and circular configuration. Wavelia was implemented in the Galway University Hospital in Ireland. The system has an examination table on which the patient can lie in prone position. A hole in the table allows the patient to immerse the breast under examination in a tube containing a coupling medium liquid, that was created with specific dielectric properties. [35] Wavelia uses frequency-domain to adquire data. The device take approximately 10 minutes to complete a scan. [1] Efforts were made to mitigate some measurement errors and uncertainty, due to the contributions of the system noise floor and system croostalk, the mechanical movements and temperature drift. [35]

A radar-based system has also been presented from the Southern University of Science and Technology (SUST), China. The system consist of a multi-static virtual array with two small UWB horn antennas controlled by mechanical rotation. The horn antennas are immersed in a plastic tank filled with corn oil. A VNA is used as the signal source, which spans a frequency spectrum from 4 to 8.5 GHz. [36] The patient needs to lie in the prone position on the examination table, like other systems previously covered. [13] The antenna array rotates and S parameters are recorded. As the calibration procedure, SUST adopted the artifact estimation method that is obtained by the combination of signals from neighboring channels. [36]

The Mammowave device is based on the Huygens Principle (HP) to process the microwave signals and to build the respective microwave images. [1] It is constituted by one transmitting antenna (TX), one receiving antenna (RX) and a hub with a cup, made in Teflon, that are placed to contain the breast of the patient, in prone position, and two arms to rotably associate TX and RX to the hub. Both antennas operate in the frequency range of 1 to 9 GHz and are connected to a VNA. [37] Antennas and the breast are in free space, unlike most systems, since no matching liquid is used. The whole process of data acquisition is computer controlled and the scan time is 10 minutes. [1] All recorded data is transferred to a secure server following the exam completion, for image processing. [37]

Manitoba University (UM), Canada has also presented a radar-based system. The Manitoba setup is a pre-clinical breast microwave imaging system and it uses a VNA to supply a stepped-frequency continuous-wave signal over 1-8 GHz to a double-ridged horn antenna. Furthermore, the setup operates in air, without the use of a coupling medium. So far, in addition to the setup described in this work, Instituto de Telecomunicacões (IT), the Manitoba Setup is one of the two setups that have been published in the literature that do not use gel and coupling between antennas and. breast tissue. [38] The system can operate in monostatic or bi-static scan configurations and the antennas are rotated along a circular trajectory during the scan. For each one of the positions, the VNA measures the S-parameters and since this system only has two antennas, the VNA only measures S11 and S21 scattering parameters, if it is considering the bi-static scan configuration. [38, 39] The duration of a scan with Manitoba University system is determined not only by the dimensions of the imaged target, but also by the number of antenna locations programmed.The synthetic aperture radar algorithm is used to reconstruct images of the scans and was previously mentioned in [39]. A photograph of the Manitoba University system is displayed in Figure 1.7.

(a) Side view of the system with a bi-static antenna configuration and a breast phantom

(b) Rotating radar module of the system.
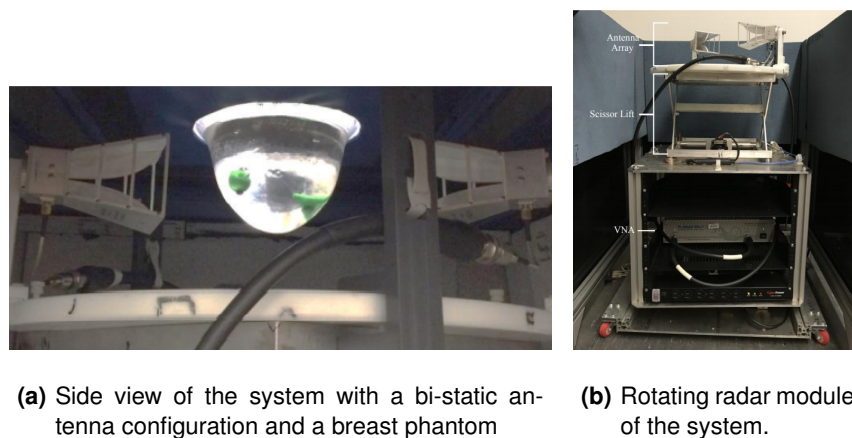
Figure 1.7: Radar-based Manitoba setup. 1.7(a)

1.2.4 Phantoms

For the simulation studies, phantoms are created based on highly accurate imaging modalities in order to have closer-to-reality results and emulating the human-body part, that is breast. However, multiple approximations are generally used in simulations, in order to simplify electromagnetic analyses, that lower the accuracy of the results. An example of such approximations is using boundary conditions to eliminate multi-path signals at discontinuities. [40]

The phantoms are normally hollow and carry a prepared solution according to a recipe, in order to

emulate the electromagnetic response of the human tissues, this is the electric properties and to be used to tune the performance of medical imaging devices. However, phantoms are also solid models with the advantage of not using those prepared solutions, which can degrade with time. In summary, there are three types of primary phantoms used in the literature: solid, liquid and gel phantoms.

Gel phantoms must be individually prepared by hand and are therefore unique, although the material can closely model the dielectric properties of breast tissues. [41, 42]

Solid phantoms use solid materials as the tissue mimicking materials and they are robust, stable and can be 3D-printed, allowing its replication. One of the biggest limitations of this type of phantom is due to its unique geometric shape and the fact that it cannot be modified because the components are solid. [9]

Liquid phantoms use liquids to emulate the human-body part and use shells to contain these liquids. Initially, the phantoms used hemispherical or cylindrical shells [43] made of low-permittivity plastics. [44, 45]

The phantom can be classified in three different groups, according to adipose tissue content. The first one has a content between 0% and 30%, the second varies from 31% to 84% and finally, the third group has a content, which interval goes from 85% to 100%. [22, 46] As the adipose tissue content increases, the dielectric constant (permittivity) decreases, which should ease the tumor detection.

Figure 1.8 shows two experiments with different coupling liquids that have different properties. The first version, a group of researchers have experimented with 2D tumor phantoms represented by two different cylinders immersed in a tank filled with a mixing of glycerin (80%) and water (20%), while the second version of their prototype, they experimented with the GePs-L2S breast phantom that represents a 3D realistic breast consisting of three different tissues: adipose, fibroglandular and tumor.

Each of these parts is filled with Triton x-100, a nonionic surfactant often used as a detergent in laboratories. This liquid mimics the dielectric characteristics of the 85-100% adipose tissue content of the normal breast tissue in a frequency range (0.5-3GHz). [6]
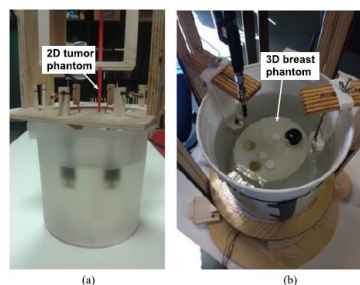
Figure 1.8: (a) Tank filled with glycerin-water mixture and a vertically aligned cylinder representing a 2D tumor phantom. (b) Tank filled with Triton x-100 and a full 3D breast phantom. [6]

Until now, the University of Manitoba has developed two generations of 3D-printed MRI-derived breast phantoms. [39, 47]. The hollow shells are filled with liquids selected to mimic the dielectric properties of breast tissues and for that Glycerin and a 30% solution of Triton X-100 were used. [47]

The difference between the first and the second generations 3D-printed MRI-derived breast phantoms are the bases of the fibroglandular shells to allow for greater freedom tumor analog positioning. [39]

The University of Manitoba created an open-access dataset, University of Manitoba Microwave Breast Imaging Dataset (UM-MWID) that contains the 3D-printable .stl files used to create the phantoms, which are used during this work. The dataset is available at `https://bit.ly/UM-bmid`.

1.3   Work highlights

Given the current status of the microwave imaging system developed by the Antennas and Propagation group of the Instituto de Telecomunicações, this thesis aims to analyze a set of anthropomorphic phantoms in order to test the set-up itself before proceeding to clinical tests, the continuation of the development of the graphical user interface that allows the user to interact with the entire setup, as well as the development of the physical set-up involving the integration of components such as switches to be able to associate the various antennas of the system in order to obtain various measures and in implementing strategies to make the interface itself, data acquisition and image reconstruction faster. Taking into account the objectives defined for this dissertation, during its development, several challenges arose to overcome. Regarding the implementation of switches to be able to connect the 8 antennas, there was some difficulty in finding a way to be able to calibrate the system, removing the impact of the coaxial cables that are connected between the switches and the antennas. Until now, the calibration was done regarding the coaxial cables that were directly connected to the VNA, as the system previously did not have the switches implemented. For this reason, one of my contributions was the implementation of switches, thus allowing to connect the 8 system antennas directly to the switches, whereas previously it was only possible to have two antennas to the VNA.

Before the development of this dissertation, the set-up had only been tested with few anthropomorphic phantoms and under particular conditions, that is, without the incorporation of such switches. One of the contributions of this work, is related to measurement and analysis of different anthropomorphic phantoms with different shapes and dimensions and using different antennas. Challenges arose for the analysis of denser and/or elliptical breasts, as the tumor was either not detected or had various artifacts around it, as the tumor response was masked. To this end, a study of the behavior of the antenna at a distance from a metallic target was carried out.

Given the enormous importance of the graphical user interface and the fact that it is not finished, the focus of this dissertation was also its development and improvement. During the work with the graphical interface, difficulties arose, namely, with pre-existing code, due to lack of familiarity and the need to implement action buttons in the application, improve the code in order to consider all scenarios, in order to avoid errors in the interface. The contribution also consisted in creating pages so that the user can

select the antennas, as well as select the respective scattering parameters and even save their VNA states or execute VNA commands directly through the interface, facilitating the process for the user.

This dissertation is divided into 6 chapters. The first chapter corresponds to the introduction and it has already been presented.

Since this dissertation is a bridge between telecommunications and medicine, it is presented, in chapter 2, some fundamental concepts about the breast anatomy and breast cancer. Chapter 2 is also dedicated to the analytical formulation, where it is explained a radar-based wave migration algorithm for breast cancer detection, in the frequency domain and the artifact removal algorithm, which is responsible for removing the early-time reflections between the air and the breast.

Chapter 3 presents the numerical results of the study of the behavior of the Crossed Exponentially Tapered Slot (XETS) antenna depending on distance to the metallic target,in order to understand the impact of the antenna near and farther from the breast skin on the experimental results and consequently on the images obtained.

Chapter 4 presents the experimental results and it is sub-divided into two sections, the first one presents the different measurement of signals using phantoms anthropomorphic, where almost of them were provided by Manitoba University and the imaging results for that phantoms obtained for different scenarios. The second topic is related with the IT's Breast Scanning Setup and the Graphical User Interface. Finally, Chapter 5 draws the main conclusions of this work, which includes future work description.

2

Fundamental Concepts and Analytical Formulation

Contents

2.1 Fundamental Concepts

Since this dissertation is a bridge between telecommunications and medicine, it is useful to address some concepts superficially about the breast anatomy. This information will help to visualize and understand what parts of the breast are being addressed throughout the dissertation.

2.1.1 Breast Anatomy

The breast is a highly complex part of the human body, it goes through many changes over a lifetime and its development is a vital part of a woman's reproduction. Breast development happens in certain stages during a woman's life: first before birth, again at puberty, and later during childbearing years. Changes also happen to the breasts during the menstrual cycle and when a woman reaches menopause [7].

During puberty, the production of hormones, such as estrogen and progesterone, stimulates the growth of milk ducts in the breast and the formation of the milk glands. When a woman becomes pregnant, she experiences some changes, such as the enlargement of the breast due to the production of the hormone progesterone that stimulate the milk-producing lobules [48, 49].

The overall anatomy of the female breast is presented in Figure 2.1.
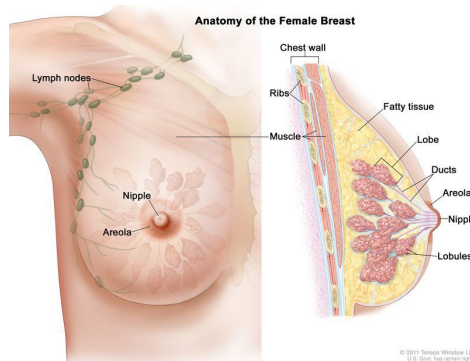
Figure 2.1: Anatomy of Female Breast. [7]

The female breast is mostly made up of a collection of fat cells called adipose tissue, with low water-content and lower dielectric properties. The primary function of fat cells, or also known for adipocytes, is to store energy as fat. Furthermore, the adipose tissue contains a stromal vascular fraction which is constituted by vascular endothelial cells, immune cells and fibroblasts. This tissue extends from the collarbone down to the underarm and across to the middle of the ribcage [8]. In Figure 2.2(a), it is possible to observe the adipose tissue.

Another essential structure in the breast are the lobes, glandular structures with high water content and dielectric properties. A breast usually consists of 15 to 20 lobes with small lobules in them. Each lobe is an aggregate of smaller lobules. These lobules consist of milk-producing glands, fibrous and fatty
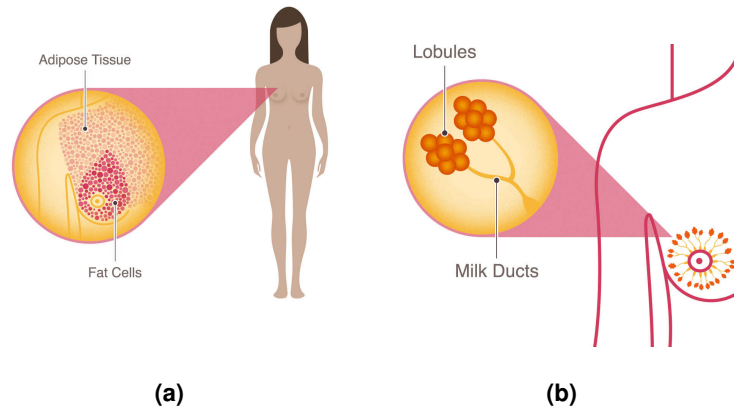
Figure 2.2: Adipose Tissue composed by adipocytes[2.2(a)]. Mammal Gland (Lobes) and Ducts.[2.2(b)] [8]

tissue [7, 50]. Both the lobes and lobules are connected by milk ducts, which act as tubes to carry the milk to the nipple. These breast structures are generally where the cancer begins to form. The nipple is located at the centre of the areola, the dark area of skin surrounding the nipple [8]. In Figure 2.2(b), it is possible to observe the mammal gland (lobes) and the ducts.

Finally, the breast and armpit contain lymph nodes that belong to the lymphatic system - a network of nodes and tubes that drain fluid (lymph) and transport white blood cells (immune cells involved in fighting against infections) [7].

2.1.2 Breast Cancer

Healthy cells are the basic building blocks of all tissues in the body. Normal cells are programmed to grow and divide in a controlled and orderly manner as they reach the end of their life cycle [7]. However, this process sometimes does not go as expected, so the cell's genetic material (Deoxyribonucleic Acid (DNA)) is damaged or altered, with mutations that affect cell growth, division and death. So on the one hand there are cells that grow and divide without any control and on the other hand there are cells that should die and they don't [51]. As the sickest cells do not die when they should and continue to generate more when the body no longer needs them, they start to accumulate in masses that in turn do not work. This mass of sick and damaged cells is called a tumor.

Breast cancer, usually, starts in the ducts that carry milk to the nipple (called ductal carcinoma), or within the lobules (called lobular carcinoma). In rare cases, other cancer types can also occur in the breast, such as sarcomas (cancer of the soft tissues) or lymphomas (cancer of the lymphatic system) [7].

Cancerous tissues have high dielectric properties, but although early studies indicated a very high contrast between healthy and cancerous tissues, recent studies demonstrated that the dielectric properties of cancerous tissues and healthy glandular tissues may overlap with very little contrast. [13] It is important to note that microwave image detection methods are based on detecting this contrast.

2.2 Analytical Formulation

This section presents the image reconstruction algorithm, which is based on the reflection field at each point of the volume of interest and the artifact removal algorithm , that is responsible for removing the early-time reflections between the air and the breast, which corresponds to the breast skin. This section also addresses different metrics in order to measure image quality.

2.2.1 Migration Algorithm

The presented method in this section, whose name is Matched Filter, is based on wave migration, which "back-propagates" the wave-front. The migration algorithm accounts for the phase-delay of the propagating wave.

The wave transmitted by the antenna travels through the medium until some of its energy is reflected by the target back to the same antenna (in monostatic system) or to a different antenna (bi or multi-static system). The reflected wave is received by the antenna with phase $-2jknd$, where k is the wave number, $\frac{2\pi}{\lambda}$, n is the refractive index of the travelling medium and d is the distance at which the target is. The electric field expression for a monostatic antenna configuration is given by equation 2.1.

$$E = E_0 e^{-2jknd} \tag{2.1}$$

In order to find where the target is located, the imaging algorithm considers a "search" volume, which contains the target, as shown in Figure 2.3. Each point of that volume is a possible scatterer which reflects the energy coming from the transmitted wave. [52]
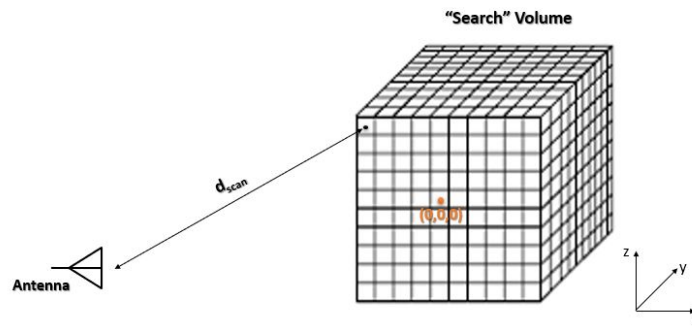
Figure 2.3: "Search" volume containing the target. Each focal point scatters the signals transmitted by the antenna.

The vector distance from each antenna location, $(P_{Ant_{x(i,j)}}, P_{Ant_{y(i,j)}}, P_{Ant_{z(i,j)}})$ to each point of the virtual grid (G_x, G_y, G_z) is calculated using the equation 2.2 in order to create estimated data set.

$$d_{scan(i,j)} = \sqrt{D_x^2 + D_y^2 + D_z^2} \tag{2.2}$$

19

where $D_x = P_{Ant_{x(i,j)}} - G_x, D_y = P_{Ant_{y(i,j)}} - G_y$ and $D_z = P_{Ant_{z(i,j)}} - G_z$. The migration algorithm tests each focal point individually and if the distance of the scan point to the antenna,d_{scan}, matches the distance of the target,d_{target}, it is possible to cancel the phase of the reflected wave by compressing the phase by $+2jkd_{scan}$. Thus, the imaging algorithm used is extremely computationally efficient and it is robust enough to overcome errors during the measurements.

In order to obtain a detection of the target, the algorithm consists in, for every point of the "search" volume, multiplying the phase of the reflected wave by the frequency dependent S-parameters, for each position of the antenna a, as shown in Equation 2.3.

$$E = \sum_r |\sum_{i,j} E_0 e^{2jk_r d_{scan(i,j)} \times n} s_{11(i,j)}| \tag{2.3}$$

where r is the index of frequencies, s11 is complex, n is the index of refraction and (i,j) is the index of the antenna position. The propagation constant k is given by Equation 2.4.

$$k = \omega\sqrt{\mu\varepsilon} = \sqrt{\mu_0\varepsilon_0\varepsilon r} = \frac{\omega}{c}\sqrt{\varepsilon_r} \tag{2.4}$$

where ε_r is the permittivity of the medium. This permittivity is a complex number, where the imaginary part corresponds to the losses and attenuation caused by the tissues. The ratio between the reflected field,E, and the incident, E_0, is related to the measured complex-valued s parameter.

In microwave imaging, in measurements and simulations and in order to guarantee that the algorithm processes uniquely the scattered signal from target, it is necessary the realization of a calibration procedure. Thus, in order to isolate the desired signal, it is necessary to subtract the antenna reflection characteristic from the simulated data.

The calibration procedure is the ideal, subtracting the reflection coefficients from the configuration with the target and the reflection coefficients from the scenario without the target according to Equation 2.5. It is important to note that this procedure cannot be used in a real environment, but it is used here to allow testing the migration algorithm without being masked by other effects.

$$S_{11(i,j)} = S_{11data(i,j)} - S_{11calibration(i,j)} \tag{2.5}$$

where $S_{11data(i,j)}$ and $S_{11calibration(i,j)}$ are data obtained and (i,j) is the index of the antenna position.

In order to obtain a detection of the target for this stage, the algorithm consists in, for every point of the "search" volume, multiplying the phase of the reflected wave by the frequency dependent S-parameters, for each position of the antenna, as shown in Equation 2.6.

$$Image = \sum_r |\sum_{i,j} S_{11final(i,j)} \times e^{2jk_r(d_{scan(i,j)}+d_{ant})}| \tag{2.6}$$

where r is the index of frequencies, s11 is complex, n is the index of refraction of the respective medium, (i,j) is the index of the antenna position and d_{ant} is the electrical distance of the antenna.

2.2.2 Artifact Removal Algorithm

Since the value of permittivity contrast between skin and air is high, the received signals are dominated by this early-time reflection. The artifact is larger in magnitude than the tumor response, which can mask the tumor and prevent its detection. In order to avoid this, it is necessary to remove or at least reduce the early-time response from the skin. This processing step is known as artifact removal.

One way to mitigate backscattering of the skin is to immerse the breast in a coupling medium. [53] However, in the setup presented in this thesis, the patient is in the prone position with the breast pendant inside a cavity, requiring no immersion liquid. The contactless approach simplifies the setup, avoids lengthy sanitation procedures during the exam and especially favors patient comfort.

The dry setup presents challenges to overcome, namely the removal of the skin artifact that increases due to the concomitant absence of matching liquid or even the non-uniform shape of the breast. In order to deal with the challenges addressed, some strategies were developed, namely an iterative and adaptive algorithm based on a Singular Value Decomposition (SVD) that effectively removes the skin scattering under the conditions mentioned above. [19, 54]

The SVD corresponds a fast and real-time artifact removal algorithm used in the calibration, which decomposes the measured data into a set of reflections, allowing removing the stronger echoes created by the breast skin, without influencing the tumor position. [19]

Breast shape is a factor influencing artifact and image removal algorithms, meaning that symmetrically shaped breasts make the algorithms simpler. However, the assumption of symmetry of a breast is unrealistic and leads to inadequate results considering a real context.

In order to ensure that the unwanted antenna internal reflections are removed from the scattered signals, the signal processing considers that the signals retrieved in the presence of the breast are subtracted by the free-space antenna input reflection coefficient.

Figure 2.4 represents a propagation scenario considering a antenna *a* and one neighbour antenna, *a-N1,a+N1*, on each side of the selected antenna,*a*. d_s^{init} corresponds to the shortest distance between the antenna and the breast skin,d_t, the distance from the skin to the tumor and d_s^{back}, the physical distance between opposite walls of the breast. Ts corresponds to the transmission coefficient of the skin and Γ_s^{init},Γ_s^{back} and Γ_t are the reflection coefficients of the front skin interface, opposite skin interface, and tumor, respectively.

In the absence of noise, the measured signals for example for antenna *a* in Figure 2.4 are given by
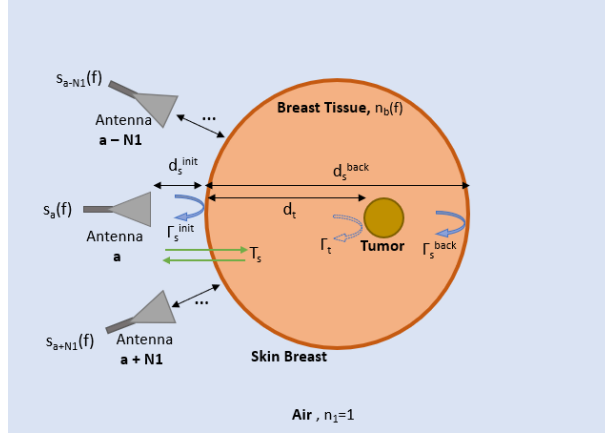
Figure 2.4: Sketch of the antenna symmetry and a simplified propagation scenario for one antenna and its neighbours.

the equation 2.7.

$$s_a(f) = c^{init}exp(-2jk_0d_s^{init}) + c_t exp[-2jk_0(d_s^{init} + n_b d_t)] + c^{back}exp[-2jk_0(d_s^{init} + n_b d_s^{back})] \quad (2.7)$$

where $c^{init} = \chi^{init}\Gamma_s^{init}$, $c_t = \chi_t T_s^2 \Gamma_t$ and $c^{back} = \chi^{back}T_s^2\Gamma_s^{back}$ are coefficients associated to the reflection, transmission and dissipation losses, respectively. χ is the radial spreading of the propagation spherical wave. [54].

Therefore, it is possible to have the S_a matrix for the input reflection coefficients for the selected antennas, according to the number of neighbors defined, N_n, as seen in the equation 2.8.

$$S_a = [s_{a-N_n}...s_a...s_{a+N_n}] \quad (2.8)$$

The equation 2.9 represents an optimal approximation of SVD, which factorizes matrices. [54]

$$M_q = \sum_{i=0}^{q} \sigma_i u_i v_i^H \quad (2.9)$$

where (σ_i, u_i, v_i) are the first q singular values, left singular vectors, and right singular vectors, decreasingly ordered value of σ_i.

The equation 2.10 represents the calibration matrix, S_a^{cal} (i.e. without the skin artifact) is obtained by subtracting the matrix for the input reflection coefficients by the unwanted q scatterers.

$$S_a^{cal} = S_a - M_q \quad (2.10)$$

S_a^{cal} contains the response of the tissues inside of the breast considering a specific position of the antenna. In order to eliminate all the reflections from the skin, all the q coefficients that describe the skin

are erased from the S_a matrix in order to reach the tumor signal. The value of q varies depending on the antenna, since the distance from the tumor to the respective antenna is different, as skin reflections in each breast point, due to the breast not being symmetrical. [19, 54] As the value of q increases the power of the signal decreases, which can correspond that the weight of the specific signal will decrease in the reconstruction of the image.

2.2.3 Image Quality Metrics

Most image quality metrics, that is performance metrics aim to measure the contrast between the tumor response and clutter responses in the image. Fibroglandular tissues of the breast have high values of dielectric properties compared to adipose tissues, and clutters are directly related to their presence. [55]

In order to quantitatively analyze the images reconstructed from the processing of measurements acquired using the phantoms anthropomorphic, three image performance metrics were used, namely the Positioning Error (PE), Tumor-to-clutter Ratio (TCR) and Tumor-to-mean Ratio (TMR) to assess the quality of the received signals and the image reconstruction, as seen in the table 2.1. [2]

Table 2.1: Performance metrics used to assess the qualify of the received signals and the image reconstruction [2]

Performance Metrics	Description
Tumor response magnitude,T	Measure the intensity of the tumor response in the final image.
TCR	Measure T relative to the largest intensities of the background clutter of the image,C
TMR	Measure T relative to the mean intensities of C.
PE	Quantify the deviation of the detected tumor relative to the actual coordinates.

In log units, TCR and TMR are computed as presented in equations 2.11 and 2.12, respectively.

$$TCR[dB] = 10log_{10}[max(T)/max(C)] \tag{2.11}$$

$$TMR[dB] = 10log_{10}[max(T)/mean(C)] \tag{2.12}$$

The TCR and TCR provide a measure of the contrast between the clutter and the tumor responses in the reconstructed images. A negative TCR indicates that the maximum response present in the image occurred outside the known tumor region, which means that the tumor response in the final image is not identifiable based on its intensity. [55] The Positioning Error is defined in equation 2.13

$$PE = ||P_{tumor} - P_{detected}|| \tag{2.13}$$

where P_{tumor} is the known tumor position and $P_{detected}$ is the position of the maximum response in the reconstructed image.

3

Numerical Results

Contents

This chapter addresses the numerical results of the study of the behavior of the Crossed Exponentially Tapered Slot (XETS), ultrawideband antenna , [56], depending on distance to the metallic target. The XETS antenna is used in the measurement of signals acquired with different phantoms anthropomorphic and which is presented in the chapter 4.

3.1 Design Description

During the experimental analysis, different breasts phantoms anthropomorphic were measured using a VNA. The breasts differ in shape and dimensions, with, for example, some breasts being more elliptical than others. After obtaining the dispersion data, it was found that despite the ideal calibration method perfectly detecting the tumor, the SVD algorithm did not detect the same in some breasts, namely large and/or elliptical breasts.

Antennas play a very important role and strongly influence the image generation process, as they need to operate in close proximity to the breast itself. Due to the extreme proximity of the antenna to the breast, there is a need to study the antenna, in order to understand which are its characteristics that have to be accounted for in the post-processing of the image signal itself.

In order to understand the impact of the distance from the antenna to the breast skin on the results obtained, we resorted to the Computer Simulation Technology (CST) Microwave Studio. [57] The antenna used is the XETS antenna and since it works between 2.4 GHz and 4.8 GHz [52], the frequency interval considered was between 2 and 5 GHz.

In the CST, a setup was developed consisting of the antenna used in the laboratory, XETS, and a rectangular parallelepiped metal target, whose dimensions are $160 \times 160 \times 2mm^3$, as shown in Figure 3.1. The XETS antenna is 5mm away from the metal target and it was important that the rectangular target was metallic in order to reflect all the incident power and with that it was possible to determine the antenna distance and the metal plate answer.
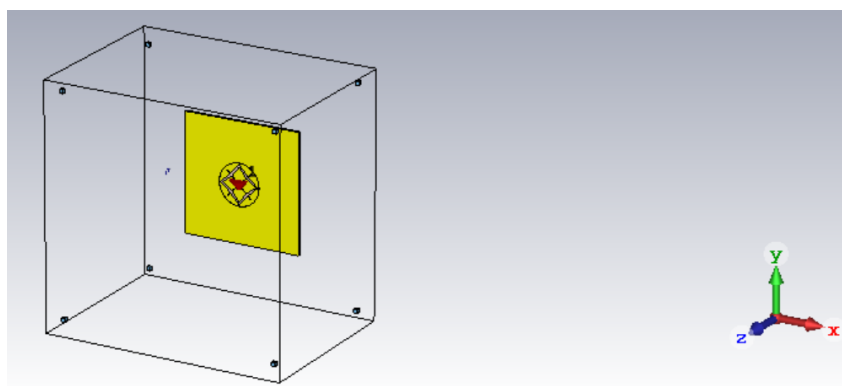
Figure 3.1: Perspective View of XETS antenna and metallic target.

In Figure 3.2, it is possible to see the XETS antenna and the metallic plate in the Z and X planes.
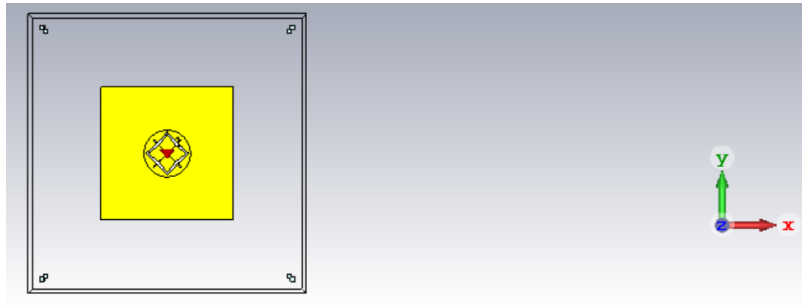
(a) Metallic Target and XETS antenna in the z plane.
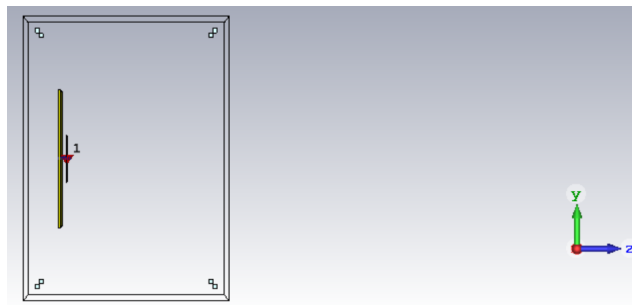
(b) Metallic Target and XETS antenna in the x plane.

Figure 3.2: Front and Left view of the CST setup.

As far as the simulations are concerned, two simulations were made, one considering the metallic target and one not considering the target. The second simulation corresponds a free space measurement, thus it was made by the subtraction of the reflection coefficients from the free space setup, that is, the one without the target, to the setup considering the target.

Through the **CST**, a linear scan of the position of the antenna in relation to the metallic target was performed between 5mm (initial position of the antenna) and 125 mm (final position of the antenna), every 1 mm, which corresponds to 121 positions of the antenna, in order to obtain the reflection coefficients for each of these positions.

The XETS antenna is formed by two crossed exponential tapered slots that intersect a square slot and due to its symmetric geometry, the antenna tends to exhibit a stable radiation pattern versus the frequency with stable phase center as well as low pulse distortion.

The material used for the target is copper, as it is an electrical conductor and has an electric conductivity of $5.8 \times 10^7 S/m$.

After having configured the model geometrically and assigned the appropriate power source, as well as the boundary conditions in CST STUDIO SUITE, the model has to be translated into a computer-accessible format, this means that for the case of CST, it uses a method of volume discretization, in

which its calculus domain has to be subdivided into small cells on which the Maxwell's Grid Equations must be solved. The mesh strictly influences the accuracy of the data obtained, in addition to the simulation speed.

In order to keep the mesh as static as possible for the two simulations, with and without a metallic target, depending on the distance between the antenna and the target, eight vacuum cubes were placed at a distance greater than the maximum distance from the antenna to the metallic plane, i.e., $d = 126mm$.

3.2 Simulation Results

As discussed in the previous section, two simulations were performed, one with the metallic target and the other without the target, that is, free-space.

After obtaining the reflection coefficients for each of the antenna positions and for the two simulations referred above, the simulation results were analyzed and for this the Matched Filter algorithm was used.

The reflections coefficients for the simulations are subtracted in order to remove the influence of the surrounding environment, since the only difference between the both simulations referred above is the presence of the metallic target.

Through the Matched Filter algorithm, it was possible to visualize the different graphs of the reflected power as a function of the distance for different positions of the antenna in relation to the metallic target.

By analyzing the multiple graphs and using computational tools, namely MATLAB, it was possible to determine the different distances for the maximum in the graphs. The maximum value represents the position of the metallic plane.

In Figure 3.3, it is possible to visualize the relationship between the physical distance from the antenna XETS to the metallic target and the maximum distances discussed above for a frequency of 2 to 5 GHz. It is also possible to visualize in Figure 3.3, in green, the straight and dotted line resulting from the simple linear regression process, which describes the relationship mentioned above.

Analyzing Figure 3.3, it can be seen that as the XETS antenna moves away from the metallic plate, the values obtained from the relationship tend to approach the simple regression line, reducing the deviation of the points from the line. If the antenna is approached to the metallic target, it is verified that the points obtained present a sinusoidal behavior compared to the simple regression line.

In order to understand the deviation of the target's position from its physical position, we proceeded to graph the difference between the different points in Figure 3.3 in relation to their position in the linear regression line for the frequency band from 2 to 5 GHz, as shown in Figure 3.4.

By analyzing Figure 3.4, it can be seen that for the 2 to 5 GHz frequency band, the metallic plate can be deviated up to $\pm 3.6mm$ from its physical position. If we consider the case of the XETS antenna distanced from the breast with the tumor instead of the metallic plane, the result obtained in Figure 3.4
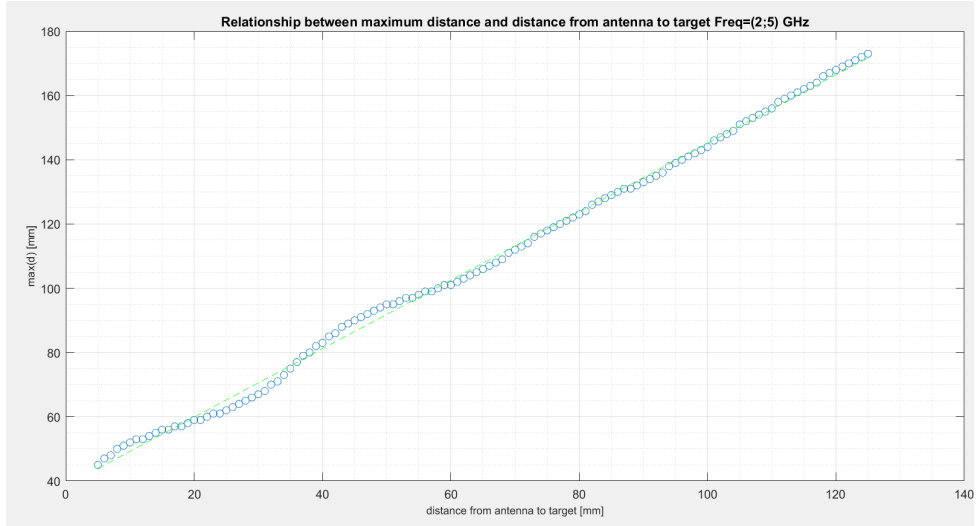
Figure 3.3: Relationship between maximum distance and the distance from antenna to the target for a frequency of 2 to 5 GHz.
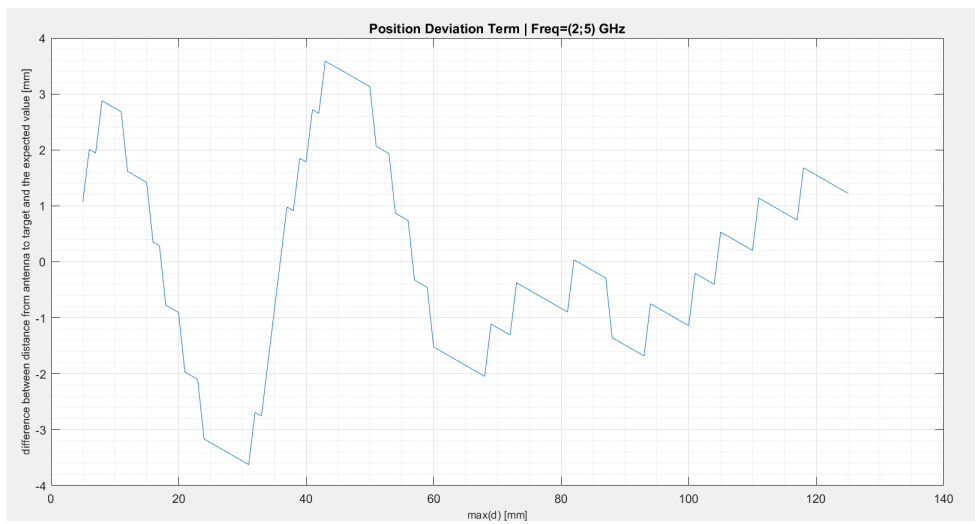
Figure 3.4: Position Deviation Term for a frequency of 2 to 5 GHz.

reflects the situation that when using the algorithm to reconstruct the image of the breast with the tumor, the breast skin may appear in the image shifted from its original position, which leads to the tumor also being deviated.

Through the analysis of the Figure 3.4, it can be seen that the deviation from the target position decreases as the antenna moves away from the metallic target and the behavior of the graph may be related to the presence of a standing wave, formed by the superposition of two identical waves, but in opposite directions, derived from the metal plate that reflects the signal to the XETS antenna again.

4

Experimental Results

Contents

This chapter is divided into two sections. In the first section, different sets of phantoms anthropomorphic, where some of them were provided by the University of Manitoba, are measured and image reconstruction of these phantoms using the IT MWI reconstruction algorithm.

Regarding the second section, this consists of the description of the MWI IT image acquisition setup, as well as in the further development of an user-friendly graphical user interface, that in turn interacts directly with the user and operates the configuration, which creates a bridge between the setup and the technicians and doctors to perform the examination. It is noteworthy that some part of the interface has already been developed in previous works. [18, 19]

4.1 Measurement of Signals acquired with Phantoms anthropomorphic

As mentioned above, different breast phantoms will be covered in this section. The breast phantoms were experimentally measured using an Agilent E5071C vector network analyzer.

In order to construct the printed breast phantom model, it is important to create a volumetric binary mask, which differentiates between air and the solid plastic void regions. For this, it is necessary to remove the numerical phantom's skin layer and segment all the regions.

The image reconstruction algorithm used to reconstruct all the images presented in this section uses a 5mm distance between pixels and an average dielectric permittivity for the phantom of 4.2.

In this setup no breast immersion liquid is used in order to favor a future more practical examination scenario, faster and comfortable for the patient.

The present section considers homogeneous breasts, i.e. breasts composed of adipose tissue only, without fibroglandular tissue. Table 4.1 presents a summary of almost of breast phantoms' characteristics.

Table 4.1: Summary of breast phantoms anthropomorphic and homogeneous used to measure signals. The breast's dataset and the information are provided by Manitoba's University at https://bit.ly/UM-bmid.

Breast	Shell Volume $[mm^3]$	Breast Length $[mm]$	Mean Shell Radius $[mm]$	Antenna(s) Used
A1	294710	77.63	34.6	XETS
A2	729324	115.4	43.8	CABAVA, XETS
A3	1113320	138.2	51.6	XETS
A12	567850	94	42.5	XETS
A14	713177	97	48.2	XETS

Figure 4.1 represents all the breast phantoms anthropomorphic used to measure signals.
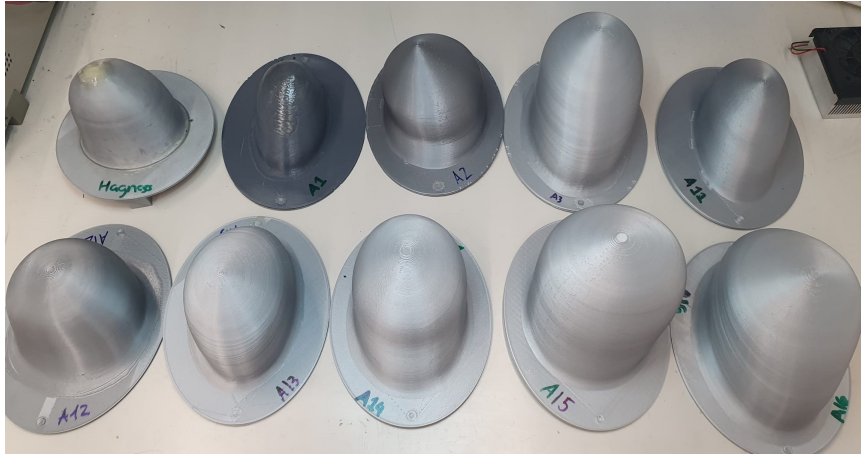
Figure 4.1: Breast phantoms anthropomorphic and homogeneous.

4.1.1 Hagness Breast

The first experimentally measured breast phantom was the Hagness, that is a 3-D-printed Polyactic acid (PLA) shell ($\varepsilon_r \approx 2.75 - j0.03$ at 4 GHz), obtained from the University of Wisconsin–Madison breast repository [52].

In figure 4.2, it is possible to visualize the exterior of the phantom in an xOz plane and for that a .stl file of the phantom was needed, which contains all the information about the 3D model of the phantom.

In order to obtain the Hagness breast mask, the CST was initially used to center the breast by its base, as shown in figure 4.2 and orient it according to the coordinates defined during the measurement in the laboratory.

Figure 4.3 represents the Hagness breast mask in different planes and by analyzing it, it can be seen that it is a homogeneous breast.

During the experimental analyzes, the Hagness breast phantom was filled with a Triton X-100 surfactant solution, which has a relative permittivity of approximately 4.2 and the tumor containers were filled with a mixture of TX-100, distilled water and sodium chloride of different percentage of each ingredient in order to mimic the dielectric properties of biological tissues. A biologically relevant contrast between the Hagness breast plastic and the solution can be achieved by choosing an appropriate ratio between Triton X-100 and distilled water. [6]

This chapter on the Hagness Breast is divided into two sub-chapters: BAVA antenna and XETS antenna, as they correspond to different experimental analyzes with different antennas, as it is possible to see below.

The tumor was inside the breast phantom and three different tumor position were concerned for each of the two experimental analyzes. The tumor is represented as 10 mm x 20 mm ellipsoidal shape for the scenario with BAVA antenna. If it is considered the XETS antenna, the tumor is represented as 10mm x
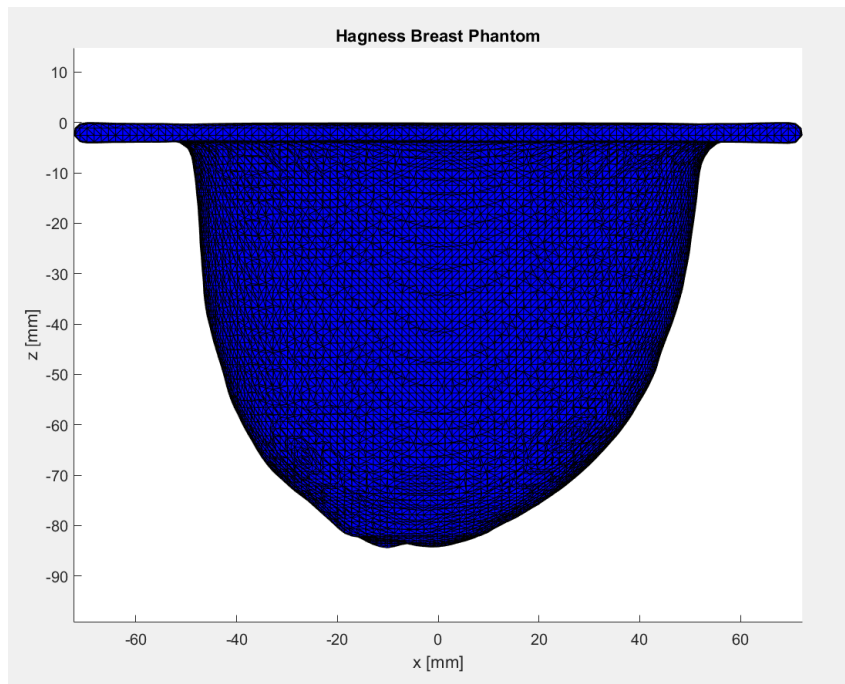
Figure 4.2: Representation of the Hagness breast phantom in the xOz plane, that is the anthropomorphic exterior of the phantom. [9]
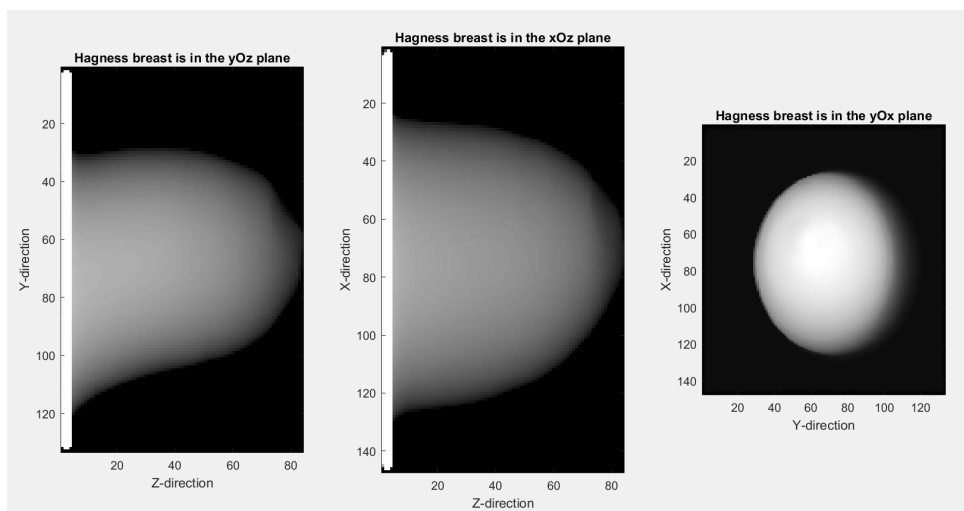
Figure 4.3: Representation of the Hagness breast in different planes.

10 mm circular shape since the tumors are different for the two experimental scenarios.

4.1.1.A BAVA antenna

The first experimental analysis with Hagness breast phantom used a Balanced antipodal Vivaldi antenna (BAVA), a compact, low-cost antenna that is simple to manufacture and features relatively high gain radiation patterns, used in broadband designs and that is ideal for systems that are based on radar. The antenna substrate is a Rogers RT58880, with a thickness of 0.254 mm and whose dielectric properties are $\epsilon_r = 2.2$ and $tag(\delta) = 0.0009$. [18] BAVA has a radiation pattern relatively directive at higher frequencies.

In this experiment, a linear sweep of the antenna rotation angle between 0º and 360º was performed every 15 degrees, which corresponds to 24 BAVA antenna positions, in order to obtain the reflection coefficients for each of the three tumor positions. It is important to note that the BAVA antenna rotates clockwise around the breast.

The figure 4.4 summarizes everything that was discussed and corresponds to a representation of the 24 BAVA around the Hagness breast phantom distanced from the center of the breast (R).

As mentioned, three tumor positions were used in these measurements. The first had the central coordinates in $(x_t, y_t, z_t) = (17, 5, -30)mm$, the second corresponded to $(x_t, y_t, z_t) = (-20, -15, -30)mm$ and the third was defined in $(x_t, y_t, z_t) = (-27, 12, -30)mm$.
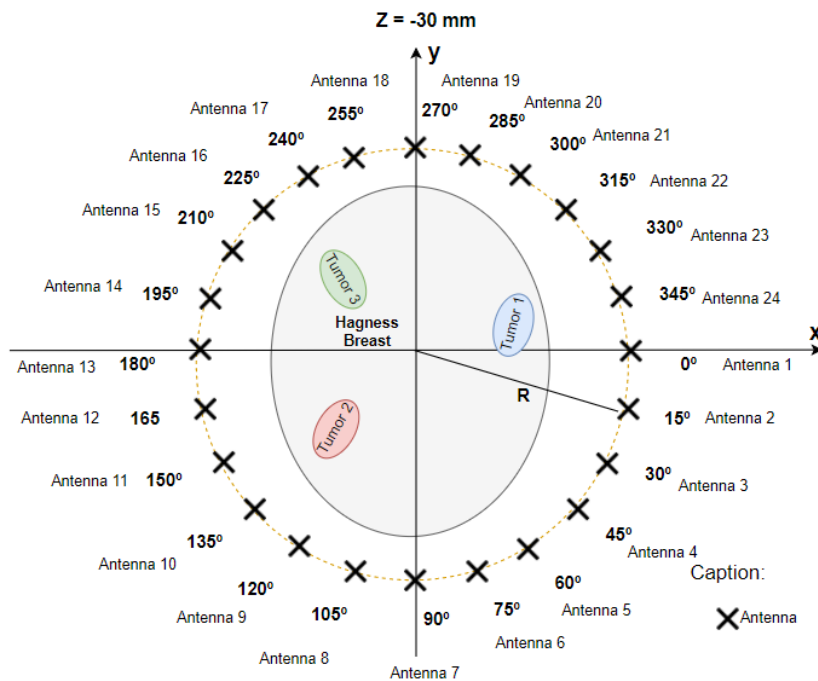
Figure 4.4: All 24 antennas around the Hagness breast phantom, where R is the distance between the center of the breast and the position of the antenna.

Before inserting the tumor container inside the Hagness breast phantom, a free space measurement was performed for each antenna position, in order to determine the distance introduced by the antenna, which is d_{ant} mentioned at equation 2.6, an important parameter for image reconstruction, as it is added to the position of the target's response, causing a translation of its position.

In order to obtain the image reconstructed, it is important to calibrate the measurements and two different methods were used which are the ideal calibration and the SVD.

The ideal calibration corresponds to the subtraction of the measurements obtained with the tumor inserted in the Hagness breast from the experimental measurements without the presence of the tumor. The reflection map resulting from the subtraction ideally corresponds only to the tumor response.

Since the ideal calibration cannot be used in real diagnoses, because it is not possible to obtain results with and without the tumor simultaneously, the SVD method emerged, a method that is able to obtain the tumor response in order to detect it and which was described in section 2.2.2.

If the calibration is not performed, the image reconstruction algorithm does not process uniquely the target reflections, since there are two issues fat and skin which compromises the effectiveness of the imaging algorithm.

In all the images that follow concerning the results obtained from the image reconstruction for each tumor position, it is possible to visualize the results according to the two methods mentioned above, that is ideal calibration and SVD methods.

In figure 4.5, it is possible to visualize the results obtained for a plane z= -30 mm considering Tumor 1 and for all 24 antennas using the ideal calibration and SVD, respectively.

(a) Ideal Calibration **(b)** SVD
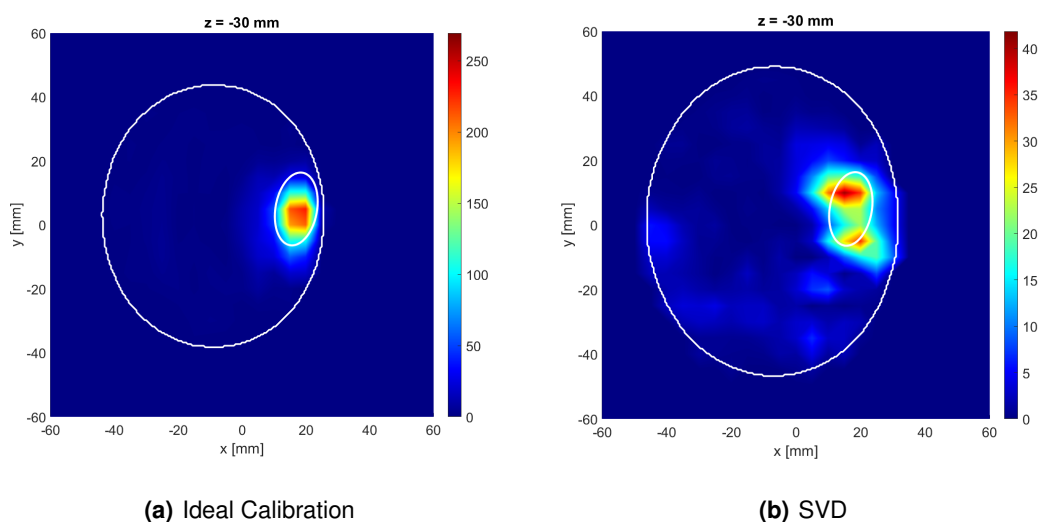
Figure 4.5: Imaging results for the plane z=-30mm considering the Tumor 1, all antennas and using 4.5(a) the ideal calibration 4.5(b) the SVD. The white lines translate the border of the breast with the air and the border between the tumor and the fat.

At it is possible to verify at figure 4.5(a), the tumor can be clearly detected using Ideal Calibration, without any presence of clutter. Through the application of the SVD method with 4 neighbours it is found that despite the detection of the Tumor 1 being achieved near the real position of the tumor, there is some clutter surrounding the area, which can mask and lead to false results.

The result obtained using the SVD method may be due to the relative proximity of the tumor to the breast skin and that, as it has a dielectric constant that is approximately 10 times greater than that of the tumor, it may contribute to the presence of clutter.

The second step was the reconstruction of the image for Tumor 2 using the two methods mentioned above and the results can be seen in figure 4.6. By observing figure 4.6(a), it is possible to verify that Tumor 2 is detected using the ideal calibration in the defined region for the exact position of the tumor, however there is some clutter spread in the image and the tumor is a little deviated from its original position.

(a) Ideal Calibration   **(b)** SVD
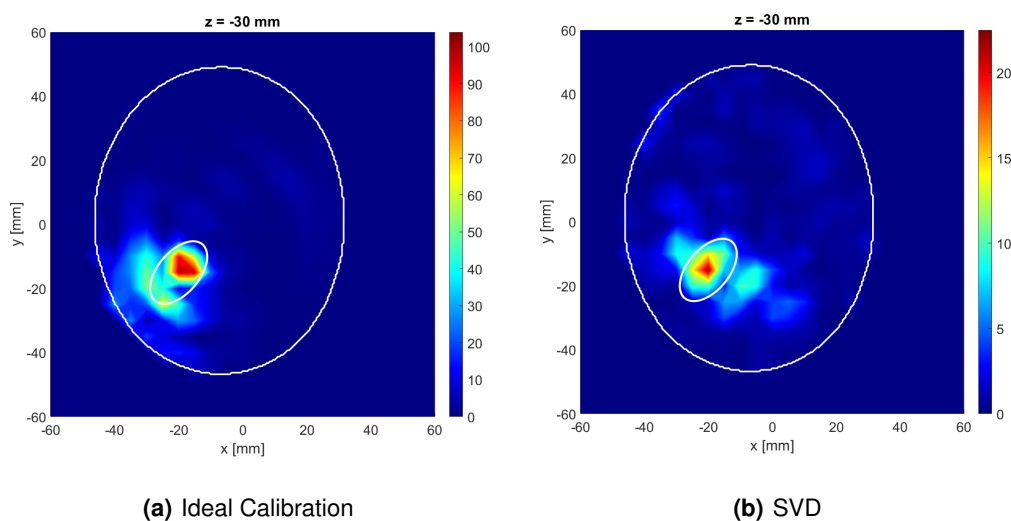
Figure 4.6: Imaging results for the plane z=-30mm considering the Tumor 2, all antennas and using 4.6(a) the ideal calibration 4.6(b) the SVD. The white lines translate the border of the breast with the air and the border between the tumor and the fat.

Regarding the image obtained using the SVD method with 4 neighbours, that is figure 4.6(b), it is possible to conclude that the tumor is equally detected, despite the area with greater intensity being small (tumor response) and there is the presence of clutter that interferes with the tumor response. Comparing the results in figures 4.6 and 4.5, the intensity decreased and more clutter appeared.

Figure 4.7 represents the results for the plane z = -30 mm considering Tumor 3 using the ideal calibration and the SVD for all 24 BAVA antenna's positions.

As can be seen in figure 4.7(a), the Tumor 3 can be detected using the Ideal Calibration and its not deviated, but there is some clutter near the tumor, which can be related with the high difference of the

(a) Ideal Calibration   **(b)** SVD

Figure 4.7: Imaging results for the plane z=-30mm considering the Tumor 3, all antennas and using 4.7(a) the ideal calibration 4.7(b) the SVD. The white lines translate the border of the breast with the air and the border between the tumor and the fat.

dielectric constant between the breast skin and the tumor. Finally, regarding the results obtained using SVD as a calibration method, that is 4.7(b), it is possible to detect clearly the presence of the tumor. However, there is some clutter surrounding the area that can mask the tumor.

4.1.1.B XETS antenna

In the second experimental measurements with the Hagness breast phantom, the XETS antenna was used instead of the BAVA. The XETS is a thin planar printed antenna and was developed at the Antennas and Propagation Group at Lisbon. The other aspects related with XETS antenna is that its a low-cost, light-weight and low-profile antenna. Furthermore, XETS is the ideal antenna candidate for microwave imaging systems.

Unlike the first experimental measurements, in which to obtain the reflection coefficients it was necessary to manually move the antenna around the breast according to a support, these second measurements used an Arduino Uno and a motor that allowed rotating the antenna in around the breast, making it easier to obtain measurements.

A linear sweep of the XETS antenna rotation angle between 0º and 360º performed every 9º, instead the 15º, as happened with the previous experimental measurements and analysis with the BAVA antenna. Considering the linear sweep of this second experimental measures, it appears that it corresponds to 40 XETS antenna positions, in order to obtain the reflection coefficients for each of the three tumor positions. It is important to note that the XETS antenna rotates anticlockwise around the Hagness

breast.

The Tumor used in the second measurements for the three positions was 3D-printed using conductive Polyactic acid (PLA) filament, usually known as "Proto-pasta", which presents $\varepsilon_r \approx 20 - j9$ at 4 GHz. The "Proto-pasta" has lower dielectric properties compared with a real tumor, but the contrast allows to distinguish it from the fat tissue. [58]

The figure 4.8 corresponds to a representation of the 40 XETS antennas around the Hagness breast phantom distanced from the center of the breast (R).

The central coordinates of the positions of Tumor 1, Tumor 2 and Tumor 3 used in these measurements are $(x_t, y_t, z_t) = (20, -15, -43.5)mm, (x_t, y_t, z_t) = (-20, -5, -43.5)mm$ and $(x_t, y_t, z_t) = (10, -20, -43.5)mm$, respectively.
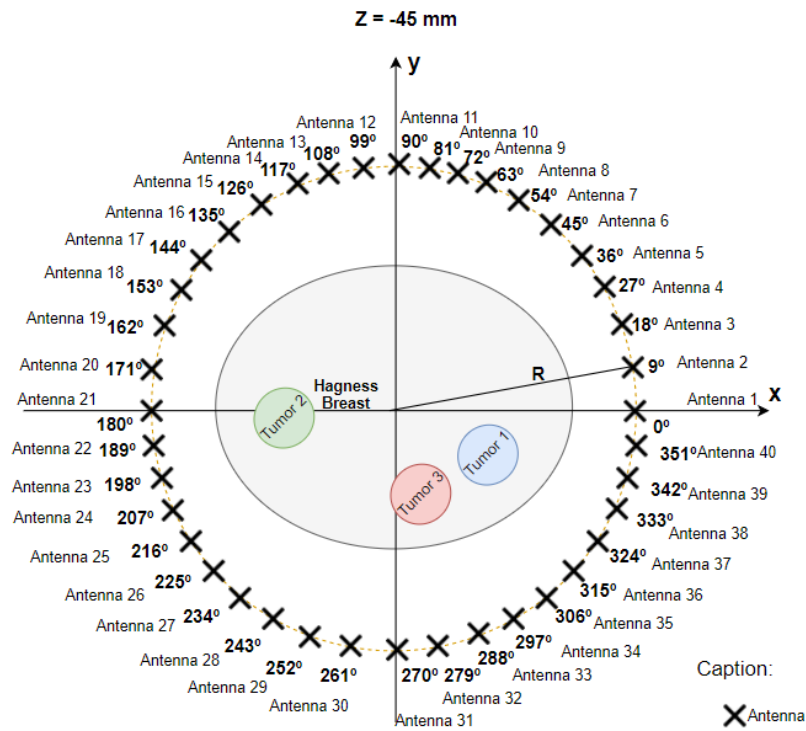
Figure 4.8: All 40 XETS antennas around the Hagness breast phantom, where R is the distance between the center of the breast and the position of the antenna.

Initially, measurements were taken in free-space for each position of the antenna without the presence of the tumor, which is important to know the distance introduced by the antenna. Afterwards, the tumor container was inserted inside the breast phantom and the measurements were taken in order to obtain the scattering parameters.

The images that appear below resulted from the application of a reconstruction algorithm and correspond to each tumor position and each calibration method, that is, the ideal calibration method and

SVD.

The results obtained according to the two calibration methods discussed above for the z = -45 mm plane considering Tumor 1 for the 40 XETS antennas can be seen in figure 4.9.
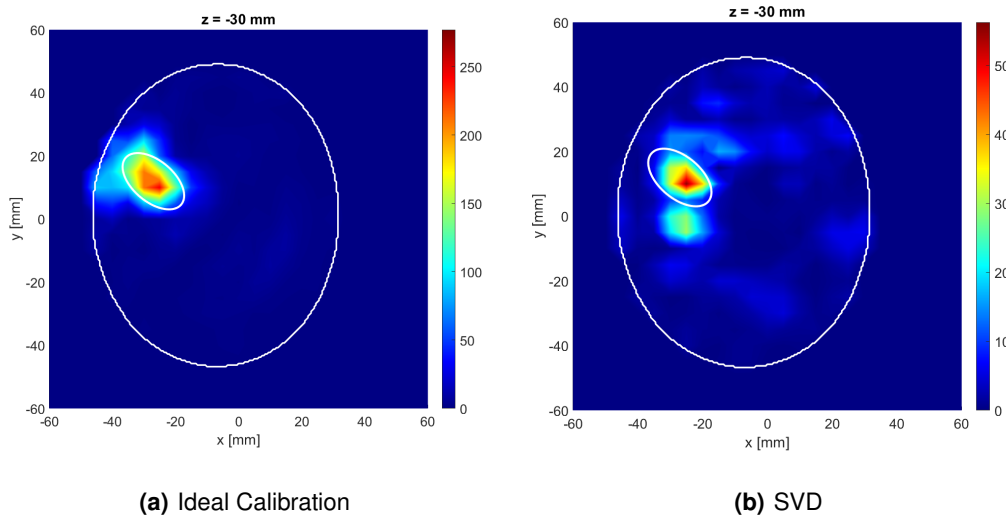

(a) Ideal Calibration **(b)** SVD
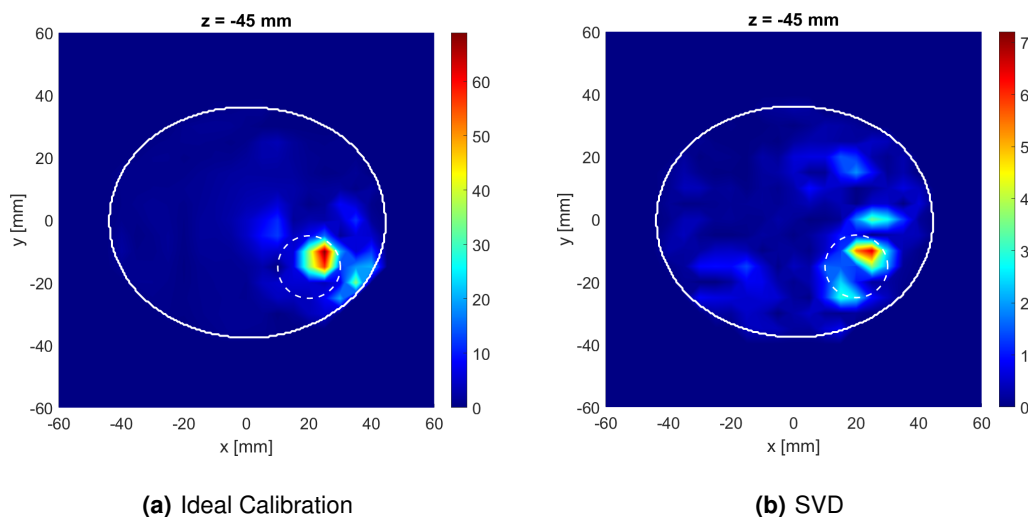
Figure 4.9: Imaging results for the plane z=-45mm considering the Tumor 1, all XETS antennas and using 4.9(a) the ideal calibration 4.9(b) the SVD. The white lines translate the border of the breast with the air and the border between the tumor and the fat.

By looking at figure 4.9(a), it is seen that Tumor 1 can be clearly detected using optimal calibration without the presence of any clutter, despite the tumor being deviated from its actual position. Regarding the application of the SVD method, as it is possible to see in figure 4.9(b), it appears that the tumor is detected, with a lower intensity than the ideal calibration, which makes sense, since the ideal calibration removes all interference between measurements with and without tumor. However, there is the presence of clutter close to the tumor.

Subsequently, the images for Tumor 2 were reconstructed according to the two methods mentioned above and the results can be seen in figure 4.10.

Using the ideal calibration method and according to figure 4.10(a), the detection of a slightly deviated Tumor 2 is verified. It is possible to detect Tumor 2 using the SVD method with 4 neighbours despite the marked presence of clutter, as it can be seen in figure 4.10(b).

Finally, the figure 4.11 represents the results obtained using the Ideal Calibration and SVD method considering the Tumor 3.

From the figure 4.11 obtained, it appears that Tumor 3 can be equally detected with both methods, despite the presence of clutters in the case of SVD, which can be related with high values of q singular values at SVD that will lead to the decrease of the power of the signal and consequently the tumor answer.

(a) Ideal Calibration   **(b)** SVD
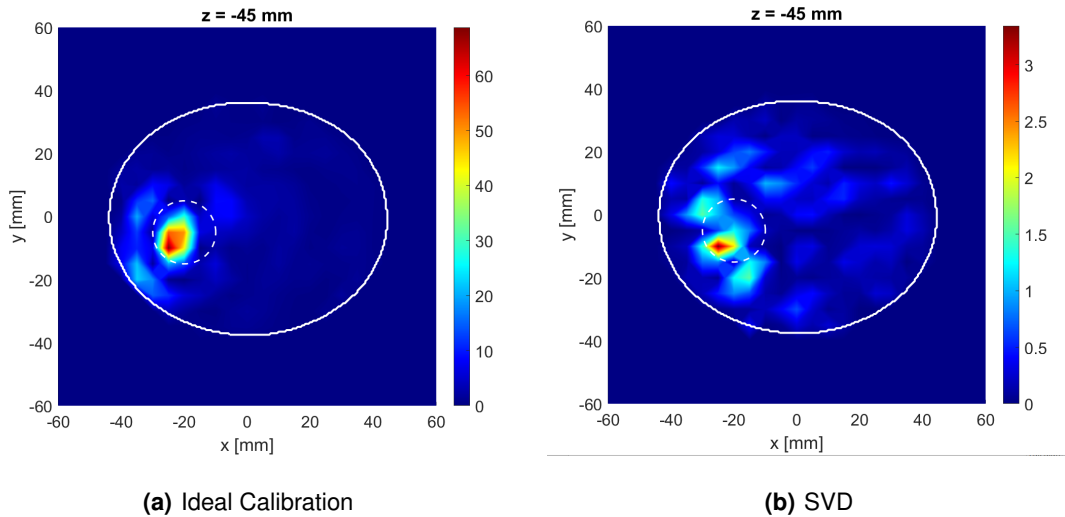
Figure 4.10: Imaging results for the plane z=-45mm considering the Tumor 2, all XETS antennas and using 4.10(a) the ideal calibration 4.10(b) the SVD. The white lines translate the border of the breast with the air and the white dotted line represents the border between the tumor and the fat.

(a) Ideal Calibration   **(b)** SVD
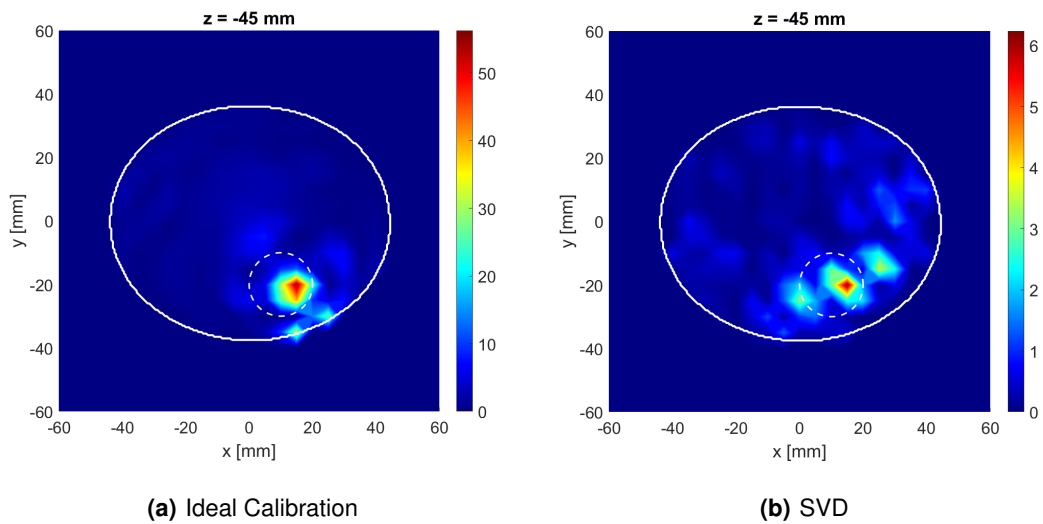
Figure 4.11: Imaging results for the plane z=-45mm considering the Tumor 3, all XETS antennas and using 4.11(a) the ideal calibration 4.11(b) the SVD. The white lines translate the border of the breast with the air and the white dotted line represents the border between the tumor and the fat.

The metrics calculated in the Hagness Breast using XETS antenna, which was discussed before, are summarized in Figure 4.12.

|		Tumor 1		Tumor 2		Tumor 3	
		Ideal Cal.	SVD	Ideal Cal.	SVD	Ideal Cal.	SVD
Positions (x_t, y_t, z_t)	Actual	(20, −15, −43.5)		(−20, −5, −43.5)		(10, −20, −43.5)	
	Detected	(25,-10,-45)	(20,-10,-50)	(-25,-10,-50)	(-25,-10,-45)	(15,-20,-60)	(15,-20,-50)
	PE	7.228	8.201	9.605	7.228	17.241	8.201
	TCR [dB]	3.9123	2.344	4.948	2.689	2.317	2.038
	TMR [dB]	6.343	3.525	6.9109	3.482	4.714	2.267

Figure 4.12: Calculated imaging metrics for Hagness Breast using XETS antenna.

Figure 4.12 shows that the positioning error is good for the intended primary screening technique. Furthermore, it is verified that the values obtained for TCR and TMR are higher for ideal calibration than SVD, due to the tumor response is higher and the presence of clutter is smaller for ideal calibration. There are no significant differences between the values using the different methods, so it appears that the tumor is detected with both methods and the presence of a cluster, where it exists, is not significant to the point of masking the tumor.

From all the results obtained for Hagness Breast phantom, we can conclude that XETS and BAVA present similar imaging performance under the same conditions.

4.1.2 A1 Breast

After obtaining the measurements and data, processing and image reconstruction for the Hagness breast phantom, we proceeded in the same way for the A1 breast phantom.

Unlike the Hagness breast, for the A1 breast, the reflection coefficients were only obtained using the XETS antenna only, so this section does not present subsections.

Figure 4.13 shows the exterior of the A1 breast phantom in an xOz plane. The phantom .stl file is needed to obtain the breast mask for further image reconstruction, in order to obtain all information about the 3D breast model.
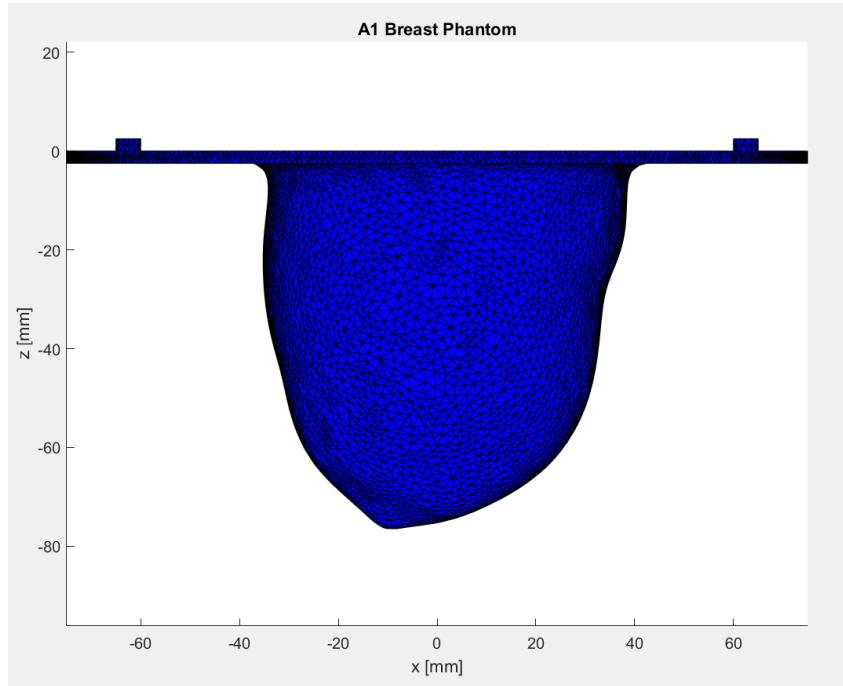
Figure 4.13: Representation of the A1 breast in the xOz plane.

Figure 4.14 represents the A1 breast mask in different planes and, analyzing the figure, it can be seen that the A1 breast is more elliptical than the Hagness breast, which can hinder the tumor detection process by the SVD calibration method and the sharp increase in the number of clutters.

In the lab setup, the A1 breast phantom is a 3-D-printed PLA shell ($\varepsilon_r \approx 2.75 - j0.03$ at 4 GHz), obtained from the University of Manitoba. [52]. The tumor was 3D-printed using conductive PLA filament, which presents $\varepsilon_r \approx 20 - j9$ at 4 GHz. [58] A1 breast phantom was filled with a Triton X-100 surfactant solution, with different percentage of each ingredient in order to mimic the dielectric properties of biological tissues.

In this experimental measurement, it was used the XETS antenna, which is a low-profile and light-weight antenna, with almost ideal transfer function, that is linear phase.

In this experimental analysis, 40 XETS antennas were used and to obtain the scattering parameters it was used an Arduino Uno and a motor to move the antenna around the breast according to the support.

The VNA was used in order to obtain the reflection coefficients so in reality a linear sweep of the antenna rotation angle between 0º and 360º was performed every 9º, which corresponds to 40 antenna positions. This procedure was repeated three times as there are three tumor positions.

In figure 4.15, it is possible to visualize a graphical representation of the 40 antennas distributed around the A1 breast and distances from the center of the breast by R mm.

As mentioned above, three tumor positions were used in these measurements. The first had the central coordinates in $(x_t, y_t, z_t) = (17, 5, -30)mm$, the second tumor corresponded to $(x_t, y_t, z_t) =$
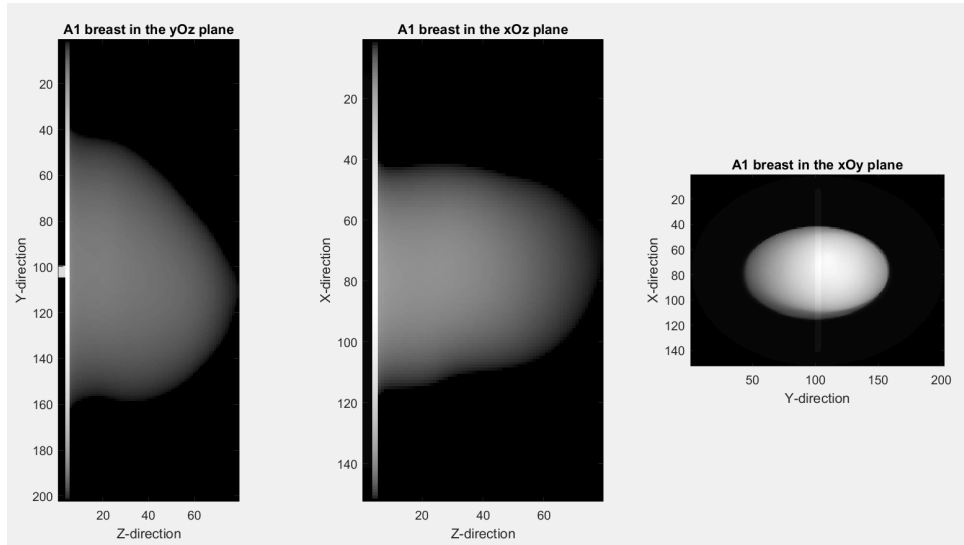
Figure 4.14: Representation of the A1 breast in different planes.

$(-20, -15, -30)mm$ and the third tumor was defined in $(x_t, y_t, z_t) = (-27, 12, -30)mm$.

One free space measurement was performed at the beginning for each antenna position, before insert the tumor container with the purpose to determine the distance introduce by the XETS antenna, a parameter that cause the translation of the position of the target's response.

After the insertion of the tumor inside the A1 breast phantom, the scattering parameters were obtained and the same procedure was done without the tumor.

Figure 4.16 shows the results obtained for a plane z = -45 mm considering the Tumor 1 for all 40 antenna's positions and using the two calibration methods mentioned above.

By analyzing figure 4.16, it is verified that using the ideal calibration method, which corresponds to figure 4.16(a), the tumor is detected, despite being deviated and the maximum intensity does not correspond to the analyzed plane, that is, z = -45 mm. Furthermore, Tumor 1 is also detected by the SVD calibration method with 4 neighbours, even though the breast is elliptical, as can be seen in figure 4.16(b).

The second step was the reconstruction of the image for Tumor 2 using the two calibration methods mentioned before and the results can be seen in figure 4.17.

By observing figure 4.17(a), it is possible to verify that Tumor 2 is also detected using the ideal calibration in the region for the exact position of the tumor, even if it is deviated from the central coordinates.

Subsequently, the image was reconstructed for Tumor 3 considering the 40 antennas around the breast, as shown in figure 4.18.

After viewing figure 4.18, there are certain aspects to report, namely that with the application of the ideal calibration method, as shown in figure 4.18(a), the tumor can be detected, although maximum intensity demonstrates that the tumor is not in that plane. The tumor is deviated from its position.
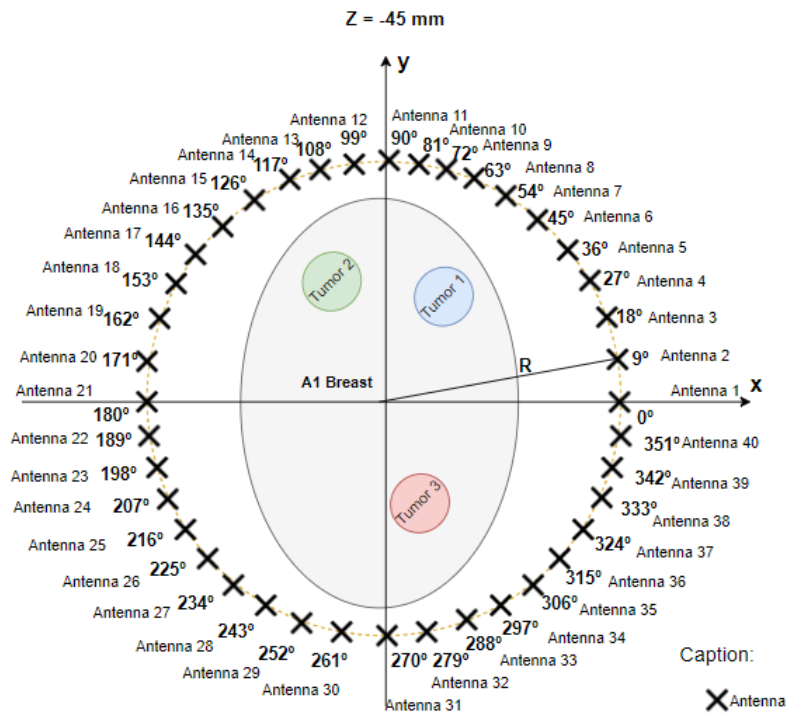
Figure 4.15: All 40 XETS antennas around the A1 breast phantom, where R is the distance between the center of the breast and the position of the antenna.

(a) Ideal Calibration

(b) SVD
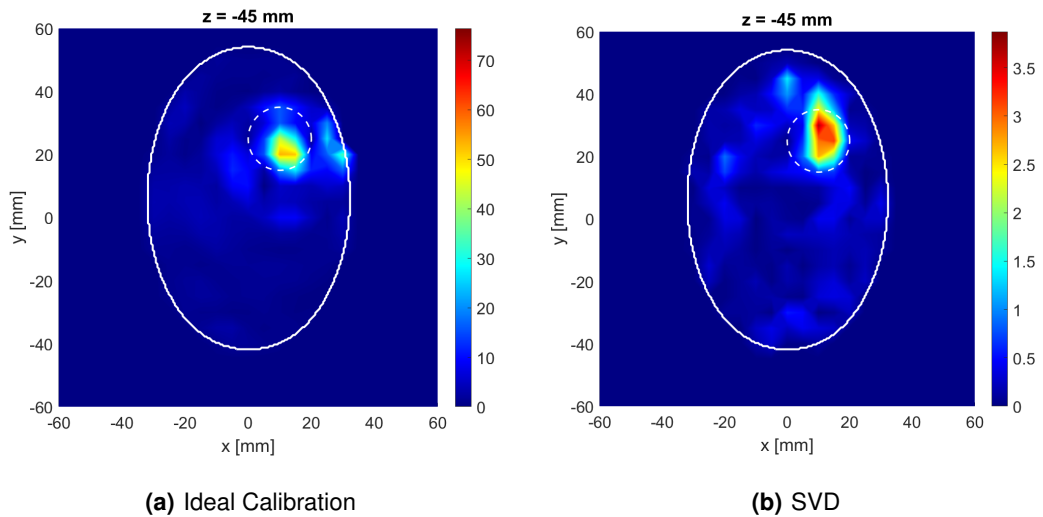
Figure 4.16: Imaging results for the plane z=-45mm considering the Tumor 1, all XETS antennas and using 4.16(a) the ideal calibration 4.16(b) the SVD. The white line translates the border of the breast with the air and the white dotted line the border between the tumor and the fat.

(a) Ideal Calibration   **(b)** SVD
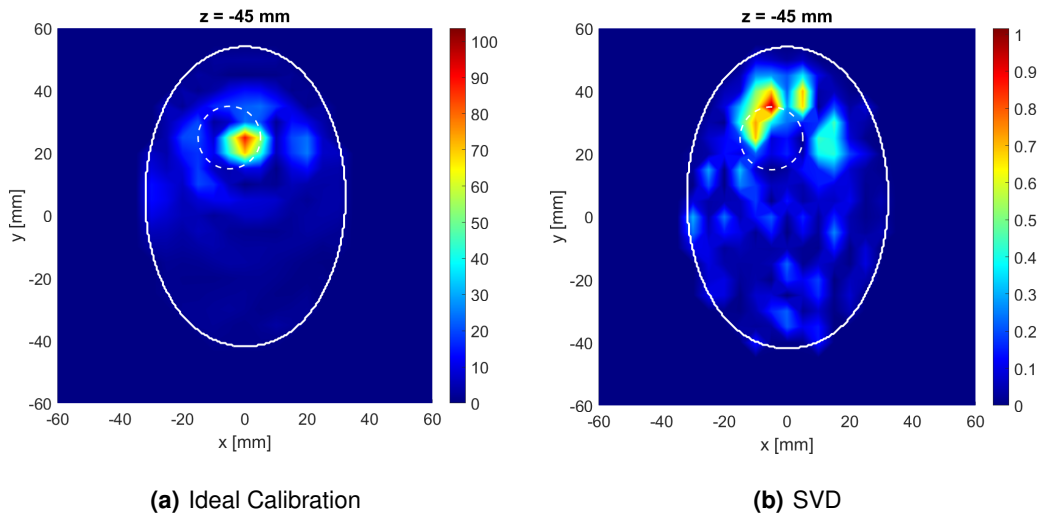
Figure 4.17: Imaging results for the plane z=-45mm considering the Tumor 2, all XETS antennas and using 4.17(a) the ideal calibration 4.17(b) the SVD. The white line translates the border of the breast with the air and the white dotted line the border between the tumor and the fat.

(a) Ideal Calibration   **(b)** SVD
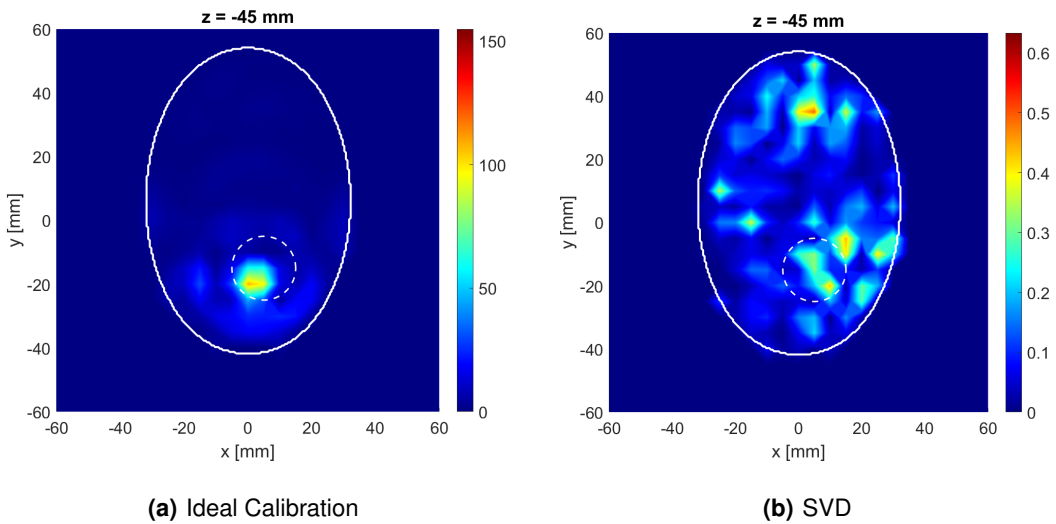
Figure 4.18: Imaging results for the plane z=-45mm considering the Tumor 3, all XETS antennas and using 4.18(a) the ideal calibration 4.18(b) the SVD. The white line translates the border of the breast with the air and the white dotted line the border between the tumor and the fat.

Referring to figure 4.18(b), it is concluded that the tumor is clearly not detected with SVD calibration method, mainly because the algorithm is affected by the non-symmetric distance between the antennas and the breast surface due to the breast being being elliptical and large.

It is important to point out that there are other factors that contribute to the fact that the Tumor 3 is not held by SVD namely it is known that the best known and most critical artifact of all is the reflection that occurs on the skin surface, which can be several orders of magnitude higher than the reflection that occurs on the tumor, and as Tumor 3 is close to the skin surface, it can be masked, since the tumor response can be suppressed.

4.1.3 A2 Breast

Therefore,the third experimentally measured breast phantom was the A2 and it was 3-D-Printed using PLA to mimic glandular breast tissue. [52]

Figure 4.19 shows the exterior of the phantom in an xOz plane and for that a .stl file of the phantom was needed, that contains the information about the 3D model of the A2 phantom.
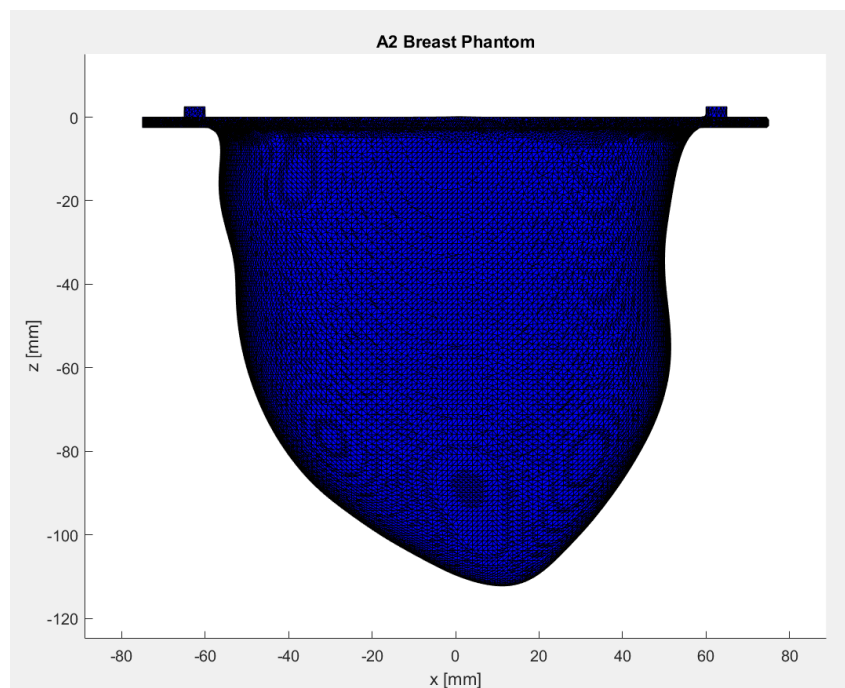
Figure 4.19: Representation of the A2 breast in the xOz plane.

The CST was initially used to center the breast by its base with the object to obtain the A2 breast mask, as shown in figure 4.20 and orient it according to the coordinates defined during the measurement in the laboratory.

During the experimental measurements, the A2 breast phantom, which is a 3-D-printed Polyactic acid
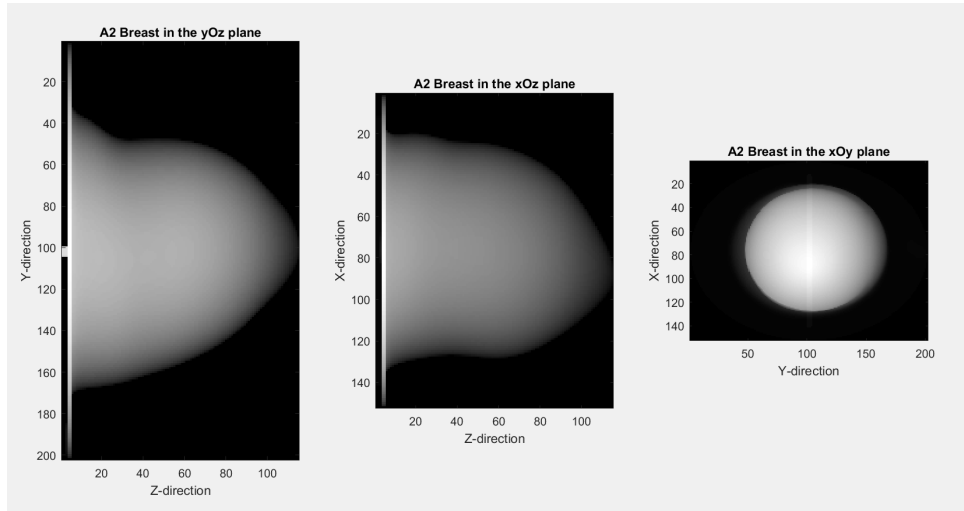
Figure 4.20: Representation of the A2 breast in different planes.

(PLA) shell ($\varepsilon_r \approx 2.75 - j0.03$ at 4 GHz), was filled with a Triton X-100 surfactant solution of permittivity of $\varepsilon_r \approx 4 - j0.17$ at 4 GHz that mimics the dielectric properties of biological tissues. The tumor is represented as a 10 mm $\times$20 mm ellipsoidal shape, and the tumor container is filled with a mixture of TX-100, distilled water and sodium chloride with the same dielectric properties of malignant tissues ($\varepsilon_r \approx 55 - j3$ at 4 GHz). The recipes of both liquids are reported in [59].

The breast phantom contains the tumor and three different tumor position were concerned for each of the two experimental analyzes that it is possible to see below, since this section about A2 breast phantom is divided into two sub-chapters: Circular Array Balanced Antipodal Vivaldi Antenna (CABAVA) antenna and Crossed Exponentially Tapered Slot (XETS) antenna, since they correspond to different experimental analyzes with different antennas.

4.1.3.A   CABAVA antenna

In this subsection, the antenna used to get the scattering parameters was the Circular Array Balanced Antipodal Vivaldi Antenna (CABAVA). In order to get more information about CABAVA antenna is possible to see this document [18], since the scope of this thesis is not the antenna characterization.

With the VNA, the reflection coefficients was obtained and it was necessary to manually move the antenna around the breast according to a support.

After that, a linear sweep of the CABAVA antenna rotation angle between 0º and 360º performed every 15º and considering the linear sweep of this experimental measures, it appears that it corresponds to 24 CABAVA antenna positions, in order to obtain the reflection coefficients for each of the three tumor positions. The antenna rotates clockwise around the A2 breast.

The figure 4.21 corresponds to a representation of the 24 XETS antennas around the breast phantom

47

distanced from the center of the breast, R mm.

The central coordinates of the positions of Tumor 1, Tumor 2 and Tumor 3 used in these measurements are, respectively, $(x_t, y_t, z_t) = (20, 25, -30)mm$, $(x_t, y_t, z_t) = (25, -5, -30)mm$ and $(x_t, y_t, z_t) = (-20, -20, -30)mm$.
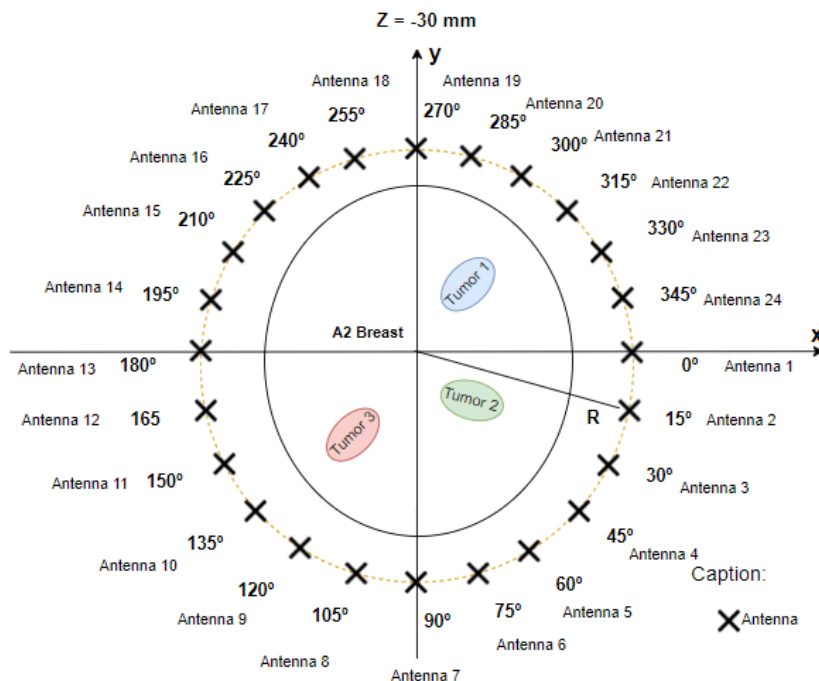

Figure 4.21: All 24 CABAVA antennas around the A2 breast phantom, where R is the distance between the center of the breast and the position of the antenna.

A free space measurement was performed for each antenna position, in order to reduce the internal reflections occurring inside the antenna structure and in order to obtain the image reconstructed, some important calibrate measurements were made and two different methods were used, since if the calibration was not performed, the image reconstruction algorithm did not process uniquely the target reflections,

In figure 4.22, it is possible to visualize the results obtained for a plane z= -30 mm considering Tumor 1 and for all 24 antennas using the ideal calibration and SVD, respectively.

By analyzing the figure 4.22, it can be seen that when the measurements obtained with the tumor are subtracted from those without the tumor, in order to obtain the tumor response and with the application of the reconstruction algorithm, Tumor 1 is perfectly detected in the plane z = -30 mm. Regarding the SVD calibration method with the help of 2 neighbors, it is possible to verify that the tumor is detected, but there is an accentuated presence of clutters, that can be related with the fact of the A2 is a dense breast.

The figure 4.23 shows the reconstruction of the image for Tumor 2 using the two methods mentioned

(a) Ideal Calibration

(b) SVD
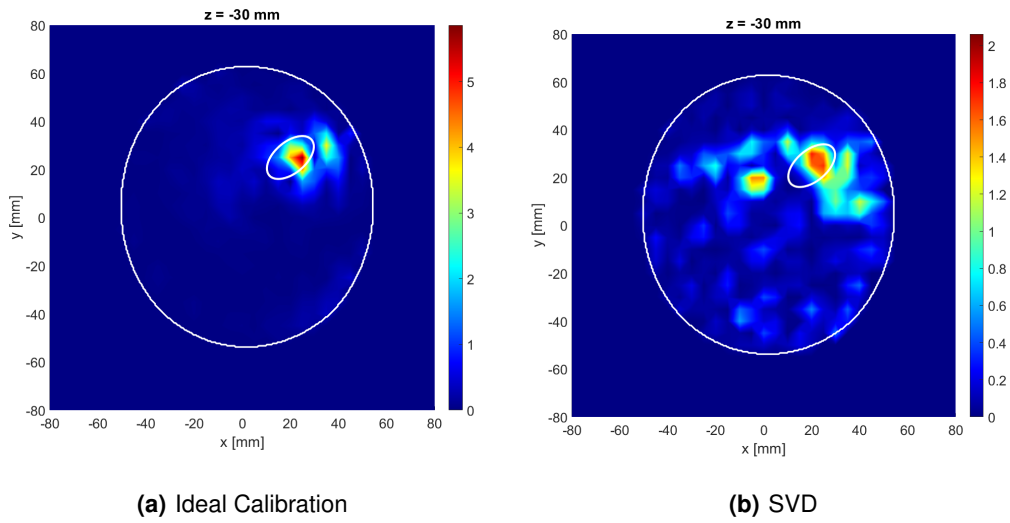
Figure 4.22: Imaging results for the plane z=-30mm considering the Tumor 1, all CABAVA antennas and using 4.22(a) the ideal calibration 4.22(b) the SVD. The white lines translate the border of the breast with the air and the border between the tumor and the fat.

above.

(a) Ideal Calibration

(b) SVD
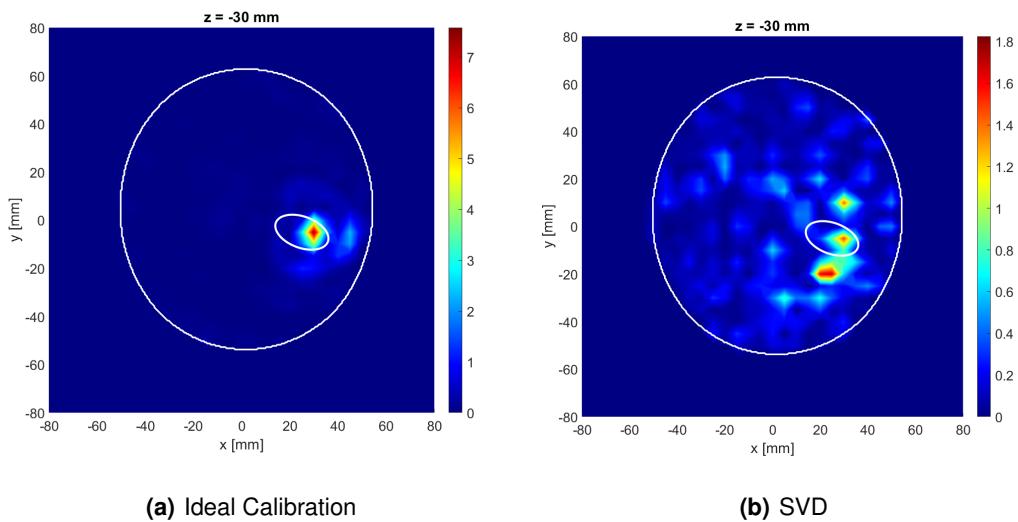
Figure 4.23: Imaging results for the plane z=-30mm considering the Tumor 2, all CABAVA antennas and using 4.23(a) the ideal calibration 4.23(b) the SVD. The white lines translate the border of the breast with the air and the border between the tumor and the fat.

By observing figure 4.23(a) verifies that Tumor 2 is detected using the ideal calibration in the with some deviation from the exact position of the tumor. However, the SVD calibration method with 2 neighbours shows a cluster under the region where Tumor 2 should be, however, given the presence of several

clusters, it ends up masking the tumor response, as it can be seen figure 4.23(b).

Figure 4.24(a) and figure 4.24(b) represent Tumor 2 response using an image reconstruction algorithm using optimal and SVD calibration methods, respectively. Although Tumor 3 is detected with ideal calibration method, it is not detected with SVD, for the same reasons as Tumor 2.

(a) Ideal Calibration   **(b)** SVD
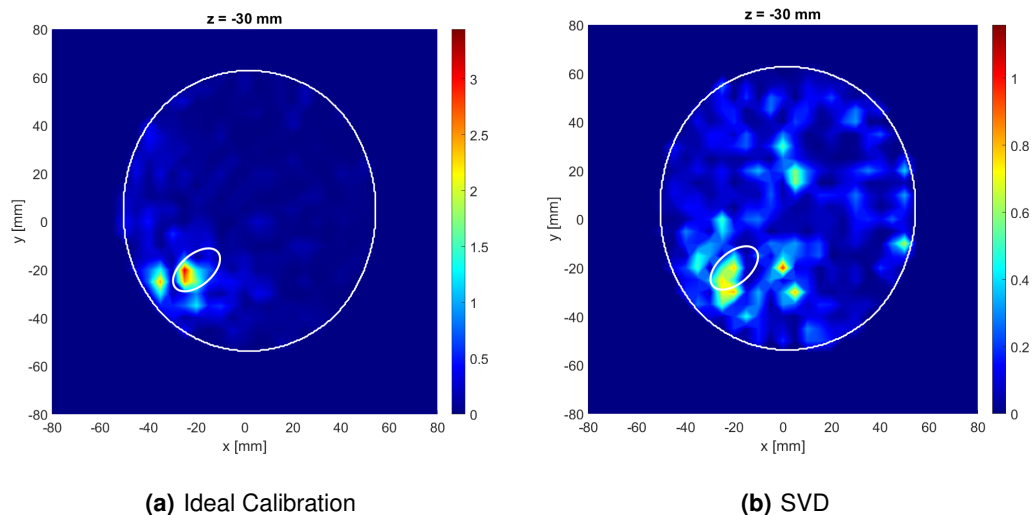
Figure 4.24: Imaging results for the plane z=-30mm considering the Tumor 3, all CABAVA antennas and using 4.24(a) the ideal calibration 4.24(b) the SVD. The white lines translate the border of the breast with the air and the border between the tumor and the fat.

4.1.3.B XETS antenna

In the second experimental measurements with the A2 breast phantom, the XETS antenna was used. In section 4.1.1.B some aspects were discussed, that is, characteristics of the XETS antenna.

A linear sweep of the XETS antenna rotation angle between 0º and 360º performed every 15º, which corresponds to 24 XETS antenna positions, in order to obtain the reflection coefficients.

Figure 4.25 shows a representation of the 24 XETS antennas around the A2 breast phantom distanced from the center of the breast (R).

The antenna 1 corresponds to 180º angle, since XETS was opposite at CABAVA antenna during this experimental measurements.

Figure 4.26 represents the results of the reconstructed A2 breast image for Tumor 1 and it is possible to state that Tumor 1 is detected either by using the ideal calibration method as well as by the SVD method.

The results of the reconstructed A2 breast image for Tumor 2 and 3 are present at Figure 4.27, 4.28, respectively and it is possible to conclude also that tumors 2 and 3 are detected either by using the ideal
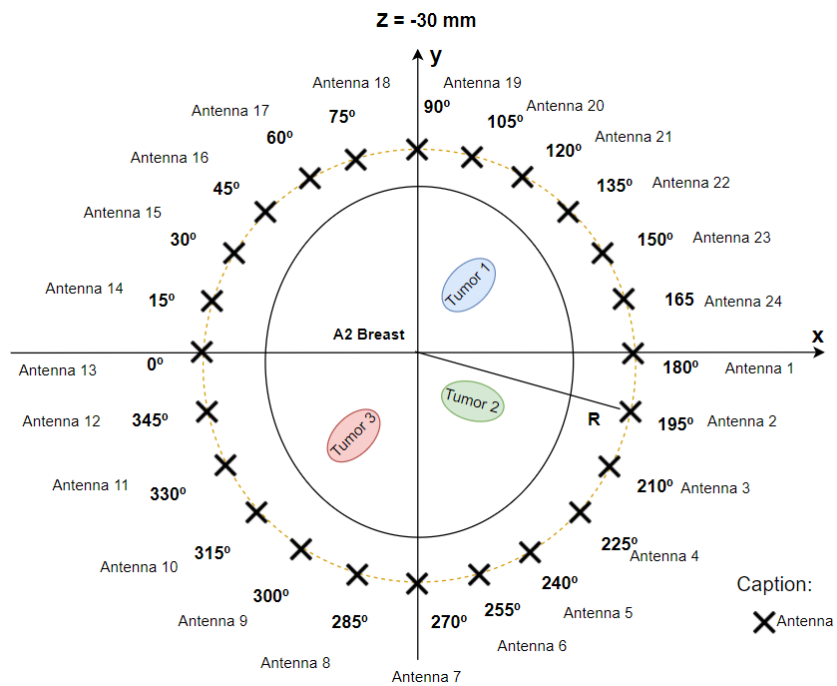
Figure 4.25: All 24 XETS antennas around the A2 breast phantom, where R is the distance between the center of the breast and the position of the antenna.

(a) Ideal Calibration

(b) SVD
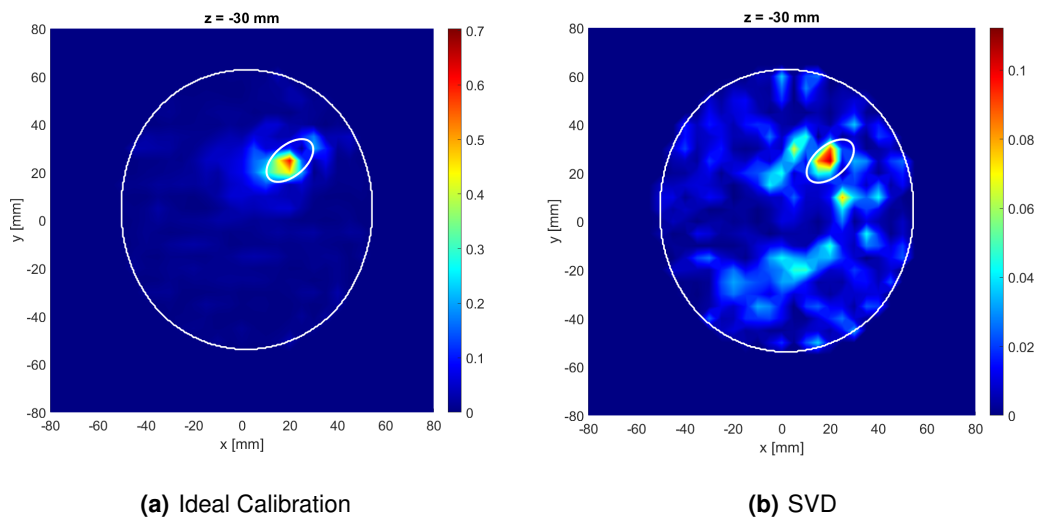
Figure 4.26: Imaging results for the plane z=-30mm considering the Tumor 1, all XETS antennas and using 4.26(a) the ideal calibration 4.26(b) the SVD. The white lines translate the border of the breast with the air and the border between the tumor and the fat.

calibration method as well as by the SVD method.

(a) Ideal Calibration **(b)** SVD
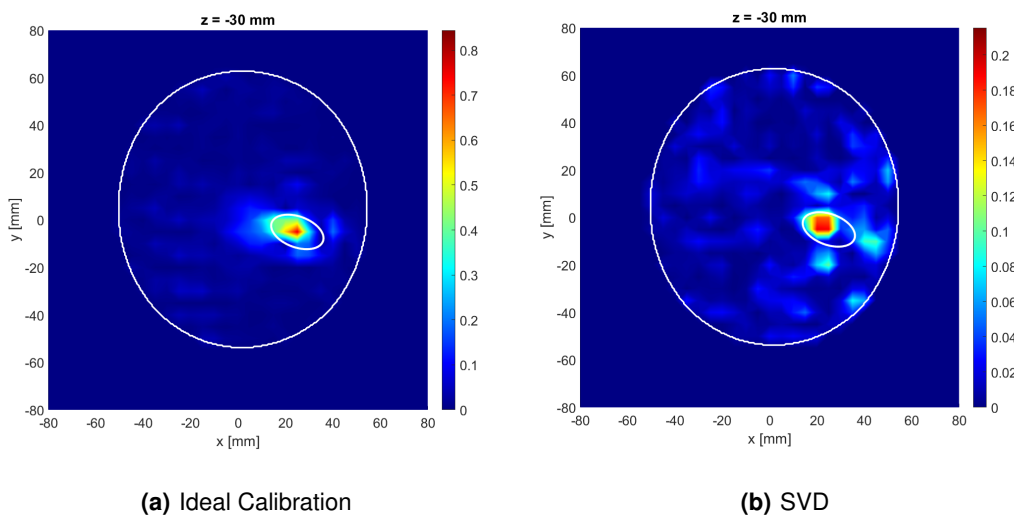
Figure 4.27: Imaging results for the plane z=-30mm considering the Tumor 2, all XETS antennas and using 4.27(a) the ideal calibration 4.27(b) the SVD. The white lines translate the border of the breast with the air and the border between the tumor and the fat.

(a) Ideal Calibration **(b)** SVD
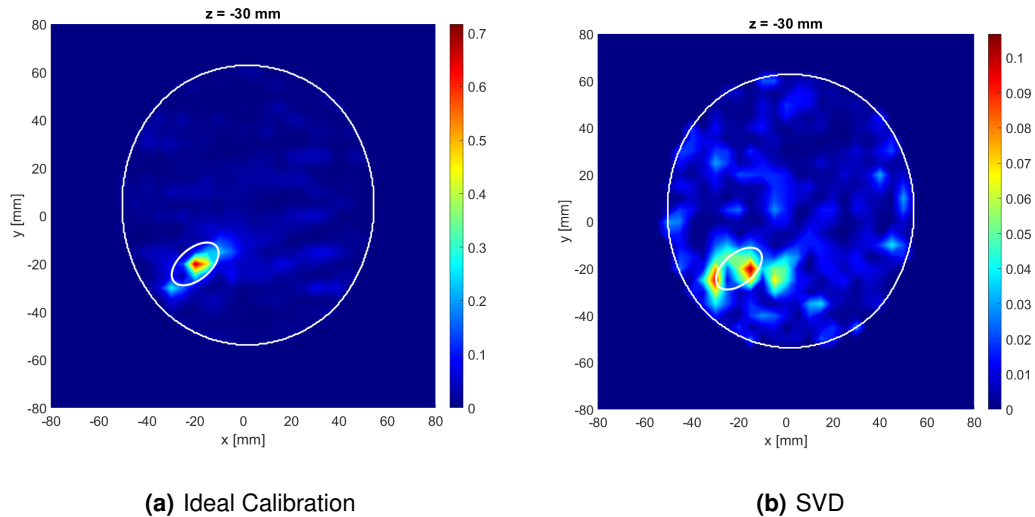
Figure 4.28: Imaging results for the plane z=-30mm considering the Tumor 3, all XETS antennas and using 4.28(a) the ideal calibration 4.28(b) the SVD. The white lines translate the border of the breast with the air and the border between the tumor and the fat.

4.1.4 A3 Breast

In this section, the study of the images obtained by the image reconstruction algorithm for the A3 breast, from the signals measured experimentally with the XETS antenna and with the VNA, is discussed.

Figure 4.29 represents the outside of the breast in the xOz plane and its obtained by the .stl breast file.

As with the previous breasts phantoms, the A3 breast is a 3-D-printed PLA shell ($\varepsilon_r \approx 2.75 - j0.03$ at 4 GHz).

Before the experimental measurements, the A3 breast was filled with a Triton X-100 surfactant solution of permittivity of $\varepsilon_r \approx 4 - j0.17$ at 4 GHz that mimics the dielectric properties of biological tissues. Regarding the tumor, its container was filled with a mixture of TX-100, distilled water and sodium chloride with the same dielectric properties of malignant tissues ($\varepsilon_r \approx 55 - j3$ at 4 GHz). The recipes of both liquids are reported in [59].
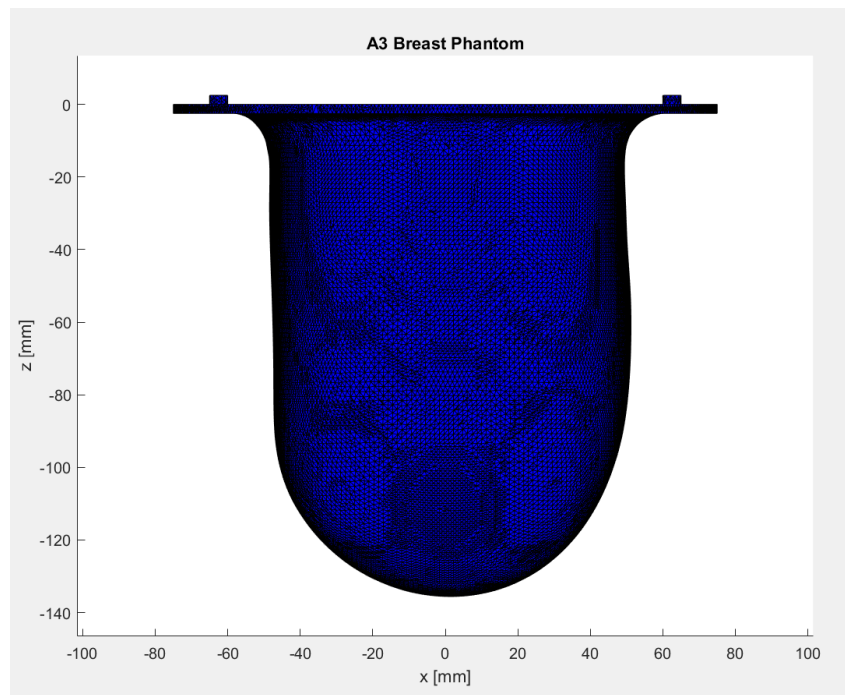
Figure 4.29: Representation of the A3 breast in the xOz plane.

Figure 4.30 shows the A3 breast mask in different planes. And from figures 4.29 and 4.30 it can be seen that the A3 breast is very dense, elliptical and large, which can hinder the process of image reconstruction by using the SVD method.

In order to obtain the measurements of the signals, the XETS antenna position around the A3 breast was scanned, starting at 0º and ending at 360º, with a variation of 15º, which corresponds to 24 possible antenna positions, as it is possible see in figure 4.31.
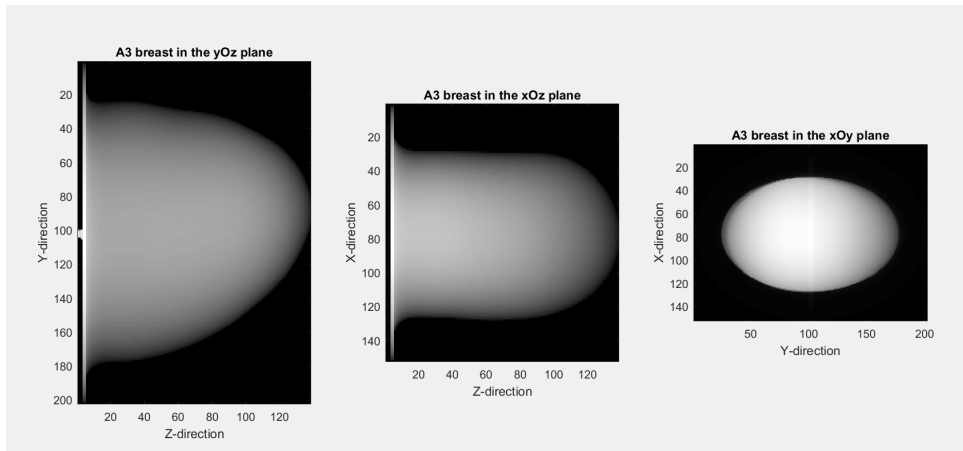
Figure 4.30: Representation of the A3 breast in different planes.
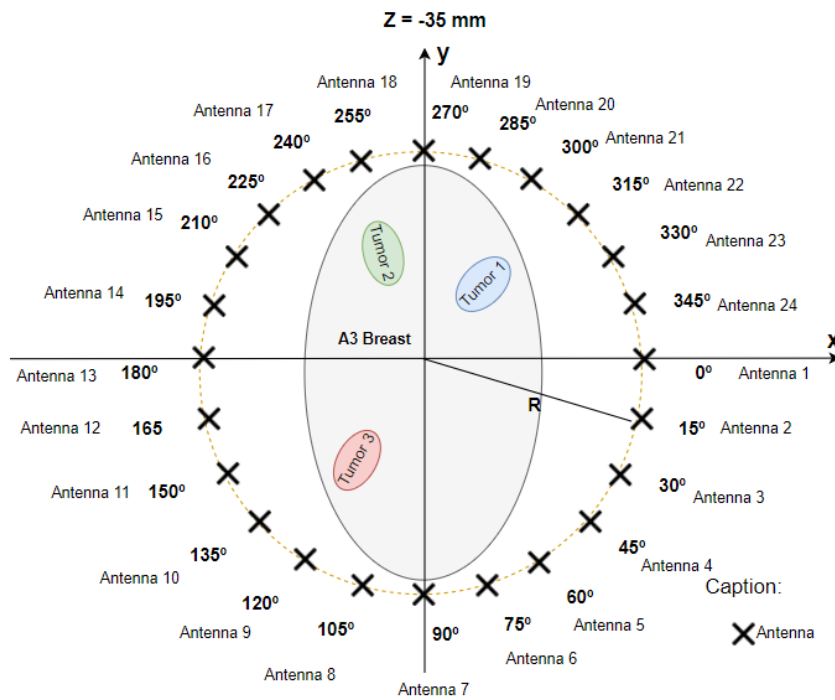

Figure 4.31: All 24 XETS antennas around the A3 breast phantom, where R is the distance between the center of the breast and the position of the antenna.

Then, using the image reconstruction algorithm, different images were obtained for the three positions of the tumor, using the ideal calibration method and the SVD calibration method.

The imaging results for the plane z = -35 mm based on experimental data obtained considering the Tumor 1 are shown in figure 4.32. The coordinates of the Tumor 1 central position are $(x_t, y_t, z_t) = (20, 20, -30)mm$.

(a) Ideal Calibration   **(b)** SVD
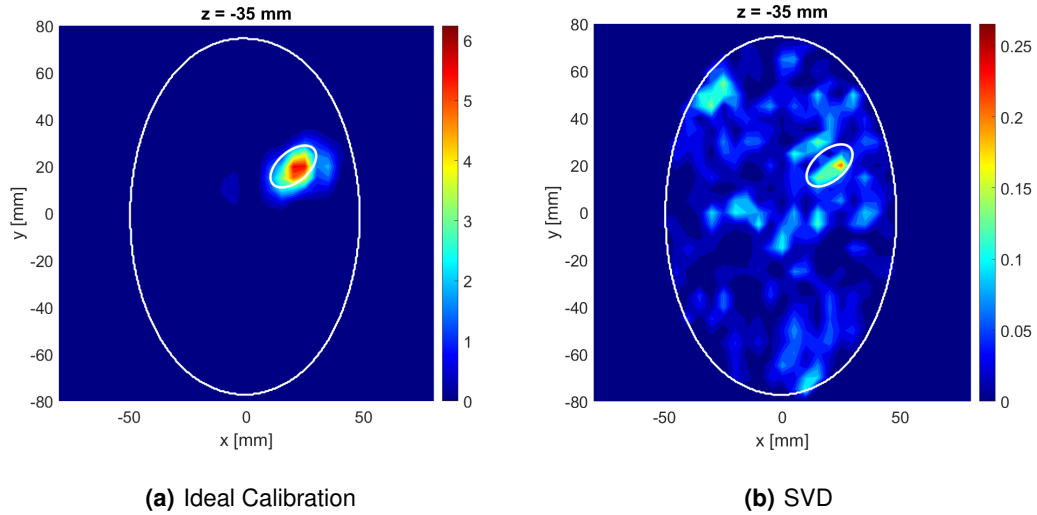
Figure 4.32: Imaging results for the plane z=-35mm considering the Tumor 1, all XETS antennas and using 4.32(a) the ideal calibration 4.32(b) the SVD. The white lines translate the border of the breast with the air and the border between the tumor and the fat.

After viewing figure 4.32, it is possible to conclude that in the absence of the calibration, the energy does not focus and, therefore, the tumor is not detected. Furthermore, the tumor can be detected using Ideal Calibration and doesn't present any clutter. In addition, with the figure 4.32(b), we can conclude that the tumor can be detected with SVD calibration, but has much clutter spread in the image, making tumor detection difficult.

Regarding Tumor 2, which position is $(x_t, y_t, z_t) = (-5, 27, -30)mm$, it is possible to see figure 4.33 and conclude that although the tumor is detectable using the ideal calibration method, which is totally normal, the tumor is not detected with the SVD calibration method, mainly due to the fact of the algorithm be affected by the non-symmetric distance between the antennas and the breast surface due to the breast being elliptical and also large.

Finally, regarding the analysis of the results of the images obtained through the reflection coefficients for Tumor 3, whose position is $(x_t, y_t, z_t) = (-25, -20, -30)mm$, we can conclude that the tumor can be detected with Ideal Calibration and the position correspond the real position, without any deviation. Furthermore, the Tumor 3 can be also detected with the SVD algorithm, as it can be seen in figure 4.33(b).

(a) Ideal Calibration   **(b)** SVD
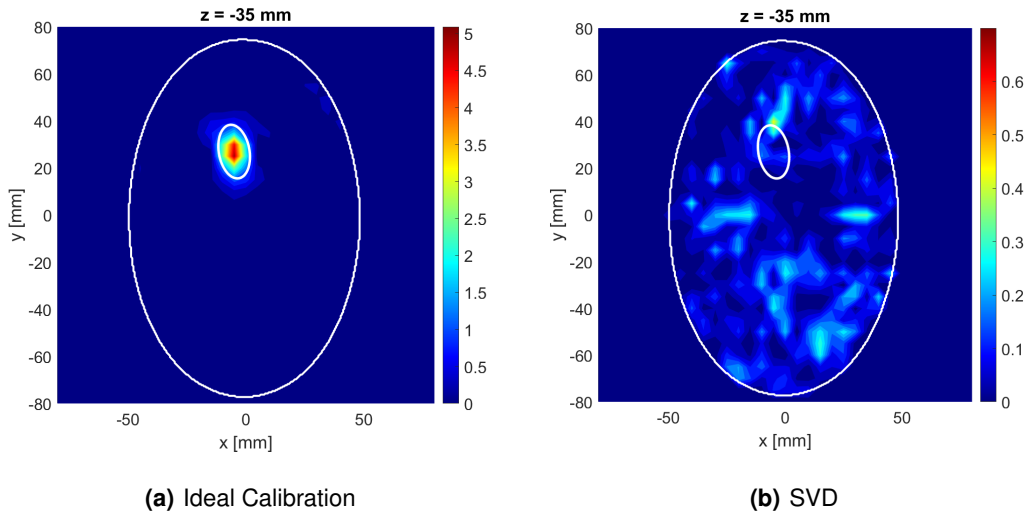
Figure 4.33: Imaging results for the plane z=-35mm considering the Tumor 2, all XETS antennas and using 4.33(a) the ideal calibration 4.33(b) the SVD. The white lines translate the border of the breast with the air and the border between the tumor and the fat.


(a) Ideal Calibration   **(b)** SVD
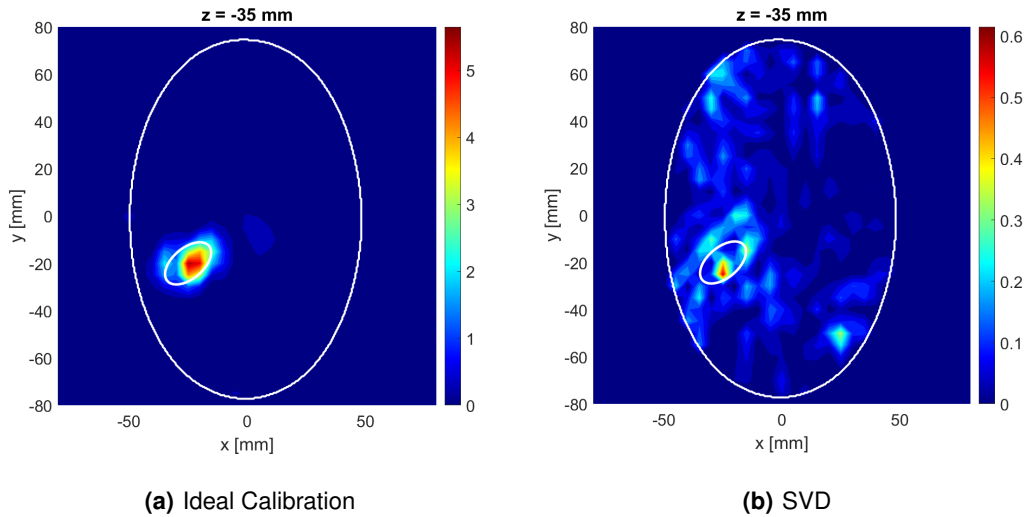
Figure 4.34: Imaging results for the plane z=-35mm considering the Tumor 3, all XETS antennas and using 4.34(a) the ideal calibration 4.34(b) the SVD. The white lines translate the border of the breast with the air and the border between the tumor and the fat.

The metrics calculated in the A3 Breast using XETS antenna, which was discussed before, are summarized in Figure 4.35.

Positions (x_t, y_t, z_t)		Tumor 1		Tumor 2		Tumor 3	
		Ideal Cal.	SVD	Ideal Cal.	SVD	Ideal Cal.	SVD
	Actual	(20, 20, –30)		(–5, 27, –30)		(-25, –20, -30)	
	Detected	(24,21,-35)	(29,21,-43)	(-5,25,-32)	-	(-23,-19,-35)	(-28,-22,-42)
	PE	6.481	16.232	9.031	-	14.771	21.959
	TCR [dB]	5.177	3.685	6.513	-	5.537	4.2393
	TMR [dB]	7.502	6.318	9.159	-	8.258	6.902

Figure 4.35: Calculated imaging metrics for A3 Breast using XETS antenna.

By analyzing Figure 4.35, it is verified that the values obtained for TCR and TMR are higher for ideal calibration than SVD, given that the tumor response is higher and the presence of clutter is smaller. Furthermore, the positioning error is good for almost cases.

4.1.5 A12 Breast

In figure 4.36, it is possible to visualize the representation of the A12 breast phantom, a 3-D-printed Polyactic acid (PLA) shell ($\varepsilon_r \approx 2.75 - j0.03$ at 4 GHz), in the xOz plane. The base of the breast is at z=0 mm and the antenna used to measure this breast is XETS.

The A12 beast phantom was provided by the Manitoba University and as with the other breasts already discussed, the A12 breast phantom was also filled with a Triton X-100 surfactant solution of permittivity of near of $\varepsilon_r \approx 4 - j0.17$ at 4 GHz, that emulates the breast fat tissues.

The tumor used in the measurements was 3D-printed conductive PLA filament, which presents $\varepsilon_r \approx 20 - j9$ at 4 GHz. [58]

Furthermore, in figure 4.37, it is possible to visualize the A12 breast in different planes, which were obtained through the mask created from the .stl file.

The schematic representation of the 40 antennas around the breast with different positions of the tumor can be seen in figure 4.38. The measurements of the signals were obtained with the help of an

57
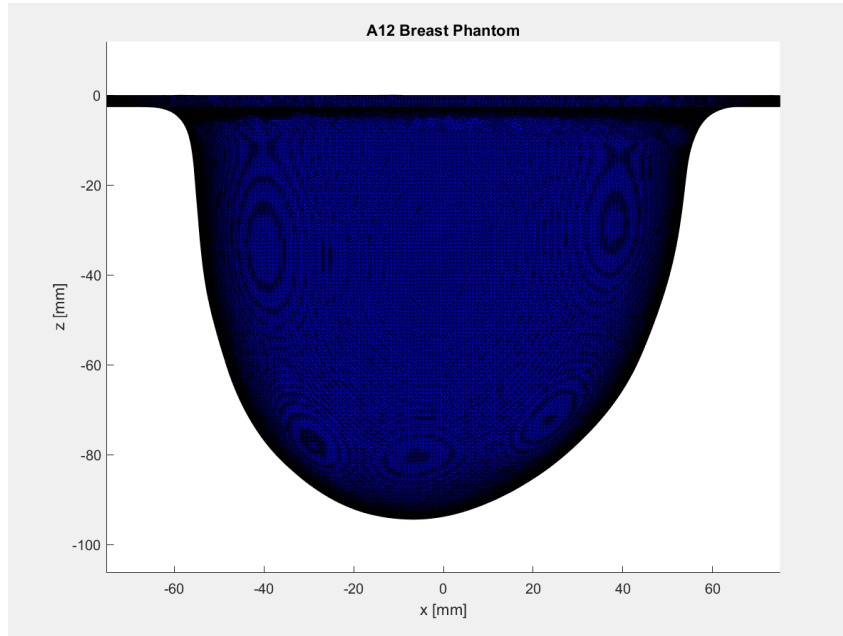
Figure 4.36: Representation of the A12 breast in the xOz plane.

Arduino Uno and motor, where the Arduino Uno controlled the Direct Current (DC) motor, in order to move the antenna around the breast. The procedure was repeated three times, since exists three tumor positions.

First, different resulting images were obtained applying the image reconstruction algorithm based on experimental data obtained for Tumor 1 according to the plane Z = -45 mm for breast A12, as it can be seen in figure 4.39. The coordinates of the central position of Tumor 1 are as follows, $(x_t, y_t, z_t) = (15, 15, -43.5)mm$

When the ideal calibration method is used, the Tumor 1 is correctly detected with all 40 XETS antennas, despite finding slightly deviated. In Figure 4.39(b), it is also possible to conclude that Tumor 1 is detected if the applied method is the SVD. However, it appears that there is the presence of clutter around the Tumor 1 area, which can mask it and decrease the tumor's response.

The second step was the reconstruction of the image for Tumor 2 using the two methods mentioned above and the results can be seen in Figure 4.40. The coordinates of the central position of Tumor 2 are $(x_t, y_t, z_t) = (-20, 5, -43.5)mm$. Figure 4.40(b) shows relevant artifacts in the resulting image with refraction outside the region of the target when we use the SVD method to reconstruct the image. Despite detecting the tumor, an artifact of equally high intensity appears near the tumor area.

Finally, in figure 4.41 it is possible to visualize the imaging results for the reconstructed A12 breast and considering the tumor 3, which coordinates are $(x_t, y_t, z_t) = (5, -20, -43.5)mm$

At it is possible to verify at figure 4.41(a), the tumor 3 can be clearly detected using Ideal Calibration,with a small presence of clutter at breast skin. Through the application of the SVD method with 4
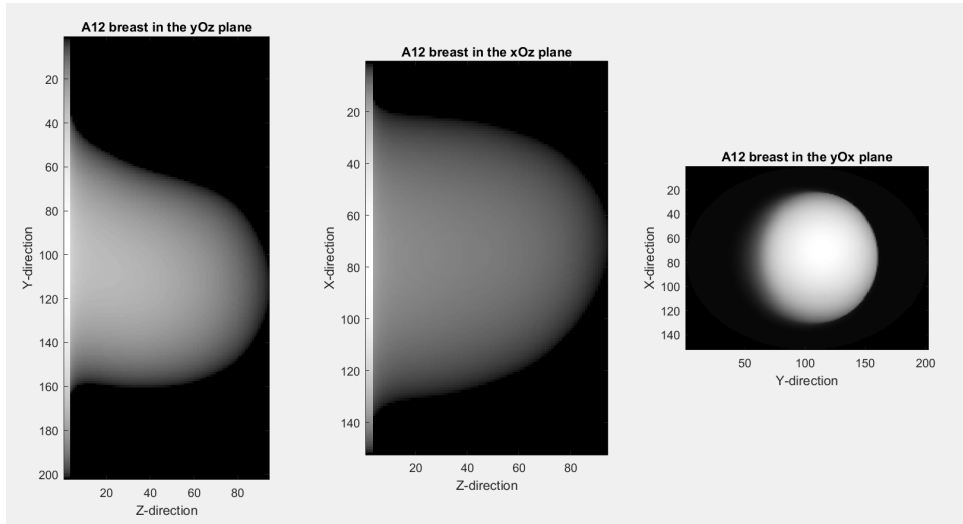
Figure 4.37: Representation of the A12 breast in different planes.

neighbours it is found that despite the detection of the tumor 3 being achieved near the real position of the tumor, there is some clutter surrounding the area, which can mask the tumor and decrease the tumor's response.
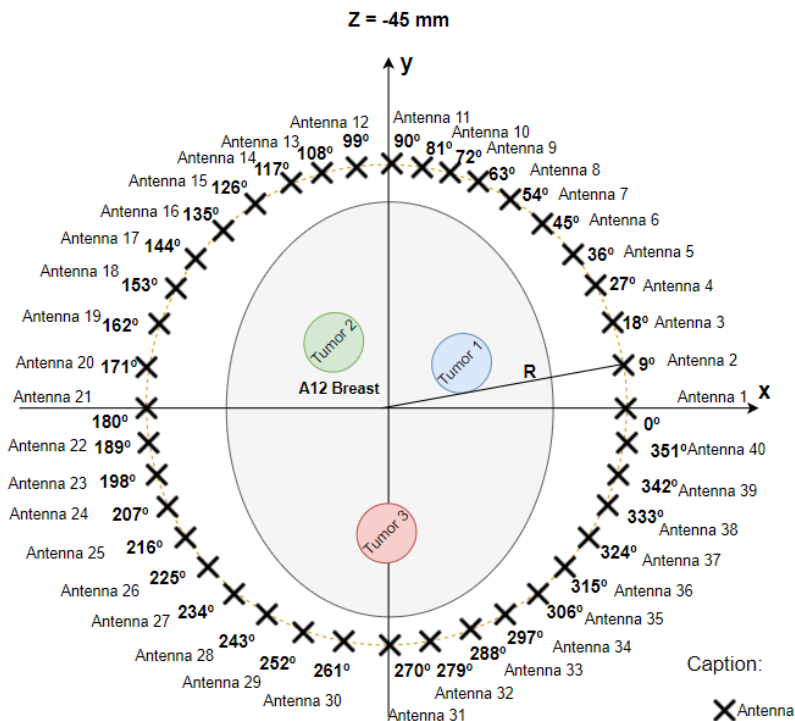
Figure 4.38: All 40 antennas around the A12 breast phantom, where R is the distance between the center of the breast and the position of the antenna.

59

(a) Ideal Calibration   **(b)** SVD
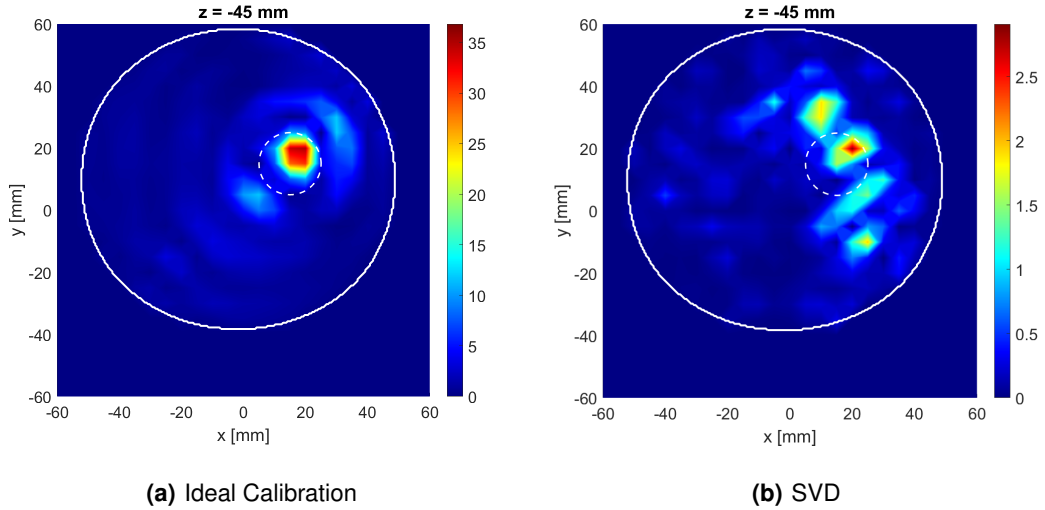
Figure 4.39: Imaging results for the plane z=-45mm considering the Tumor 1, all antennas and using 4.39(a) the ideal calibration 4.39(b) the SVD. The white line translates the border of the breast with the air and the white dotted line the border between the tumor and the fat.

(a) Ideal Calibration   **(b)** SVD

Figure 4.40: Imaging results for the plane z=-45mm considering the Tumor 2, all antennas and using 4.40(a) the ideal calibration 4.40(b) the SVD. The white line translates the border of the breast with the air and the white dotted line the border between the tumor and the fat.

(a) Ideal Calibration   **(b)** SVD
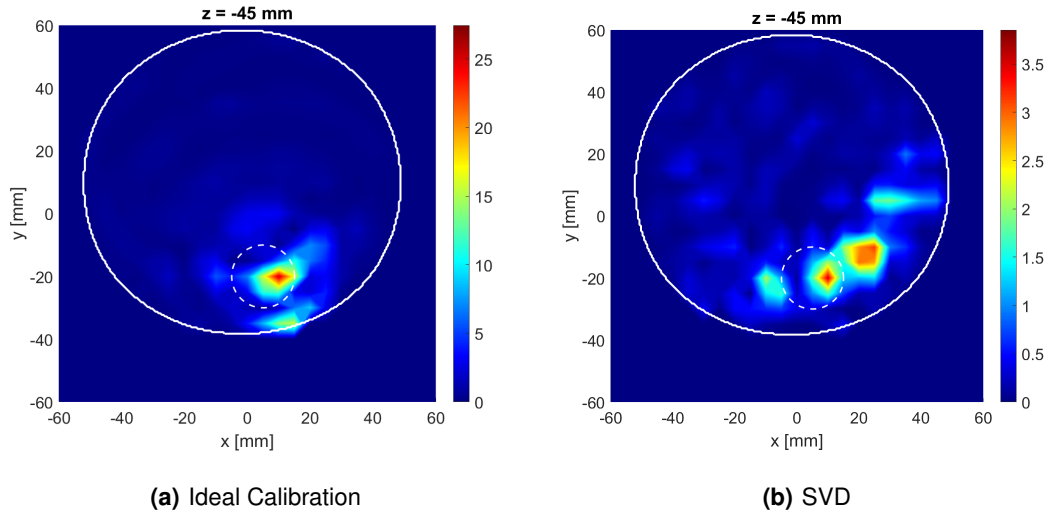
Figure 4.41: Imaging results for the plane z=-45mm considering the Tumor 3, all antennas and using 4.41(a) the ideal calibration 4.41(b) the SVD. The white line translates the border of the breast with the air and the white dotted line the border between the tumor and the fat.

4.1.6 A14 Breast

In this section, the study of the images obtained by the image reconstruction algorithm for the A14 breast phantom from the signals measured experimentally with the XETS antenna and with the VNA is discussed.

Figures 4.42 and 4.43 represents the outside of the breast in the xOz plane, which its obtained by the .stl breast file and the A14 breast mask in three different planes, respectively.

The breast and tumor phantom are fabricated from materials that are widely available and is easy to make.

A14 breast phantom is a 3-D-printed PLA shell ($\varepsilon_r \approx 2.75 - j0.03$ at 4 GHz) filled with a liquid of permittivity of of $\varepsilon_r \approx 4 - j0.17$ at 4 GHz, that emulates the breast fat tissues. The tumor is represented as a 10 mm $\times$20 mm ellipsoidal shape, filled with a liquid with the same dielectric properties of malignant tissues ($\varepsilon_r \approx 55 - j3$ at 4 GHz). The recipes of both liquids are reported in [59].

In this experimental measurement, it was used a vector network analyzer and 24 XETS antennas to obtain the scattering parameters so in reality a linear sweep of the antenna rotation angle between 0º and 360º was performed every 15º.
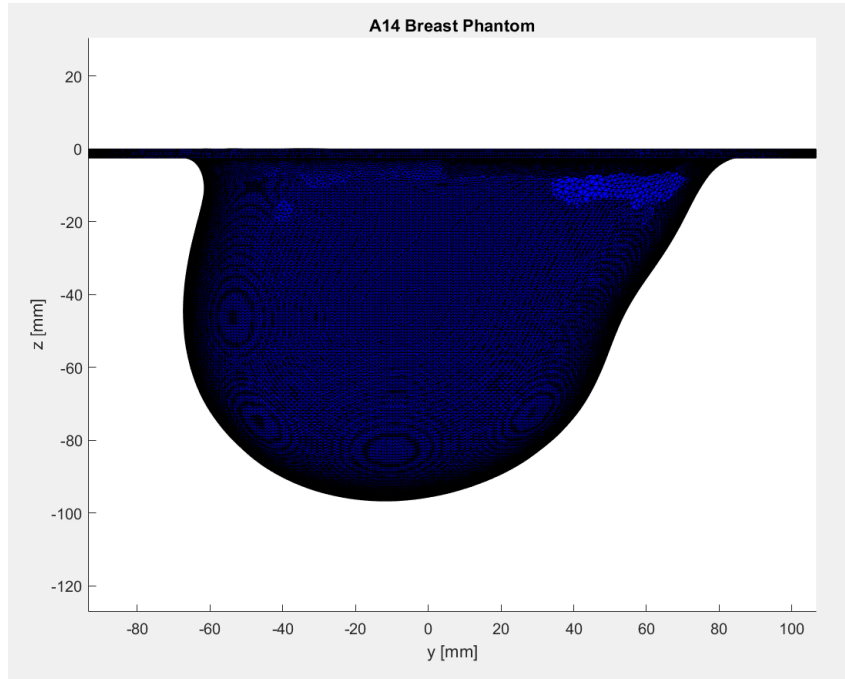
Figure 4.42: Representation of the A14 breast in the yOz plane.

The schematic representation of the XETS antennas around the breast with the 3 positions of the tumor can be seen in figure 4.44.
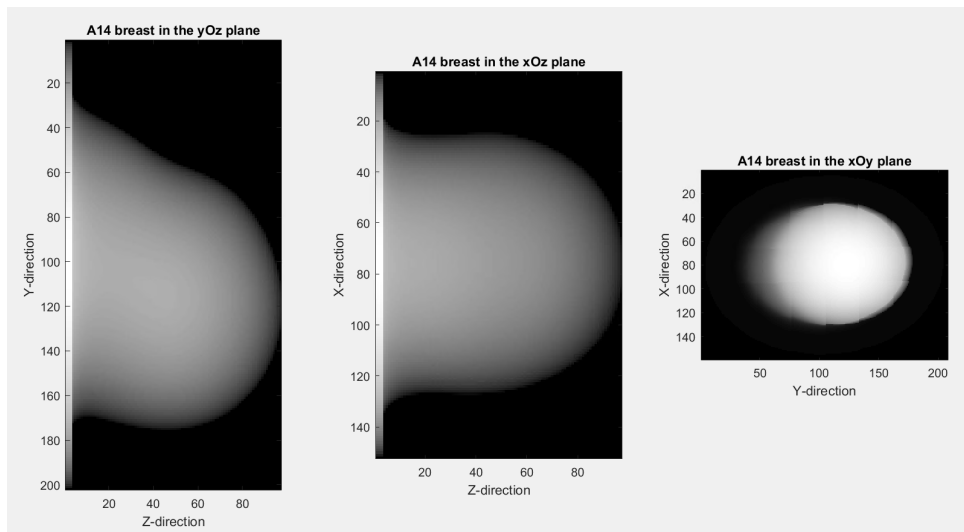
Figure 4.43: Representation of the A14 breast in different planes.

After executing the migration algorithm for breast reconstruction, the following figure was obtained considering all antennas to Tumor 1 4.45. The results that are going to be presented was obtained using the ideal calibration and SVD method. A PEC target, that is Tumor 1, was embedded in the phantom at coordinates $(x_t, y_t, z_t) = (10, 20, -30)mm$
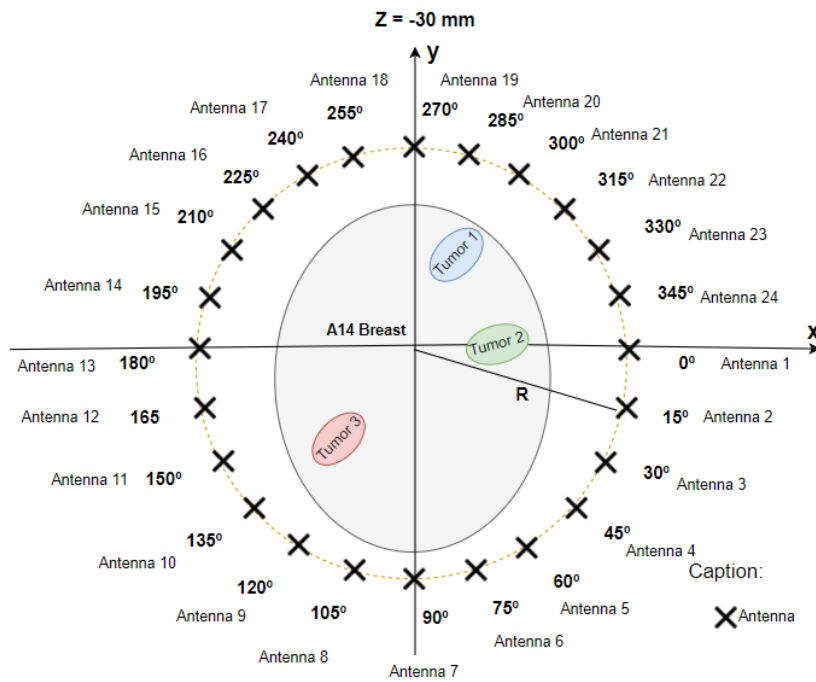
Figure 4.44: All 24 antennas around the A14 breast phantom, where R is the distance between the center of the breast and the position of the antenna.
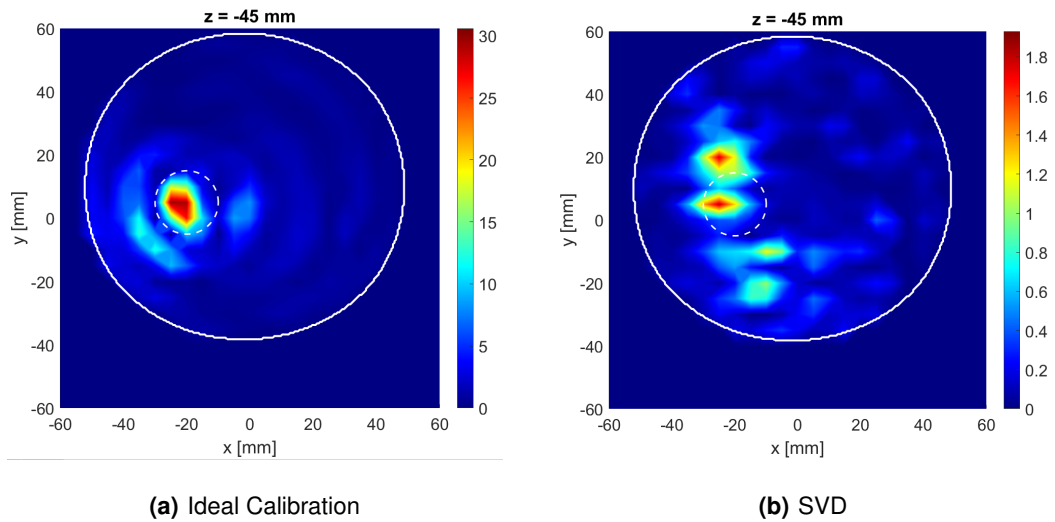

(a) Ideal Calibration

(b) SVD
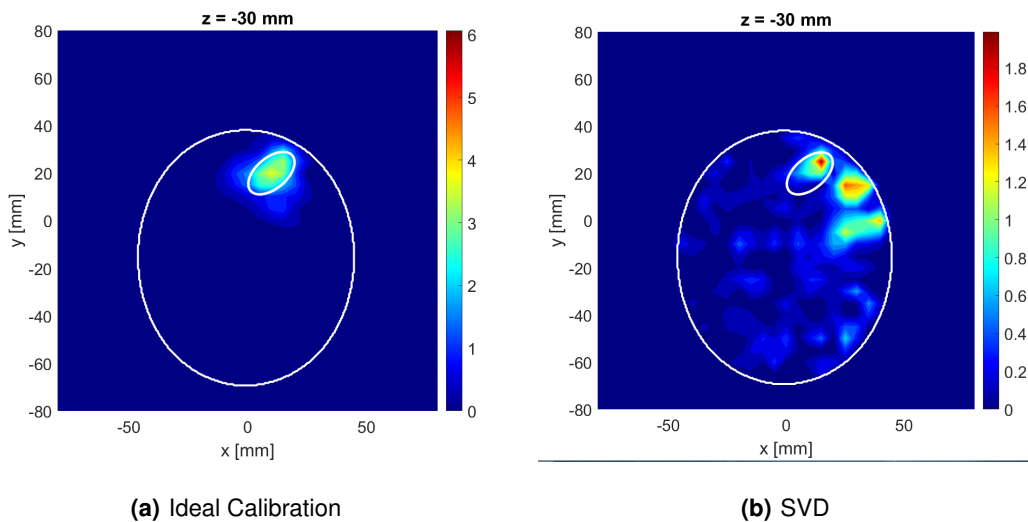
Figure 4.45: Imaging results for the plane z=-30mm considering the Tumor 1, all XETS antennas and using 4.45(a) the ideal calibration 4.45(b) the SVD. The white lines translate the border of the breast with the air and the border between the tumor and the fat.

The results from figure 4.45, indicates that is possible to detect the tumor, if the calibration is performed. Even with SVD it is possible to detect tumor 1, despite the presence of clusters. The exterior white contour defines the limits of the breast phantom, that is the breast skin, whereas the elliptical white contour marks the tumor.

If the calibration is not performed, the algorithm does not process uniquely the target reflections, since there are two issues (fat and skin) which compromises the effectiveness of the imaging algorithm.

The subtraction of a calibration measurement mitigates the negative effects previously described, in order to improve algorithm performance and have better imaging results.

Figure 4.46 represents a similar scenario as the previous one, where the only difference is the tumor response will be different, since the tumor will be 2, instead Tumor 1. The central coordinates of the positions of Tumor 2 used in these measurements are $(x_t, y_t, z_t) = (20, -15, -30)mm$.

(a) Ideal Calibration   **(b)** SVD
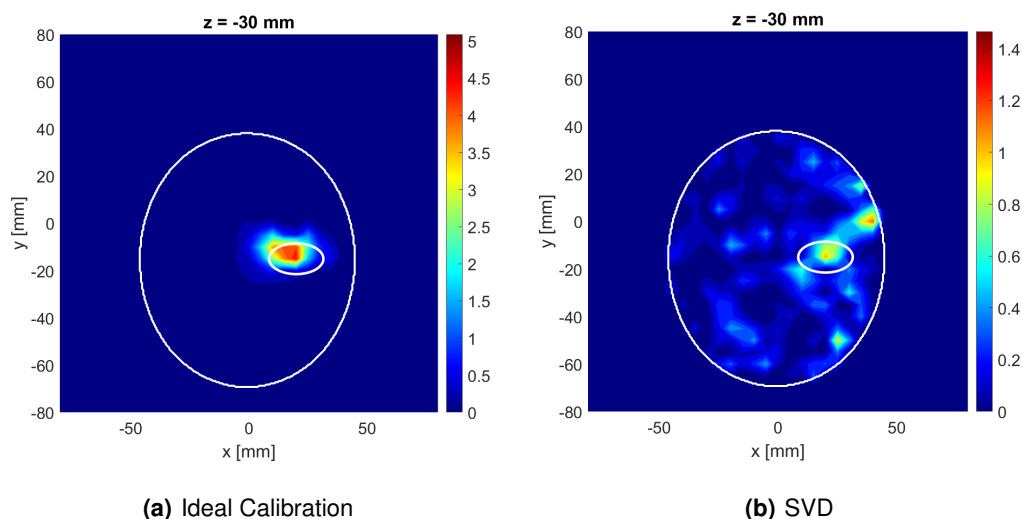
Figure 4.46: Imaging results for the plane z=-30mm considering the Tumor 2, all XETS antennas and using 4.46(a) the ideal calibration 4.46(b) the SVD. The white lines translate the border of the breast with the air and the border between the tumor and the fat.

The left image from figure 4.46, that is, figure 4.46(a) shows a clear detection of the Tumor 2. In relation to the figure on the left, the cluster present with greater intensity is found over the region where the response of tumor 2 should appear, but it is evident that there is a deterioration of the results, since the maximum intensity of the tumor response is not detected.

The figure 4.47 represents the results obtained using the Ideal Calibration and SVD method considering the Tumor 3, which central coordinates are $(x_t, y_t, z_t) = (-15, -30, -30)mm$

(a) Ideal Calibration   **(b)** SVD
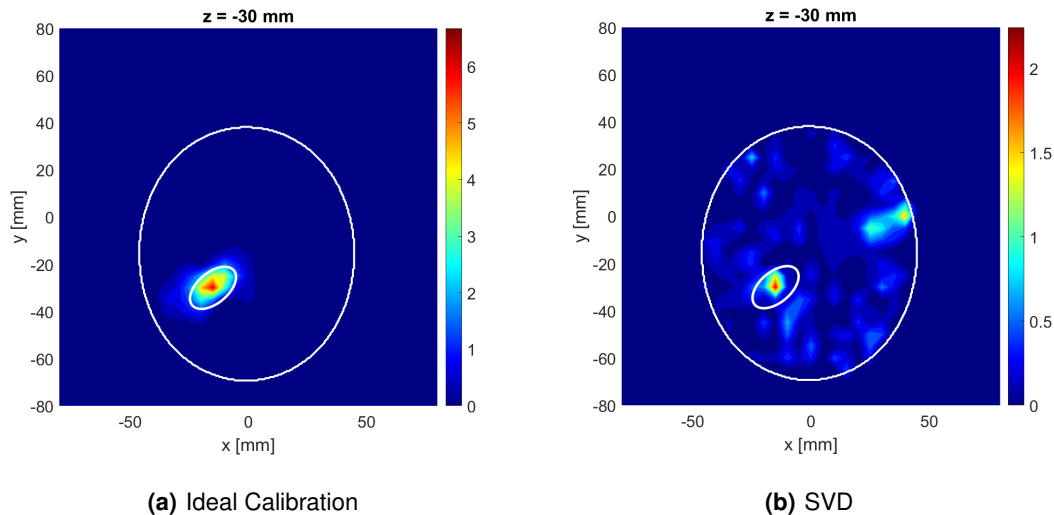
Figure 4.47: Imaging results for the plane z=-30mm considering the Tumor 3, all XETS antennas and using 4.47(a) the ideal calibration 4.47(b) the SVD. The white lines translate the border of the breast with the air and the border between the tumor and the fat.

From the figure obtained, it appears that Tumor 3 can be equally detected with both methods, despite the presence of clutters in the case of SVD, which can be related with high values of q singular values at SVD that will lead to the decrease of the power of the signal and consequently the tumor answer.

4.2 IT's Breast Scanning Setup

As seen in the state of the art, there are several factors that characterize a set-up, namely, the positioning of the patient during an examination, the scan duration, the choice of the signal acquisition domain, the imaging technique, the number and type of antennas, the coupling, the frequency of work, et cetera.

A dedicated setup was built at Instituto de Telecomunicações, at Instituto Superior Técnico, in Lisbon and can be seen in the figure 4.48. The setup can be divided into two parts: the hardware and the communication and will be covered in detail in the subsections 4.2.1 and 4.2.2, respectively.

During the development of the thesis, the setup developed by the IT set-up underwent improvements, namely the inclusion in the set-up of two switches to obtain the reflection coefficients to which the antennas are connected, thus allowing an increase in the number of antennas to be measured during each measurement and consequently the possibility of having more S parameters in the scattering matrix. This topic will be discussed in more detail in the next subsection, which is 4.2.1.B.

Furthermore, the graphical user interface, that is Graphical User Interface (GUI), which interacts directly with the user and which operates the entire setup, has progressed and is, now, more developed, and it will be seen in subsection 4.2.3 .
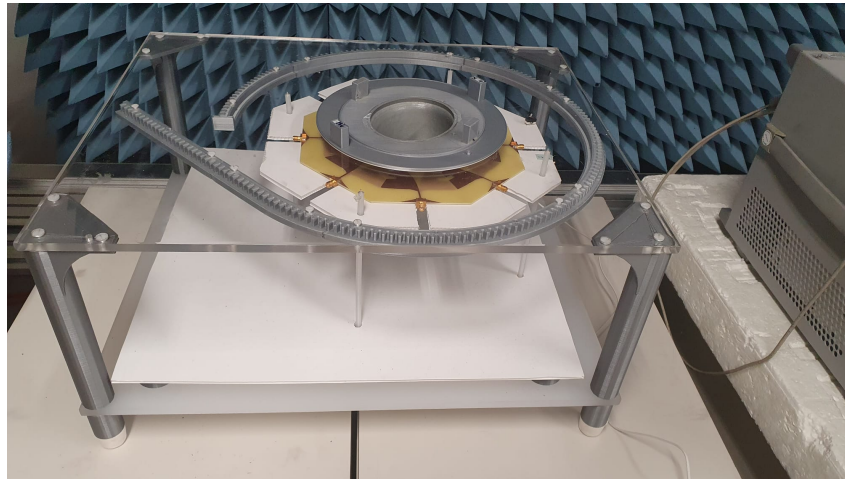
Figure 4.48: General overview of the IT set-up.

In order to summarize all the components involved in the IT imaging setup and the relationships between them, a block diagram was developed, which can be seen in figure 4.49.
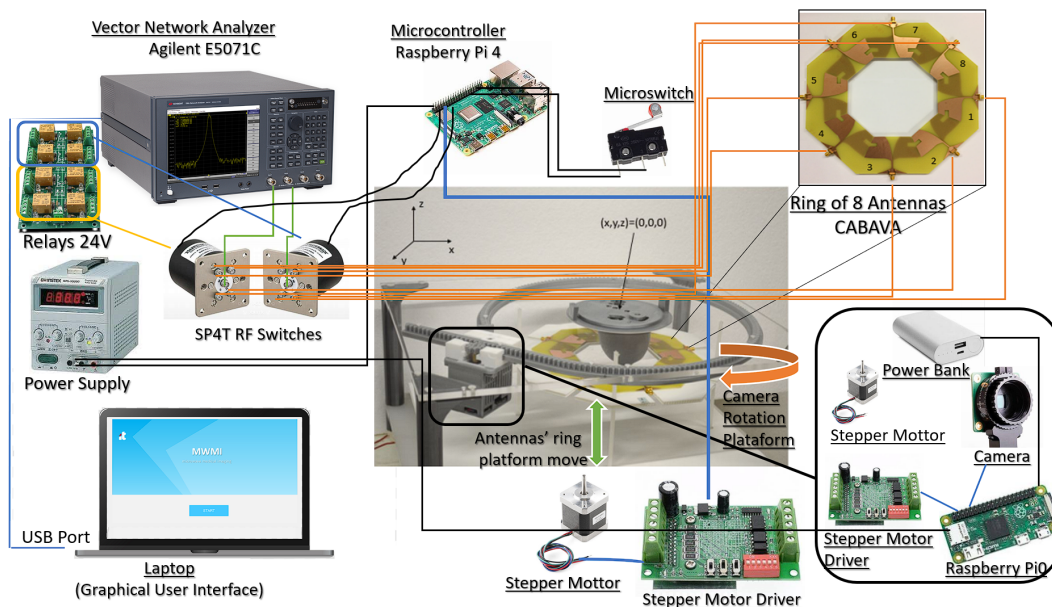
Figure 4.49: Block diagram of the IT imaging system.

The ring of the 8 CABAVA antennas will be connected with the two switches to the VNA, using a switching matrix and the stepper motor will make the antennas' ring platform move upwards and downwards. The entire system will be controlled by a single computer unit and for that it will use a

customized MATLAB program, which is the GUI. Since the program controls all the system, the back-scattered signals will be collected using the GUI interface for future post processing, which is also there.

4.2.1 Hardware

The hardware of the set-up can be divided in three different types of components according to the role that the components have in the set-up, this is, set-up control, radio-frequency measurements and body simulation components. The set-up structure consists of a plexyglass table in order to be transparent, allowing to see the set-up.

This hardware equipment was selected mainly due to their small size and portability, in order to apply the least possible weight in the rail.

The objective of this set-up is to recreate a real examination of a breast. In this set-up, the patient is in the prone position with the breast pendant inside a cavity. Since the set-up does not use any coupling medium, it is referred as a dry setup, which is more practical, hygienic, and fast to operate since it does not require immersion liquid.

4.2.1.A Set-Up Control Components

The set-up control components are responsible for controlling the movements of the antenna's ring and the camera. A Raspberry Pi0 is a wireless controller, which is programmed to control the camera and the motor and it is powered by the power bank. During the examination, the camera takes multiple snapshots of the phantom, from different positions, this is, different angles. The information contained in the pictures is used to build the breast mask.

The reconstruction of the breast shape, this is, profile is crucial for signal processing due to the different refractive indexes of the two media, air and skin, as can be seen in equation 2.6.

There are two motors, where the first is characterized for an unidirectional communication with the Raspberry Pi 0. The technician gives a certain amount of time and the motor makes the cart move, along the rails.

The second motor controls bearing, which make the antennas' ring platform move upwards and downwards. [19] The relative position of the motor is inferred by keeping track of the number of steps taken. This motor needs to know the exact distance that the platform need to go through and this distance is defined by the user. Then, the distance is converted automatically to a movement angle and the motor makes the bearings move during a certain amount time in order to achieve the desired height.

The second motor is connected to Raspberry Pi 4, which activates specific pins alternately in order to control the motor. Moreover, the stepper motor is fed by one voltage generator.

The setup required the incorporation of 2 micro-switches, that is limit switch, which is an electrome-chanical device able to detect the absence or presence of an object. Since, we want an automatic setup,

this limit switch becomes very important, once the main purposes of this device are to create an endpoint an item can travel before it stops and indicates if the object's movement has exceeded its limitations. One was installed top the ring of the antennas in order to stop its movement and the other micro-switch was incorporated to stop and change the direction of the camera movement. The micro-switches are connected to the Raspberry Pi 4, the same that is used by the switches to get the scattering parameters. The limit switch has 3 pins: C (Contact), NO (Normally Open) and NC (Normally close).

The image acquisition routine starts when the camera moves from its initial position to the end of the rail gradually. When the camera reaches the end of the rail, the micro-switch is pressed and the camera changes its movement direction, where the camera goes through a distance, that is equivalent to an 15ºarc and then it takes a snapshot of the phantom. This procedure repeats until the camera reaches its initial position.

4.2.1.B Radio-Frequency Components

In this section, the components have the objective to radiate waves and also to measure the S-parameters. The ring is around the breast, in a circular way, and has 8 CABAVA with the substrate made with FR4. These antennas do not have a perfect isolation due to the short distance that separates each one of them, but it is possible from each antenna to separate the received signal. [18] The distance between each antenna and the phantom is not the same due to the realistic shape of the phantom that was built.

Since, the ring can go upwards and downwards, it is possible to take several scans of the breast, at different heights.

Through the received signals from each position, it is possible to reconstruct the breast interior and pinpoint the tumor.

A 4-port Vector Network Analyzer (VNA) E5071C series is used as signal source and receiver to perform the measurements of the reflection and transmission coefficients. The VNA is calibrated with an ECal module. After the calibration, the antennas are connected to the VNA with coaxial cables.

The Agilent E5071C vector network analyzer has multiple key features, such as:

- Wide frequency coverage: 9 kHz to 20 GHz;

- Low trace noise: < 0.004 dB Root Mean Square (RMS) at 70 kHz Intermediate Frequency Band Width (IFBW), that allows the measurement of signal with a low amplitude level, since the noise is really low.;

- Wide dynamic range: > 123 dB, which defines the amplitude level that is possible to measure;

- 4 ports;

- Fast measurement speed: 9 msec for 401 points with error correction.

As the set-up has 8 antennas and the VNA only has 4 ports, it is not possible to connect all the antennas to the VNA at the same time. Therefore, during this thesis, it was incorporated switches in the set-up and also at GUI. Since each switch has 4 ports, this means that each switch can only have up to 4 antennas connected to each switch. As there are 8 antennas, 2 switches were incorporated.

In addition, a 8 Single Pole Double Throw (SPDT) channel relay board with a power supply of 24 Volt is used, made up of 8 channels, thus allowing to connect to two switches and is used because it is necessary to control the circuit when we select the antennas that we want to measure and get the scattering information. The 2 switches are controlled by a Raspberry Pi 4 and are activated using a voltage generator to feed them. The Figure 4.50(a) represents the connection between the two switches with the relays.

(a)   (b)
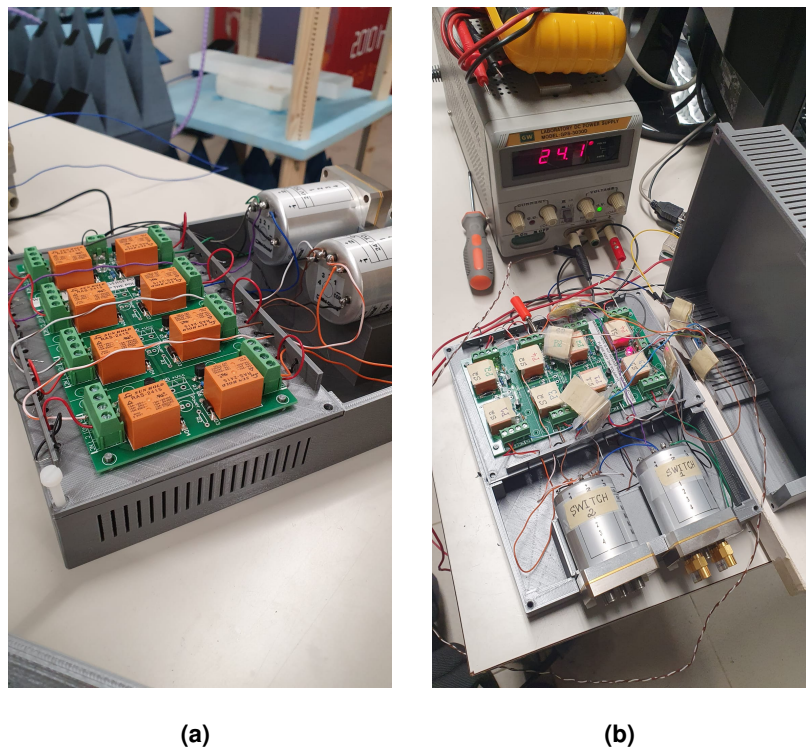
Figure 4.50: Images captured in the lab to show the two switches connected to the relays and these being powered by a 24V voltage generator.8 SPDT channel relay and two coaxial RF Selector Switches

As mentioned the 8-channel relay is wired to the Raspberry Pi 4, this means that it is important to define the GPIO pins of the Raspberry Pi 4 and that are used for each channel and then set these values. By the way, the only factor that must exist in this situation is the possibility of the user having free will to be able to connect the antenna to the switch he wants and to the port of that switch.

The antennas routine starts with the upwards movement of the ring and when it goes through the distance defined by the technician, the VNA measures the antennas' coefficients. This process is repeated

Table 4.2: Table with assignment of the GPIO pins to each switch and the respective port.

GPIO Pins (Rapberry Pi 4)	Switch	Port
20	SW1	P1
16	SW1	P2
21	SW1	P3
12	SW1	P4
26	SW2	P1
6	SW2	P2
19	SW2	P3
13	SW2	P4

until the ring of 8 CABAVA antennas reach the maximum height, also defined by the technician.

Then the antennas ring begins its downward movement, until the micro-switch is pressed, so the movement rings movement stops.

There are 2 switches that allows the measurement process. Since, the user selects previously the antennas to the respective switch. After that, it will appear a S-matrix with all the possible scattered parameters considering the combination between the antennas selected by the user. The first selects an antenna and the second goes through all the 4 antennas that are connected to it. After obtaining the measures, the first switch selects the next antenna and the second goes through all the antennas again. This process ends, when the first switch reaches the last antenna connected and all the S-parameters are saved in in matrices.

4.2.1.C Body Simulation Components

As previously mentioned, the set-up consists of a plexyglass table with a hole in the middle, in which the phantom is placed. The phantom has an anthropomorphic container, which was built based on the structures referred to in section 2.1. This container was made with Polyactic acid (PLA), which is a material that has a lower permittivity when it is compared with the breast skin.

Since, we want to test the microwave imaging technique, a target made also with PLA, which simulates a tumor, is placed inside the container.

IT's Breast Scanning Setup is based on a radar-based MWI and this method approaches the difference between dielectric properties of malignant and surrounding tissues, it is important for this dissertation to address the dielectric properties. The electrical properties of tissues exhibit strong dependence on frequency (frequency dispersion) in the Radio Frequency (RF) and microwave bands and it is dictated by the significant amount of water in living tissue.

Any dielectric material is characterized by its complex permittivity. While the real part is known as the dielectric constant and relates the interaction of the material with the electric field, the imaginary part corresponds to the losses in the material. [18]

It is known that the dielectric constant corresponds to the ratio between the permittivity of a material compared to the permittivity of free space and defines the ability of a material to concentrate the elec-

trical flux. [18] The dielectric constant is essential in order to distinguish the malignant tumor from the surrounding tissue.

In order to simulate the dielectric properties of the tissue structures, both are filled with specific liquids. The fibroglandular tissues were made with the same material as the phantom structures. As discussed in section 1.2.4, phantoms can be classified into 3 different groups, depending on the content of the adipose tissue. As the adipose tissue content increases, the permittivity decreases, which should ease the tumor detection. However, it provokes much more wave attenuation and this is the reason why the detection of the tumor becomes more difficult.

The phantom built to take the measurements belongs to the group, where the adipose tissue content varies between 85% and 100%. In order to simulate the tissues' dielectric properties, the liquid Triton-X 100 is the best option, as mentioned in the section 1.2.4 and there is no need to dilute Triton-X 100 (concentration is 100%), since the phantom belongs to the last group. The liquid, that simulates the properties of the tumor and the fibroglandular tissues, consists on a mixture between Triton-X 100 and salted water, where the fibroglandular tissues have a mixture with a Triton-X 100 concentration of 25% and the tumor has a mixture with a Triton-X 100 concentration of 20%. The recipes of all liquids are reported in [59].

In figure 4.51, it is possible to observe the model to represent the breast and the tumor.

(a) Breast container   (b) Tumor
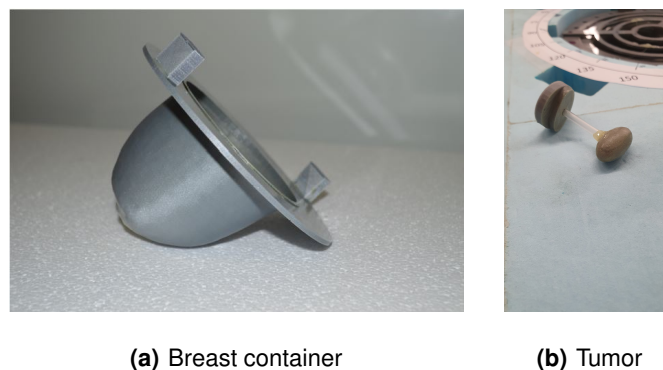
Figure 4.51: Phantom Components.

4.2.2 Communication

The communication of the setup is responsible to control all components and hardware devices via PC, in order to automate the setup. It is done in two distinct ways. The first way corresponds to the VNA being connected to the PC via USB, in such way that the compatibility with the software code can be assured. The other distinct ways consists of the PC generating a Wi-Fi network and each of the Raspberry Pi of the set-up connecting to the PC using their own IP addresses. One of the Raspberry

PI controls the movement of the antennas, the synchronization of the two switches and the activation of the micro-switch, while the other Raspberry Pi controls the movement of the camera.

4.2.3 Graphical User Interface (GUI)

In this chapter, a small introduction of the developed interface will be made and what its role and advantages are, in addition to addressing the menus that exist in this application. Finally, the last section will cover new features and changes made to the GUI.

4.2.3.A Introduction

By meaning, GUI stands for graphical user interface and corresponds to a friendly interface that allows the users in question to interact through icons and other components to devices that may be difficult to access or even more time-consuming.

As discussed above, the Antennas and Propagation group of the Instituto de Telecomunicações (IT) of the Instituto Superior Técnico in Lisbon, has developed a contactless microwave imaging system for breast cancer screening. As with many setups, the more components there are associated with a setup, the greater the need to develop a tool to facilitate and make the process between components faster, especially when the setup will not be used by the developer.

As the setup is to be used by doctors and technicians, the need for a user-friendly interface that is not complex increased. The GUI that corresponds a Graphical User Interface was initialized by this dissertation [18] using the MATLAB tool and then this dissertation was continued, [19].

The main objective of the GUI turns out to be to shorten the measurement procedure, simplify the measurement and even calibration processes, as well as the need for doctors and/or technicians to have to control components and instruments which they may have little knowledge of how control them, for example with a VNA or even a raspberry.

4.2.3.B Main Menus

The Graphical User Interface is divided in three main menus, which are Setup, Calibration and Exam.

While the menus designed for the technician are the Setup and Calibration menus, the menu designed for the doctor is only the Exam menu. An overall tree of the application is shown in figure 4.52.

The Setup menu is composed by multiple sub-menus related withe equipment that will be used during the exam, which includes configuring the VNA, the wiring network and even the Raspberry Pi. The first part regards to the Setup menu as shown in Figure 4.53

The setup menu is divided into three submenus: VNA, Raspberry Pi and Antenna. The VNA submenu is responsible for connection/disconnection, port calibration and configuration parameters, such
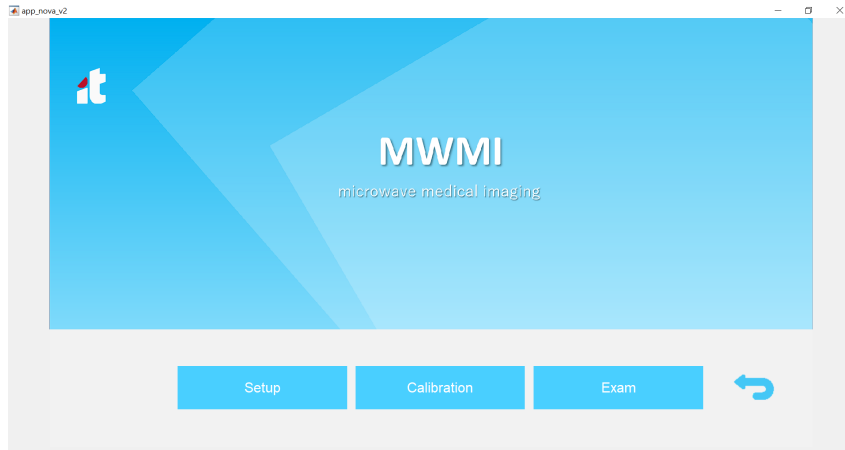
Figure 4.52: Main Menu.
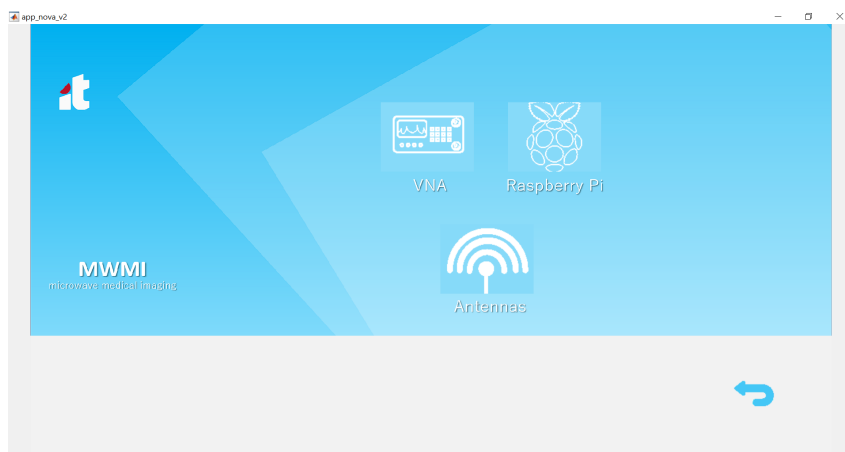
Figure 4.53: Menu of Equipment Setup.

as frequency range. In relation to the Antenna submenu the purpose it is to select an distribute the antennas by the switches and to select the links between antennas that will be active during the measurements, which that the selected scattering parameters will be measured. The Raspberry Pi submenu contains the functions to connect both the raspberry and change their configurations.

Figure 4.54 represents the calibration menu and is directly related with the antennas calibration and it is also used to obtain the free space measurements. The coefficients of free space are important in the application of the SVD method, in order to reduce the internal reflections that occurs inside the antenna structure. The button Antenna Distance will go to the measurement of the scattering parameters in order to calculates the distance that is introduced by the antenna. This distance needs to be considered also in the image reconstruction algorithm.
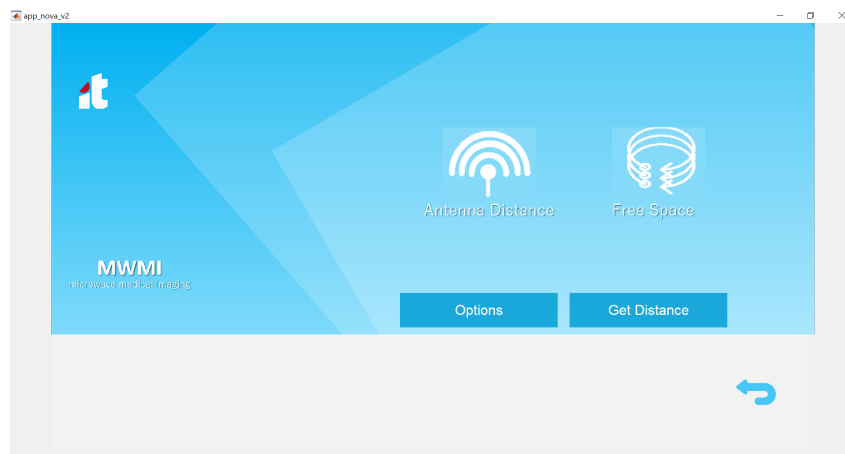
Figure 4.54: Menu of Calibration.

The Exam menu can be seen in figure 4.55 and its main function is associated to the image reconstruction. This menus is divided in three submenus: Target Shape, Scanning and Imaging and it's possible to register a new patient. Target shape menu is related with the camera movement and the camera takes several snapshots of the breast, in order to construct the breast mask. The Scanning submenu controls the movement of the ring of antennas and takes the measurements of the S-parameters. Finally, the Imaging submenu display old photos and calculates the new images using the image reconstruction algorithm.

4.2.3.C   Changes and new features

Some changes were made to the GUI. First, it was introduced buttons in each menu, as there were no buttons before. The previous procedure to change the menu was if the mouse was in a predefined region it was seen as a button, something that was relative if the window of the page was varied. Apart from that with the insertion of buttons and removal of loops used to change menus, the performance of
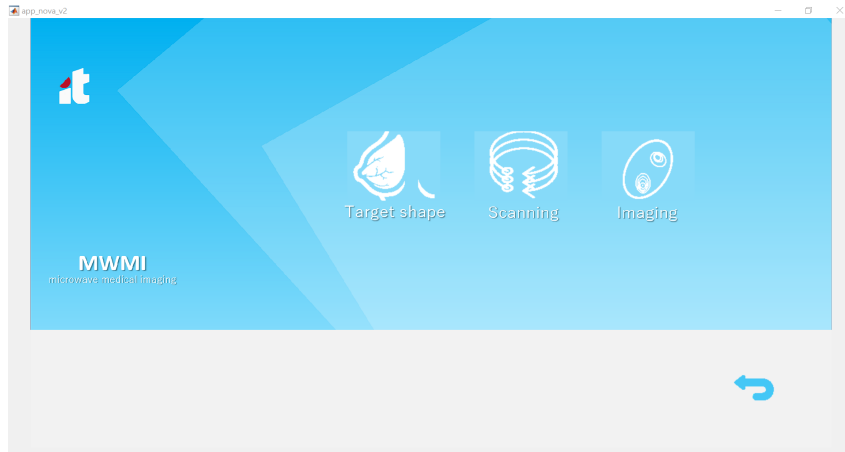
Figure 4.55: Menu of Exam.

the GUI has increased.

Then, I removed as many dialog box as possible, that is, pop ups that appeared, and the resulting dialog messages were integrated directly in the application's background, as can be seen, for example, in Figure 4.56, which depicts a configuration menu of the measurement parameters that will be sent to the VNA.
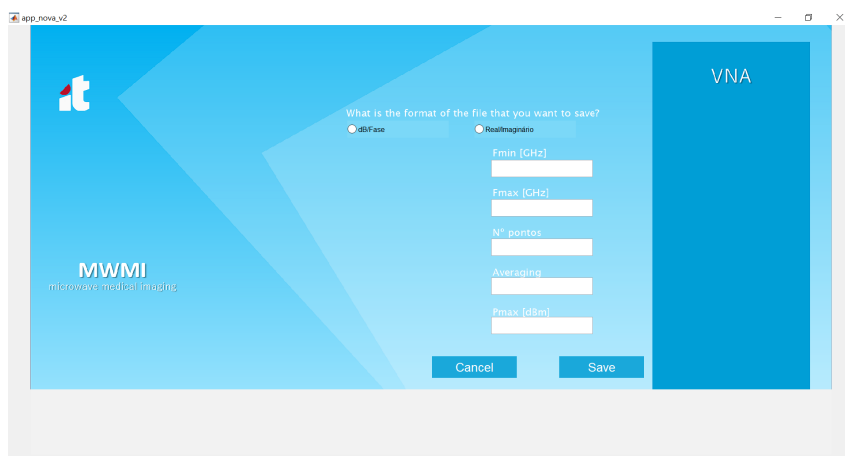
Figure 4.56: VNA configuration menu.

In the menus related to VNA and Raspberry Pi, an icon to represent the status of the equipment was introduced, that is, whether the components are connected or not. If the icon is red, it means that the equipment is not connected and vice versa. In figure 4.57 you can see an example in the VNA menu.

I added to the setup the electronic circuit that connects the GPIO pins of the Raspberry Pi to the switches, as well as defined the GPIO pins used for each port of the switch, which corresponded to the last step to automate the setup, according to [19]. In addition, a button called Wiring was removed, since the selection of antennas was integrated for each switch and even the selection of the links between the

75
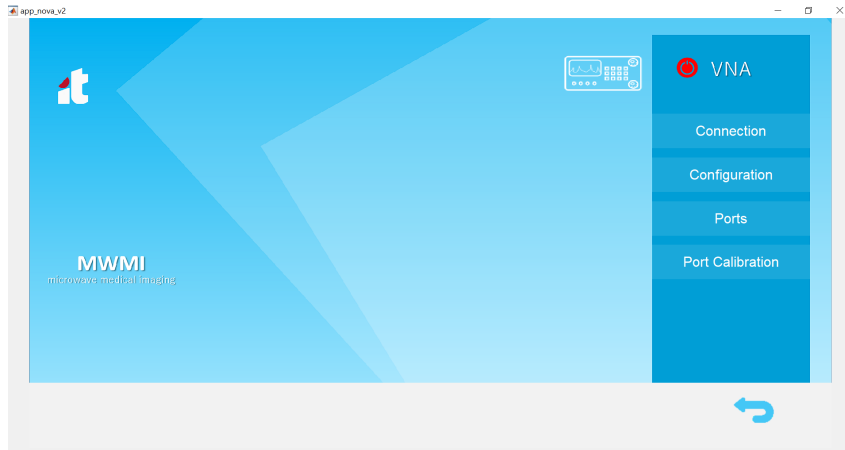
Figure 4.57: VNA menu.

antennas that will be active during measurements in the Antenna menu within the VNA menu.

Figure 4.58: Example with some antennas distributed by the two switches at selection antennas' menu

A menu that allows selecting for each switch the antennas that will be connected was developed. The MATLAB code is prepared to avoid conditions such as placing the same antenna on two switches. The code developed in MATLAB even gives the user the opportunity to not even want to have 4 antennas connected to the 4 ports of the VNA, and can opt for less.

Figure 4.58 represents an example where the user assumed that he only had two antennas connected to each switch, that is, antennas 3 and 1 to switch 1 (SW1) and antennas 2 and 6 to switch 2 (SW2), respectively.

Then it was developed a menu that creates a table with the possible S-parameters according to the selection of antennas depending on the switches. For example, in Figure 4.59, it can be seen that given the selection of antennas 3 and 1 for switch 1 (SW1) and 2 and 6 for switch 2 (SW2), the parameters that are possible to measure are (3,3), (1, 1), (2,2), (6,6), (3,1) , (3,2) , (3.6) (1,2) and (1,6) as shown in

the figure.

It is noteworthy that it is not possible to obtain the S parameters for antennas that are connected to the same switch, excluding the case of the transmitting antenna being the same receiving [(1,1), (2,2) , (3,3) and (6,6)].
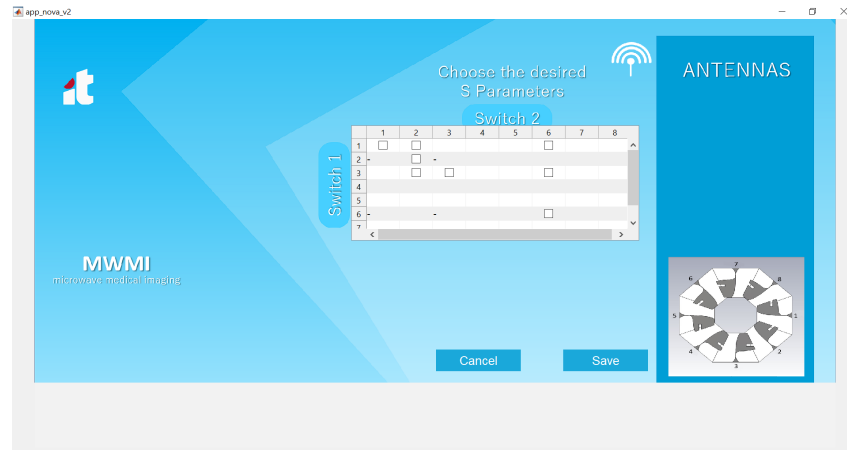
Figure 4.59: Example with the S matrix considering the previous distribution of antennas.4.58

Finally, in order to implement calculation acceleration strategies to allow real-time breast imaging, the need to read some documentation arose. Of which certain techniques were found namely, that one should use functions instead of scripts, as they are generally faster, pre-allocation instead of continuously resizing matrices and even Vectorization, that is, choosing to use matrix and vector instead of writing loop-based code. During this time, the GUI code has been improved, trying to make pre allocations when possible and even avoid using for loops.

5

Conclusions and Future Work

Contents

5.1 Conclusions

Microwave imaging has shown great potential for biomedical applications, such as breast cancer detection.

The first part of this work addressed the knowledge of the different microwave breast imaging systems that already exists and what were the differences between them.

Then, I started the analysis and study of the image reconstruction algorithm, initially using the ideal calibration method, in order to gain some sensitivity on the matter. The third part of this work is the understanding and study of the artifact removal algorithm developed in IT, which is the algorithm that is used at the IT's Breast Scanning Setup.

The antenna is one of the elements in a setup that has so much influence on the performance and in the case if there is a non ideal element in the setup, that element will introduce clutter and distortion the measured signals. One of the adverse effects introduced by the antenna is appears when the antenna is near to the breast skin.

Since for dense breast there are some positions where the antenna is near to the breast skin, the CST was used to analyze and study the behavior of the Crossed Exponentially Tapered Slot (XETS) antenna in relation to the target. XETS antenna is a planar printed and ultrawideband antenna, which provides an extremely stable phase center over the frequency band of operation. XETS has a radiation pattern very stable with frequency, although quasi omnidirectional.

It was possible to know two types of calibration methods: the ideal calibration and Singular Value Decomposition (SVD). The ideal calibration cannot be used in real diagnoses, because it is not possible to obtain results with and without the tumor simultaneously.

During this work it was possible to measure acquired signals with the aid of a Vector Network Analyzer (VNA) for different phantoms anthropomorphic and homogeneous, whose differences are mainly the dimensions, volume and format. Furthermore, different antennas were used, that is XETS, BAVA and CABAVA, in order to compare the performance of antenna topologies.

Some of the images that resulted from the reconstruction algorithm indicated the presence of clutter or the tumor was deviated from its physical position that was measured in the laboratory. In certain breasts, it was not even possible to say that the tumor was detected using SVD and there are so many factors that contribute to that.

Some of the factors that contribute to the tumor is not held are:

- The breast is not symmetric and the SVD algorithm is affected by the non-symmetric distance between the antennas.

- The most critical artifact of all is the reflection that occurs on the breast skin surface, which can be several orders of magnitude higher than the reflection that occurs on the tumor, which can mask

the tumor and the tumor response can be suppressed.

- The distance of the tumor to the breast skin surface.

It is possible to conclude that if the calibration is not performed, the image reconstruction algorithm does not process uniquely the target reflections, since there are two issues skin and fat which compromises the effectiveness of the imaging algorithm used. Furthermore, there is a need to subtract the free-space input reflection coefficient from all the signals in the presence of the breast in order to reduce the internal reflections, which occurs inside the antenna structure.

The other part of this thesis regards microwave breast imaging system developed by the Antennas and Propagation group at Instituto de Telecomunicacões (IT), in Lisbon. During the thesis, two switches were included in the setup, in order to obtain the reflection coefficients to which the antennas are connected, thus allowing an increase in the number of antennas to be measured during each measurement and consequently the possibility of having more S parameters in the scattering matrix.

Furthermore, the Graphical User Interface (GUI) has progressed and is more developed.

5.2 Future Work

Regarding the work experience with the measurement of Signals acquired with Phantoms, a more robust artifact removal algorithm has to be created not only to tackle the additional challenge posed by the non-uniform shape of a breast, but also the stronger skin artifacts, since the value of permittivity contrast between skin and air is high, which compromises the effectiveness of the imaging algorithm.

Even if the switches are now implemented, since the measurements for the free space and metal target are defined only for the height of -150mm, which is the initial position of the antennas' ring, there is a need to have multiple height for the CABAVA antennas. Summarizing, in the free space measurement, a measure is taken before the ring moves and, in the metal target measurement, the ring does not move and a measurement is taken. Furthermore, the "Shape Reconstruction" at the Target shape submenu is not defined yet.

Bibliography

[1] R. Benny, T. Anjut, and P. Mythili, "An overview of microwave imaging for breast tumor detection," *Progess in Electromagnetics Research B*, vol. 87, pp. 61–91, 2020.

[2] J. M. Felício, J. M. Bioucas-Dias, J. R. Costa, and C. A. Fernandes, "Antenna design and near-field characterization for medical microwave imaging applications," *IEEE Transactions on Antennas and Propagation*, vol. 67, no. 7, pp. 4811–4824, 2019.

[3] S. Kwon and S. Lee, "Recent advances in microwave imaging for breast cancer detection," *International journal of biomedical imaging*, vol. 2016, p. 5054912, 2016. [Online]. Available: https://europepmc.org/articles/PMC5210177

[4] C. Curtis, B. R. Lavoie, and E. Fear, "An analysis of the assumptions inherent to near-field beamforming for biomedical applications," *IEEE Transactions on Computational Imaging*, vol. 3, no. 4, pp. 953–965, 2017.

[5] Y. Kuwahara, "Microwave imaging for early breast cancer detection," in *Breast Imaging*, A. M. Malik, Ed. Rijeka: IntechOpen, 2017, ch. 3. [Online]. Available: https://doi.org/10.5772/intechopen.69562

[6] M. R. Casu, M. Vacca, J. A. Tobon, A. Pulimeno, I. Sarwar, R. Solimene, and F. Vipiana, "A cots-based microwave imaging system for breast-cancer detection," *IEEE Transactions on Biomedical Circuits and Systems*, vol. 11, no. 4, pp. 804–814, 2017.

[7] Breast cancer anatomy and how cancer starts. (April,2020). [Online]. Available: https://nbcf.org.au/about-breast-cancer/diagnosis/breast-cancer-anatomy/

[8] Breast anatomy. (April,2020). [Online]. Available: https://www.nationalbreastcancer.org/breast-anatomy

[9] M. J. Burfeindt, T. J. Colgan, R. O. Mays, J. D. Shea, N. Behdad, B. D. Van Veen, and S. C. Hagness, "Mri-derived 3-d-printed breast phantom for microwave breast imaging validation," *IEEE Antennas and Wireless Propagation Letters*, vol. 11, no. 1, pp. 1610–1613, January 2012.

[10] M. S. Islam, N. Kaabouch, and W. C. Hu, "A survey of medical imaging techniques used for breast cancer detection," in *IEEE International Conference on Electro-Information Technology , EIT 2013*, 2013, pp. 1–5.

[11] Cancer stat facts: Female breast cancer. (April,2020). [Online]. Available: https://seer.cancer.gov/statfacts/html/breast.html

[12] B. Moloney, D. O'Loughlin, S. E. Abd, and M. Kerin, "Breast cancer detection—a synopsis of conventional modalities and the potential role of microwave imaging," *MDPI Diagnostics*, vol. 10, no. 2, 2020.

[13] D. O'Loughlin, M. O'Halloran, B. M. Moloney, M. Glavin, E. Jones, and M. A. Elahi, "Microwave breast imaging: Clinical advances and remaining challenges," *IEEE Transactions on Biomedical Engineering*, vol. 65, no. 11, pp. 2580–2590, 2018.

[14] M. Lazebnik, M. Okoniewski, J. H. Booske, and S. C. Hagness, "Highly accurate debye models for normal and malignant breast tissue dielectric properties at microwave frequencies," *IEEE Microwave and Wireless Components Letters*, vol. 17, no. 12, pp. 822–824, 2007.

[15] E. C. Fear, X. Li, S. C. Hagness, and M. A. Stuchly, "Confocal microwave imaging for breast cancer detection: localization of tumors in three dimensions," *IEEE Transactions on Biomedical Engineering*, vol. 49, no. 8, pp. 812–822, 2002.

[16] E. C. Fear and M. A. Stuchly, "Microwave breast cancer detection," in *2000 IEEE MTT-S International Microwave Symposium Digest (Cat. No.00CH37017)*, vol. 2, 2000, pp. 1037–1040 vol.2.

[17] E. Porter, J. Fakhoury, R. Oprisor, M. Coates, and M. Popović, "Improved tissue phantoms for experimental validation of microwave breast cancer detection," in *Proceedings of the Fourth European Conference on Antennas and Propagation*, 2010, pp. 1–5.

[18] C. Rebocho, *Systems for Breast Tumor Detection Using Microwave Imaging*. Instituto Superior Técnico, 2018.

[19] D. Fernandes, *Early Breast Tumor Detection Using a Microwave Imaging System*. Instituto Superior Técnico, 2019.

[20] N. K. Nikolova, "Microwave imaging for breast cancer," *IEEE Microwave Magazine*, vol. 12, no. 7, pp. 78–94, 2011.

[21] D. M.Lazebnik, L.McCartney, "A large-scale study of the ultrawideband microwave dielectric properties of normal breast tissue obtained from reduction surgeries." *Phys Med Biol.*, vol. 52, no. 10, pp. 2637–26 456, 2007.

[22] A. M. Hassan and M. El-Shenawee, "Review of electromagnetic techniques for breast cancer detection," *IEEE Reviews in Biomedical Engineering*, vol. 4, pp. 103–118, 2011.

[23] Mammography. (April,2020). [Online]. Available: https://www.nibib.nih.gov/science-education/science-topics/mammography

[24] P. T. Huynh, A. M. Jarolimek, and S. Daye, "The false-negative mammogram." *RadioGraphics*, vol. 18, no. 5, pp. 1137–1154, 1998, pMID: 9747612. [Online]. Available: https://doi.org/10.1148/radiographics.18.5.974761

[25] S. Radhakrishna, J. S.Agarwal, P. M. Parikh, K.Kaur, S. Panwar, S. Sharma, A. Dey, K. K. Sexena, M. Chandra, and S. Sud, "Role of magnetic resonance imaging in breast cancer management," *South Asian journal of cancer*, vol. 7, no. 2, pp. 69–71, April 2018.

[26] Breast magnetic resonance imaging (mri). (April,2020). [Online]. Available: https://www.hopkinsmedicine.org/health/treatment-tests-and-therapies/breast-mri

[27] Ultrasound breast. (April,2020). [Online]. Available: https://www.radiologyinfo.org/en/info.cfm?pg=breastus

[28] H. Madjar, "Role of breast ultrasound for the detection and differentiation of breast lesions," *S. Karger GmbH*, vol. 5, no. 2, pp. 109–114, April 2010.

[29] Ultrasound. (April,2020). [Online]. Available: https://www.nationalbreastcancer.org/breast-ultrasound

[30] P. M. Meaney, M. W. Fanning, Dun Li, S. P. Poplack, and K. D. Paulsen, "A clinical prototype for active microwave imaging of the breast," *IEEE Transactions on Microwave Theory and Techniques*, vol. 48, no. 11, pp. 1841–1853, 2000.

[31] Y. Kuwahara, S. Miura, Y. Nishina, K. Mukumoto, H. Ogura, and H. Sakahara, "Clinical test of microwave mammography," in *2013 IEEE Antennas and Propagation Society International Symposium (APSURSI)*, 2013, pp. 2028–2029.

[32] The science of looking beneath the surface. (May,2020). [Online]. Available: https://www.kobe-u.ac.jp/research_at_kobe_en/NEWS/spotlight/2019_06_17_01.html

[33] S. Jeon, B. Kim, and S. Son, "Clinical trial of microwave tomography imaging," in *2016 URSI Asia-Pacific Radio Science Conference (URSI AP-RASC)*, 2016, pp. 1–2.

[34] H. Song, S. Sasada, T. Kadoya, M. Okada, K. Arihiro, X. Xiao, and T. Kikkawa, "Detectability of breast tumor by a hand-held impulse-radar detector: Performance evaluation and pilot clinical study," *Scientific Reports*, vol. 7, 12 2017.

[35] L. Duchesne, A. Fasoula, E. Kaverine, G. Robin, and J. Bernard, "Wavelia microwave breast imaging: Identification and mitigation of possible sources of measurement uncertainty," in *2019 13th European Conference on Antennas and Propagation (EuCAP)*, 2019, pp. 1–5.

[36] F. Yang, L. Sun, Z. Hu, H. Wang, D. Pan, R. Wu, X. Zhang, Y. Chen, and Q. Zhang, "A large-scale clinical trial of radar-based microwave breast imaging for asian women: Phase i," in *2017 IEEE International Symposium on Antennas and Propagation USNC/URSI National Radio Science Meeting*, 2017, pp. 781–783.

[37] L. Sani, N. Ghavami, A. Vispa, M. Paoli, G. Raspa, M. Ghavami, F. Sacchetti, E. Vannini, S. Ercolani, A. Saracini, M. Duranti, and G. Tiberi, "Novel microwave apparatus for breast lesions detection: Preliminary clinical results," *Biomedical Signal Processing and Control*, vol. 52, pp. 257 – 263, 2019. [Online]. Available: http://www.sciencedirect.com/science/article/pii/S1746809419301223

[38] M. Solis-Nepote, T. Reimer, and S. Pistorius, "An air-operated bistatic system for breast microwave radar imaging: Pre-clinical validation," in *2019 41st Annual International Conference of the IEEE Engineering in Medicine and Biology Society (EMBC)*, 2019, pp. 1859–1862.

[39] T. Adam Reimer, *Improving Image Reconstruction and Machine Learning Methods in Breast Microwave Sensing*. The University of Manitoba, 2020.

[40] A. Modiri, S. Goudreau, A. Rahimi, and K. Kiasaleh, "Review of breast screening: Towards clinical realization of microwave imaging," *Medical Physics*, vol. 44, 10 2017.

[41] A. Mashal, F. Gao, and S. C. Hagness, "Heterogeneous anthropomorphic phantoms with realistic dielectric properties for microwave breast imaging experiments," *Microwave and Optical Technology Letters*, vol. 53, p. 1896–1902, 2011.

[42] S. D. Meo, L. Pasotti, I. Iliopoulos, M. Pasian, M. Ettorre, M. Zhadobov, and G. Matrone, "Tissue-mimicking materials for breast phantoms up to 50 GHz," *Physics in Medicine & Biology*, vol. 64, no. 5, p. 055006, feb 2019. [Online]. Available: https://doi.org/10.1088/1361-6560/aafeec

[43] D. Flores-Tapia, G. Thomas, and S. Pistorius, "A wavefront reconstruction method for 3-d cylindrical subsurface radar imaging," *IEEE Transactions on Image Processing*, vol. 17, no. 10, pp. 1908–1925, 2008.

[44] N. Joachimowicz, B. Duchêne, C. Conessa, and O. Meyer, "Reference phantoms for microwave imaging," in *2017 11th European Conference on Antennas and Propagation (EUCAP)*, 2017, pp. 2719–2722.

[45] D. R. Herrera, T. Reimer, M. S. Nepote, and S. Pistorius, "Manufacture and testing of anthropomorphic 3d-printed breast phantoms using a microwave radar algorithm optimized for propagation

speed," in *2017 11th European Conference on Antennas and Propagation (EUCAP)*, 2017, pp. 3480–3484.

[46] R. Conceição, H.Medeiros, D.M.Godinho, M.O'Halloran, D.Rodriquez-Herrera, D.Flores-Tapia, and S.Pistorius, "Classification of breast tumor models with a prototype microwave imaging system," *American Association of Physicists in Medicine Medical Physics*, vol. 47, no. 4, pp. 1860–1871, 2020.

[47] D. R. Herrera, T. Reimer, M. S. Nepote, and S. Pistorius, "Manufacture and testing of anthropomorphic 3d-printed breast phantoms using a microwave radar algorithm optimized for propagation speed," in *2017 11th European Conference on Antennas and Propagation (EUCAP)*, 2017, pp. 3480–3484.

[48] How do breasts change during and after pregnancy? (April,2020). [Online]. Available: https://www.medicalnewstoday.com/articles/325602

[49] Breast changes in older women. (April,2020). [Online]. Available: https://www.nhs.uk/live-well/healthy-body/breast-changes-in-older-women/

[50] Anatomy of the breast. (April,2020). [Online]. Available: https://www.mskcc.org/cancer-care/types/breast/anatomy-breast

[51] What is cancer. (April,2020). [Online]. Available: https://www.nationalbreastcancer.org/what-is-cancer/

[52] J.Felício, C.Fernandes, and J.Costa, "Microwave imaging using the kirchoff migration algorithm," *Instituto de Telecomunicações*, 2015.

[53] D. Byrne, M. Sarafianou, and I. J. Craddock, "Compound radar approach for breast imaging," *IEEE Transactions on Biomedical Engineering*, vol. 64, no. 1, pp. 40–51, 2017.

[54] J. Felício, J. Bioucas-Dias, J. Costa, and C. A. Fernandes, "Microwave breast imaging using a dry setup," *IEEE Transactions on Computational Imaging*, vol. 6, no. 1, pp. 167–180, January 2020.

[55] M. Lazebnik, L. McCartney, D. Popovic, C. B. Watkins, M. J. Lindstrom, J. Harter, S. Sewall, A. Magliocco, J. H. Booske, M. Okoniewski, and S. C. Hagness, "A large-scale study of the ultrawideband microwave dielectric properties of normal breast tissue obtained from reduction surgeries," *Physics in Medicine and Biology*, vol. 52, no. 10, pp. 2637–2656, Apr 2007. [Online]. Available: https://doi.org/10.1088/0031-9155/52/10/001

[56] J. M. Felício, C. A. Fernandes, and J. R. Costa, "Uwb body-implantable antenna for short range communication," in *2015 9th European Conference on Antennas and Propagation (EuCAP)*, 2015, pp. 1–3.

[57] Cst - computer simulation technology. (July,2021). [Online]. Available: https://www.cst.com/

[58] R. A. Martins, J. M. Felício, J. R. Costa, and C. A. Fernandes, "Comparison of slot-based and vivaldi antennas for breast tumor detection using machine learning and microwave imaging algorithms," in *2021 15th European Conference on Antennas and Propagation (EuCAP)*, 2021, pp. 1–5.

[59] N. Joachimowicz, C. Conessa, T. Henriksson, and B. Duchêne, "Breast phantoms for microwave imaging," *IEEE Antennas and Wireless Propagation Letters*, vol. 13, pp. 1333–1336, 2014.